Traveling ionospheric disturbances and ionospheric perturbations associated with solar flares in September 2017

Shun-Rong Zhang[1], **Anthea J. Coster**[1], **Philip J. Erickson**[1], **Larisa Goncharenko** [1], **William Rideout**[1], **Juha Vierinen**[2]

[1]MIT Haystack Observatory
[2]University of Tromsø, Tromsø, Norway

Key Points:

- Post-flare TIDs emanating near sunrise terminator propagated predominantly eastward with 150 m/s zonal phase speed and ~30 min period
- Synchronized differential TEC oscillations occurred over the continental US with ~60 min period and decreasing amplitude over time
- Rapid and significant ionospheric up-welling developed in the topside immediately after onset of X-class flare

Plain language description:

A solar flare injects a sudden and strong energy input to the sunlit upper atmosphere at a range of radiation wavelengths important for ionospheric photochemistry and thermospheric dynamics. Impulsive energy inputs from flares are well known to generate sudden ionospheric density enhancements with subsequent quick decay. This study addresses another type of flare-associated ionospheric perturbation, known as traveling ionospheric disturbances (TIDs), in the form of propagating waves in space and time as well as synchronized temporal oscillations over the continental US. Our study provides likely direct observations pointing to a previously unconfirmed TID excitation mechanism associated with solar flare impacts near the sunrise terminator. We observed TIDs with a dense network of GNSS receivers, yielding detection of differential ionospheric electron content with high fidelity and excellent spatio-temporal resolution. We also used incoherent scatter radar observations at Millstone Hill to reveal ionospheric expansion/up-welling associated with flare impact. These results address fundamental questions regarding solar flare influences on initiation of atmospheric and ionospheric waves.

Corresponding author: Shun-Rong Zhang, shunrong@mit.edu

Abstract

Solar flares provide strong impulsive radiation and energy injection to the sunlit upper atmosphere. The impact on the ionosphere is immense in spatial scale, and therefore it is not immediately evident if dramatically elevated neutral heating can lead to excitation of acoustic gravity waves (AGWs). Using primary observations from GNSS differential TEC over the continental US (CONUS), this paper presents post-flare ionospheric observations associated with three X-class flares on 6, 7 and 10 September 2017. Post-flare ionospheric changes had two significant morphological characteristics: (1) a few minutes after the X9.3 flare peak on 6 September, clear TID fronts emanated near the sunrise terminator with alignment parallel to its direction. TIDs propagated predominantly eastward into the dayside with a 150 m/s phase speed and a ~30 min period. (2) Synchronized differential TEC oscillations over CONUS with ~60 min periodicity and damping amplitude over time, following all three X-class flares. Post-flare ionospheric oscillation spectra exhibited significantly enhanced amplitudes and changes of periodicities (including the appearance of the 60-min oscillations). The Millstone Hill incoherent scatter radar observed large ionospheric up-welling occurring nearly simultaneously as detected TIDs at the X9.3 flare peak, with up to 80 m/s enhancements in vertical drift at 500 km lasting for ~ 30 min. Results suggest that significant solar flare heating and associated dynamical effects may be an important factor in TID/AGW excitation.

1 Introduction

Solar flares provide strong impulsive radiation energy injections into the upper atmosphere. They are well-known to generate enhanced electron density in the ionosphere, particularly at lower altitudes depending on the specific EUV spectrum of the flares. Numerous prior studies indicate that solar flares produce a variety of space weather consequences primarily due to sudden enhancements in photo-ionization and photo-absorption in the upper atmosphere; see Mitra [1974] and Mendillo and Evans [1974] for some earlier investigations, Tsurutani et al. [2009] for a recent short review, and Le et al. [2016] and Xiong et al. [2014] for statistical features of solar flare induced ionospheric variations. Other recent work includes studies of solar flare aeronomic impacts with strong dependence on the flare location within the solar disk [Afraimovich , 2000; D. H. Zhang et al., 2002], solar zenith angle dependence [D. H. Zhang and Xiao, 2003; Wan et al., 2005; Hernández-Pajares et al., 2012], influences on the thermosphere [Sutton et al. , 2006; Tsugawa et al., 2007; H. Liu et al., 2007], ionosphere and thermosphere coupling, and equatorial dynamics [H. Liu et al., 2007; Qian et al., 2011; Sumod et al. , 2014; R. L. Zhang et al., 2017].

Prior studies also indicated quasi-periodic bursts of ionospheric density enhancements associated with similar impulsive solar flares, but these ionospheric disturbances are not characterized by propagating features [D. H. Zhang and Xiao, 2003; Hernández-Pajares et al., 2012; Hayes et al., 2017] and thus are not defined as traveling ionospheric disturbances (TIDs). Suggestions have also been made that solar flares could impact characteristics of existing TIDs or TADs (traveling atmospheric disturbances) [Qian et al., 2012a; Helmboldt et al., 2017].

Can solar flare forcing excite TIDs or other significant ionospheric fluctuations? Some of these questions have recently been addressed by simulations using GITM (the Global Ionosphere-Thermosphere Model, Ridley et al. [2006]). Pawlowski and Ridley [2008] studied thermospheric responses to solar flares on 28 October 2003 (X17.2) and 6 November 2004 (M9.3), and indicated that flare-induced intense dayside heating launched nightward propagating gravity waves (GWs) that seem to explain post-flare nighttime enhancements in the neutral density. Another GITM-based thermospheric simulation for a X5.3 flare on 14 July 2000 also yielded “extensive acoustic and gravity wave” excitation in the subsolar region; these GWs with frequencies lower than the buoyancy frequency traveled also into the nightside.

The obvious difficulty with a sudden and large radiation energy input that induces GWs and TIDs arises from the fact that flares influence the entire sunlit ionosphere, and therefore spatial scales of the impact are large enough to lessen expectations that GWs would be excited. However, while a solar flare impacts the whole sunlit atmosphere, the impact remains strongly solar zenith dependent. Therefore, the possibility remains that GWs can be excited at certain solar zenith angles. Qian et al. [2012a] simulations were able to identify strongly localized enhancement of heating in the neutral atmosphere, but suggested instead that flare-associated conditions led to enhancements of pre-existing TIDs that were launched separately by previous geomagnetic storms. Based on a study for the September 2017 solar events, Qian et al. [2019] further pointed out that solar flares alone were not the sufficient conditions to excite *large-scale* traveling atmospheric disturbances (TADs). Thus the flare onset and TID/GW excitation causality remains inconclusive based on existing theoretical work.

Confirmation of a flare - TID/GW causality would add solar flares to the long list of sources of TIDs as manifestations of GWs. Previously studied sources include solar storm and magnetic activity induced high-latitude disturbances [Richmond, 1978; Lyons et al., 2019], lower atmosphere / terrestrial weather induced propagating waves [Azeem et al., 2015], seismologically induced atmospheric waves [Liu et al., 2011], solar terminator waves [Song et al., 2013], solar eclipse induced ionospheric bow waves [Zhang et al., 2017b], and human-induced atmospheric perturbations from e.g. rocket launches [Lin et al., 2017].

In this paper, we provide direct observations of two types of ionospheric fluctuations that occurred immediately after X-class flares, both suggesting unique roles of solar flares. We argue that the type of resulting fluctuations seen in a synchronized fashion over the continental US (CONUS) were unlikely related to pre-existing disturbances, but were more likely associated with a solar flare effect. The other type of fluctuations is TID-like propagation feature emanated near and aligned itself in parallel to the sunrise terminator. Their smaller wavelength and slower propagation (phase) speed seem to suggest that they are not typical LSTIDs. We also provide evidence of ionospheric F region up-welling/expansion following solar flare radiation injection, suggesting that flare-induced measurable heating effects could potentially be linked to GW/TID excitation. Note that our conclusions are necessarily tempered by complex interactions between flare effects and upper atmospheric preconditioning (including the terminator). This work is based on 6-10 September 2017 observations made with GNSS differential TEC over CONUS as well as mid-latitude observations with the Millstone Hill incoherent scatter radar (ISR) located at 42.6°N and 288.5°E.

2 Observation and Analysis Method

Three major solar flare events occurred on 6, 7 and 10 September 2017. Solar-geophysical conditions during 6-10 September exhibited substantial variability (Figure 1). In particular, owing to the CME arrival, elevated solar wind speeds were observed on 8 September, and IMF Bz experienced southward excursion between 7-8 September as well as on 8 September, producing Kp=8 storms and strong AE fluctuations.

The solar active region AR12673 generated a sequence of flares. In this study, we consider three X-class events: the X9.3 flare near S10W30 coordinates at ~12:02 UT on 6 September, the X1.3 flare near S10W43 at 14:36 UT on 7 September, and the X8.2 flare near S09W83 at ~16:02 UT on 10 September. Other flare bursts occurred also during this period but with magnitudes below X class, as evidenced in Figures 2a, 2c and 2e which plot GOES X-ray flux at 0.1-0.8 nm. The analysis reported here concentrates on solar flare timing rather than fine spectrum characteristics as a more important controlling factor on the ionospheric and thermospheric responses. Other details in Figure 2 are related to TEC oscillations to be discussed in Section 3.2.

Geomagnetic activity was quiet on 6 September, with the largest Kp value at 3 for 12:00-15:00 UT and 3+ between 21:00-24:00 UT. AE reached $\gtrsim$500 nT briefly at $\sim$ 10:00 UT and 15:20 UT, 2 hours prior to and 3+ hours after the X9.3 flare peak, respectively. On 7 September, the largest Kp was 8- between 21:00-24:00 UT and 4- between 03:00-12:00 UT; AE peaked at $\sim$ 1000 nT at ~08:00UT, 6+ hours prior to the X8.2 flare. On 10 September, the largest Kp was 3 between 21:00-24:00 UT and 3- between 15:00-18:00 UT; note that on this day the ionosphere was recovering from storm induced negative phase conditions.

Our study focuses primarily on the 6 September events, as geomagnetic activity was low during the time of potentially large flare impacts (within a few hours after major bursts) and therefore significant geomagnetic storm generated large scale TIDs are not anticipated. Nevertheless, as indicated later, for the 6 September event, flare-induced perturbations proved to be quite characteristic (distinctively different from storm-related TIDs) and easily identified.

The 6-10 September was during a season of very strong hurricane activity with a few Category 5 events. Hurricane Irma made landfall at 11:15 UT on 6 September at Sint Maarten, 2500 km away in the southeast of Miami, Florida, the southern tip of CONUS, and moved very slowly toward CONUS (see https://www.nhc.noaa.gov/data /tcr/AL112017_Irma.pdf). Its potential ionospheric impact did not reach the CONUS near the flare peak time unless it traveled at more than 800 m/s, which is unlikely. GNSS observations to be discussed show no sign of inland-ward propagation TIDs at least for the majority portion of CONUS, and no sign of the characteristic concentric wave patterns assocaited with tropospheric activities (e.g., in Azeem et al. [2015]; Nishioka et al. [2013]; Chou et al. [2018]); rather, the TID waves were eastward or southeastward, and the wave fronts were initially quasi-parallel to the solar terminator and then rotated clockwise.

The GNSS data processing algorithms that produce TEC were developed at MIT Haystack Observatory [Rideout and Coster, 2006; Vierinen et al., 2016]. In the CONUS region which was mostly sunlit during these flare events, there were more than 2000 GNSS receivers generating tens of thousands of receiver-satellite paired data segments. For this TID study, ionospheric disturbances were detected at 1-min cadence by analysis of differential TEC values, rather than absolute TEC. A 30° cut-off elevation for ground-satellite ray paths was used to eliminate data close to the horizon. Differential TEC values were derived by subtracting a background TEC variation determined by a low-pass Savitzky-Golay filter [Savitzky and Golay, 1964]. The algorithm used a convolution process with least-squares fitting of successive sub-sets of windows of a given length (e.g., 30 min or 60 min) involving time-adjacent TEC data points from the same GNSS satellite-receiver pair and a linear basis function set. Similar differential TEC analysis methods have been explored extensively since the work of Saito et al. [1998], and the approach used here has been recently used in the analysis of solar eclipse induced ionospheric bow waves by Zhang et al. [2017b] and other eclipse-related perturbation features by Coster et al. [2017].

It should be noted that the filter which is used to determine the smooth background is essentially calculating averages over sliding windows. De-trended data are analyzed only for the time range between $t_1 + w/2$ and $t_2 - w/2$ where t_1 and t_2 are the start and end times of the data segment for a given pair of satellite and receiver, and w is the length of the sliding window in time; the (small) portions affected by de-trending assumptions at the edges of the data are not used. Also immediately before the flare peak, the running average calculated within a 30-min (or 60-min) window that contains the flare peak overestimates the background and thus the differential TEC is artificially negative for the 15 (or 30) minute period before the flare peak. This introduces a large (negative) differential TEC amplitude as an artifact of the background calculation algorithm. However, and most importantly for this fluctuation-based study, the analysis procedure does not introduce artificial fluctuations, nor cancel fluctuations in the data, because the background determined from the low-pass filter remains relatively smooth. The improperly determined trend to be removed only makes the perturbation visualization challenging; with proper post-processing scaling

for visualization (such as in Figures 7-8), the perturbation should be still visible. These filtering features are demonstrated in Figures 3, 4, 7 and 8 discussed in Section 3. Nevertheless, the range between the largest negative ΔTEC and the following ΔTEC enhancement peak provides a very accurate estimate of TEC response to the solar flare.

The ionospheric perturbations are never single frequency simple waves; in particular, there are categories of large scale and medium scale TIDs [Hunsucker, 1982] that may well coexist during a single event. Using different lengths (30-min or 60-min) of sliding windows for de-trending, it is possible to visualize perturbations of different spatial and temporal scales. The trend determined from a 30-min/60-min sliding window contains perturbation periods longer than 30 min/60 min, and therefore after de-trending, residual perturbations in differential TEC contain periods shorter than 30-min/60-min with reduced amplitudes for longer (>30-min/60-min) periods. While the 60-min de-trended data covers the periods in the 30-min de-trended data, amplitudes in the former data are normally significantly larger than the latter. In this study, we focus on results from 30-min sliding windows thus the structures are unlikely the typical LSTIDs. Results from a 60-min window with larger amplitudes are also shown to provide a broader perspective in term of the degree of perturbations.

The accuracy of differential TEC values is based on the accuracy of the GNSS phase measurement, which is less than 0.03 TEC units [Coster et al., 2012], as all satellite and receiver bias terms cancel out in a differential sense. Any fluctuations with changes > 0.03 TECu are considered as meaningful geophysical signals. For the perturbations derived with 30-min sliding windows, the nominal variation range is between ± 0.2 TECu, significantly above the 0.03 TECu limit. During geospace storm-times, differential TEC amplitudes from the 60-min sliding window may well be beyond 1 TECu. For further statistical analysis with these positive and negative differential TEC, the median values of them could be small, below 0.03 TECu, but that is an expected collective behavior (considering sign changes of fluctuations) rather than an accuracy concern.

During the flare events, the incoherent scatter radar at Millstone Hill conducted an observational campaign from 5-15 September, 2017. From the extensive ISR measurement set, we focus in this study on F-region and topside ionospheric responses. We therefore concentrate on zenith pointing topside-mode observations with a 960 μs uncoded pulse (144 km range resolution) and 8 min integration time. The analysis procedure generated reliable topside ionospheric vertical drift data along with other ionospheric parameters.

3 Results

Differential TEC (ΔTEC) analysis on the flare periods previously described provided information on post-flare ionospheric disturbances, in particular the site-specific individual behavior showing both detailed post-flare fluctuation onset and interaction between flare configuration and preconditioning of the ionosphere and thermosphere. The differential analysis results allow the construction of 2-D ionospheric fluctuation maps, as well as overall ionospheric behavior such as CONUS scale ionospheric oscillations.

3.1 Classification of post-flare TEC perturbations

ΔTEC from individual GNSS receiver-satellite pairs produced an accurate measure of ionospheric temporal-spatial variations. After manual examination of hundreds of individual pairs of data for the 6 September solar flare event, we found evidence for ionospheric perturbations following solar flares, in addition to the well-known rapid onset of TEC enhancements. Differential TEC variations both before and after the 6 September X9.3 flare fell roughly into four categories (a-d), depending on ionospheric preconditioning. These are shown in Figure 3, based on a 30-min sliding window to de-trend ionospheric variations. Again, the pre-flare-peak dip in ΔTEC is due to the use of sliding windows

across the flare peak for the background calculation, resulting in elevated background TEC estimation before the flare peak (cf. red curves). We describe a number of distinct response categories, marked by conditions either before or after flare onset:

(a) *Extremely quiet pre-flare ionospheric conditions* (Figure 3a): In this scenario, a 1.6 TECu enhancement was first observed, followed immediately by an obvious TEC oscillation with 0.2 TECu amplitude and 20-30 min periodicity. The results clearly indicate that the X9.3 solar flare directly produced periodic oscillations. As demonstrated later, these were not simply local stationary waves but TIDs with propagating features. The timing of the TID onset was within 15 min after flare maximum.

(b) *Small pre-flare ionospheric perturbations* (Figure 3b): Clear post-flare ionospheric oscillations beyond observed pre-flare amplitudes occurred for this category with 20-30 min periodicities. The periodicity, amplitude, and onset timing of fluctuations were very similar to Category (a). Post-flare and pre-flare oscillations were different in amplitude but were similar in periodicities, all with parameters in the typical AGW regime.

(c) *Post-flare multiple oscillations* (Figure 3c): This response category produced both fast and slow mode oscillations, resulting in modulated multiple-frequency oscillations. In particular, predominant slow oscillations with 30 minute periods and present in Categories (a) and (b) were coupled in this category with smaller amplitude 15-min period fast oscillations. Pre-flare fluctuations had fast oscillations, and these were not completely filtered out by flare effects (whether preconditioning or other type).

(d) *Post-flare damped oscillations* (Figure 3d): For this category, small pre-flare fluctuations were effectively suppressed by the flare impact. Presumably this was due to the fact that the solar flare failed to initiate immediately new TIDs at the periods detectable using a 30-min sliding window. On the other hand, the flare-generated large electron density enhancements likely produced enhanced ion-drag forcing on the pre-flare AGWs with small amplitudes, and therefore, with pre-flare AGWs being filtered out, no visible post-flare fast fluctuations occurred. A slower gradual ionospheric variation for this category with time scales greater than 1 hour did occur as shown in the original TEC in Figures 3d (blue curve).

The four response categories described above were obtained from data in the US east coast areas. In these longitude sectors, flare local time was ~07:00 LT, a time when the ionosphere was subject to usual rapid electron density buildup approximately 2 hrs post-sunrise. The variety of responses across the four categories within data that were in close geographic proximity implies that the complexity of observed flare-induced ionospheric oscillations may be associated with small spatial differences in ionosphere and thermosphere preconditioning. Nevertheless, common features among the (a)-(c) categories do exist: (1) post-flare ionospheric oscillations occurred immediately after the flare, within 15 min after the flare peak, and therefore were apparently associated with the flare; (2) post-flare oscillation periods were primarily between 25-30 min (although longer periodicity, e.g., 45 min did occur as well; cf. Figure 2a); (3) additional aspects of post-flare oscillations were presumably associated with ionospheric and thermospheric preconditioning variations. Category (d) represents a very different but less common scenario, and future quantitative physical analysis is needed to further determine the relative importance of multiple factors. These might include solar flare spectrum specification, AGW excitation processes, ion drag effects due to enhanced plasma density, ionospheric and thermospheric heating effect on neutral and plasma dynamics, and ionosphere and thermosphere preconditioning.

A more general pattern of post-flare TEC fluctuations and evolution over time was obtained by examining all ΔTEC data within small latitude and longitude ranges. These ΔTEC, as shown in Figure 4, were based on 60-min sliding window filtering (different from the 30-min window filtering used in Figure 3). ΔTEC values exhibited clear fluctuations at longitudes impacted by the X9.3 flare (-85°E and -92°E longitudes). Note that similar

fluctuations did not exist immediately before the flare. The -110°E longitude sector was in darkness and not directly impacted by the flare; the fluctuations became visible only after sunrise time ~12:55 UT, a likely indication of solar terminator waves. Apparent fluctuations at -85°E **did not start until the post flare peak time, rather than immediately after sunrise time** at ~11:15 UT, suggesting the significance of flare effects on inducing ionospheric fluctuations, relative to the potential terminator effect which will be further discussed in Section 4.4.

3.2 Perturbation spectrum analysis

To quantify the perturbation properties, an extensive Fast Fourier Transformation (FFT) analysis is conducted based on differential TEC data (derived from the 30-min sliding windows) for individual pairs of GNSS satellite and receiver such as shown in Figure 3. Observations on the flare day (9 September 2017) are used during a 3-hour period between 12:30-15:30 UT when potentially flare induced ionospheric variations took place. For comparisons, two reference days with relatively quiet solar flux and magnetic activity conditions, 9 and 15 September 2017, are also analyzed similarly. Since the data are typically sampled at the rate of 15-20 seconds, the FFT procedure is applied to ~ 500 samples, yielding a selected set of nearly 3000 spectra, from among ~ 150,000 spectra globally, in the longitude sectors between -90 ~ -65 °E over the flare impact area in the CONUS. Spectrum amplitudes for given periods are averaged over the ~3000 spectra, and are shown in Figure 5(a). The quiet-day references from the two days are very similar, however, during the 6 September flare day, enhanced amplitudes for all frequencies are very evident, suggesting clearly the flare impact that existed over the 3 hour post-flare period. The largest amplitude occurs at the 60 min period which is missing for relatively quiet days. Another FFT analysis for data within the 2-hour period 12:30-14:30 UT (therefore avoiding the contamination by the EUV flux burst near 15:00 UT, cf. discussion in the next section) shows a similar 60-min peak. This characteristic oscillation can be also seen in a completely different analysis for the three flare days on 6, 7 and 11 September where the flare onset times are distributed between ~ 12, 14 and 16 UT corresponding to different solar local times over CONUS; see Section 3.3 for discussions on these "synchronized ionospheric fluctuations" with a 60-min periodicity.

Differential TEC oscillations at periodicities in the range of 20-45 min (based on the 30-min sliding window de-trending) are also very evident for both the flare day and the quiet days, as shown in Figure 5a. On the flare day, sub-peaks of the spectrum amplitude are at 35 min and ~25 min periods; on the quiet days, the peak amplitudes are at periods of 45 min, 30 min, and 25 min, perhaps not dramatically different from periods on the 6 September flare day. Using a shorter time span (2 hours) between 12:30-14:30 UT for the spectrum analysis leads to an amplitude peak near 25 min, similar as the one derived using the 3-hour span between 12:30-15:30 UT. Nevertheless, these 25-40 min oscillations are very typical TIDs. Observations do not seem to indicate an unique periodicity below 60-min on the flare day. However, examination of the geological locations of these perturbations with prominent amplitudes leads to interesting findings (Figure 5b). The geologic location for a given spectrum analysis (corresponding to a given pair of GNSS satellite and receiver) is the mean latitude and longitude. For 6 September, locations for the 25-min periodicity with amplitudes over the mean of the ~3000 individual FFT spectrum amplitudes at the corresponding period by 2 standard deviations appear to distribute randomly (or non-regional). noticeably near the solar terminator (~ -90°W) at the flare peak, the southern CONUS, the region of 38-44°N -87~-77°E, and elsewhere. On the quiet days, those locations with prominent amplitudes (above the mean by 2 standard deviations) seem very regional, either near the solar terminator or/and the southern CONUS, but not within the 38-44 40°N -87~-77°E region, and therefore it may be reasonable to assume the flare impact as a common driver of the large amplitude oscillations over a large area of the CONUS that did not exist on the quiet days.

For comparisons of the post-flare oscillations with the pre-flare ones, we analyzed FFT spectra over the same longitude sectors but for the 2 hour period between 07:00-09:00 UT on 6 September. The pre-flare hours 09:00-12:00 UT were deliberately not selected because of the potential contamination on TEC caused by the X2.2 flare at 08:57 UT, even though the CONUS, being completely in the darkness, was not directly impacted. These pre-flare spectra are shown in Figure 5 (magenta dotted). Compared these to the post-flare ones during the 2 hour period between 12:30-14:30 UT (red dotted), it can be seen that, firstly, post-flare amplitudes were more than doubled, secondly, clearly there was no 60-min oscillations during the pre-flare period, and thirdly, the period of the peak oscillation amplitude at ~40 min during the 2 hours between 07:00-09:00 UT appeared to be vanished during the first 2 hours of the post-flare time 12:30-14:30 UT and in the 3 hour interval between 12:30-15:30 UT (red line).

In summary, our spectrum analyses and comparisons among oscillations during the post-flare time, during the same time frame but on the quiet-days, and during the pre-flare time (on the flare day) reveal the following obvious flare effects: (1) significant enhancements of oscillation amplitudes; (2) the occurrence of an unique 60-min periodicity; (3) changes of the oscillation period (in the range of 20-45 min) for dominant amplitudes. It should be noted that the time series used for FFT analysis from the same receiver-satellite pair may be also subject to inherent spatial variations to certain degree. Normally, with the movement of a GNSS satellite, the ionospheric pierce point varies its latitude and longitude by a few degrees, or a few hundred km in the horizontal direction. Thus enhanced amplitudes of certain temporal periodicity may be also interpreted partially as enhanced amplitudes of certain spatial periodicity. Nevertheless, the enhancements of wave activities with temporal/spatial structures are a key flare-induced signature. Next we consider further the 60-min oscillations.

3.3 Synchronized ionospheric fluctuations

The above-mentioned 60-min oscillations are an important feature. Additional analyses for this 6 September event as well as other 2 solar flare events indicate that they are timely synchronized ionospheric fluctuations. In Figure 2, the bottom panels plot CONUS median differential TEC (CMDT). Individual differential TEC could be either negative or positive, and thus CMDT tends to be zero if the disturbances are more or less randomly distributed over CONUS. Therefore the CMDT view attempts to capture synchronized ionospheric variations in the US. Multiple flare bursts after 14:30 UT (indicated by green solid lines) caused immediate synchronized CMDT variations during 6 September. Such flare-time bursts have been reported previously [D. H. Zhang and Xiao, 2003; Hayes et al., 2017]. We note that the time rate of solar flux increase is an important controlling factor in producing visible CMDT response. Thus, the slow flux rise maximizing near 12:46 UT on 6 September did not cause large CMDT spikes, as the closest CMDT spike occurred 15-min later at 13:00 UT and is not likely to be associated with the flux onset.

The non-burst related CMDT oscillations (indicated by dashed vertical lines) following the three major flare events were remarkable, and indicate clear large-scale oscillations directly associated with the flares. On 6 September, the post-flare effect produced a 13:00 UT peak and a smaller CMDT enhancement 40-70 min later (black curve in Figure 2b). On 7 September, the 15:00 UT peak was followed by a sequence of peaks separated by 30-60 min with progressively decreasing amplitudes (blue curve in Figure 2d). On 10 September, the flare induced CMDT peak was first seen 30 min after the flare maximum, followed by additional smaller peaks separated by ~30 min (red curve in Figure 2f). Thus post-flare continental-scale oscillations in CMDT existed in all three September 2017 X-class events.

These CONUS oscillations are more significant (in term of amplitudes) during the flares at 16 UT (10 September) and less so at 12 UT (6 September), likely due to the flare

impact areas over CONUS being largest for the 16 UT flare and smallest for the 12 UT flare. At 16 UT, the entire CONUS was on dayside to receive the full flare impact; at 12 UT, the solar terminator was near the central US at ~ -90°E. It should be noted that any potential sunrise related terminator waves (with reasonably small amplitudes) should be well smoothed out by averaging differential TEC values over CONUS, unless they vary in a highly synchronized fashion over the entire CONUS (which appears unlikely). Thus it is very unlikely that these synchronized oscillations which damped in time for the 3 different events were caused by terminator waves.

3.4 TID characteristics

So far we have referred to post-flare ionospheric variations as fluctuations or oscillations, which are **not necessarily propagating waves or TIDs**. In the following, we consider 2-D ionospheric fluctuations with associated propagation, and we designate this class of response as TIDs.

Sequential maps of ΔTEC on 6 September show 2-D ionospheric fluctuations and evolution in differential TEC, with strong indication of post-X-class-flare TID excitation and propagation. Differential TEC maps spanning the 4 stages of the flare impact are given in Figure 6, (a) pre-flare at 11:40 UT, (b) the onset of TIDs at 12:09 UT a few minutes after the flare, (c) post-flare TIDs 1 hour after the flare peak, and (d) TIDs nearly 4 hours after the flare peak. High cadence maps of TIDs are shown in Figure 7 to demonstrated the initial TID structures. Note that the color scales vary among the maps. At 11:40 UT (Figure 7a), some pre-flare perturbations were present near the US east coast (within the magenta box), with location timing that was approximately more than 10° longitude (40+ min in time) lagged behind the terminator. These fluctuations were aligned in the NE (northeast) to SW (southwest) direction and might have been associated with solar terminator waves which have often been observed in surface pressure in the eastern US [Hedlin et al., 2018].

A few minutes after the flare peak (12:02 UT), clear wave fronts occurred and were aligned primarily in the meridional direction (Figures 6b and 7a-d, within the black boxes). At 12:09 UT the first clearly visible wave fronts occurred in a region near -90°E longitude (black boxes), not very far from the sunrise terminator. Between 12:09 – 12:13 UT, at least 3 wave fronts can be identified.

We examined in more detail the waves at 12:11 UT (Figure 8). The wave fronts in Figure 8b were derived using a 60-min sliding window and corresponded well to the waves in Figure 8a (or Figure 7b) whose analysis is based on a 30-min sliding window, indicating the high intensity of the disturbance. Within the black box near the sunrise terminator in Figure 8a, a group of quasi-parallel wave fronts is evident; they are also quasi-parallel to the sunrise terminator. The wave front azimuth is ~ 110° with respect to geomagnetic north, tilted slightly but still approximately parallel to the -90°E longitude meridian over CONUS. They appear to be locally generated rather than structures moving horizontally into the area, since, as indicated in discussions in following sections, the **horizontal** phase speeds of the structures were indeed eastward but were not moving fast enough to allow wave trains to arrive in the area in merely 10 min by **horizontal** propagation. These wave fronts were separated by ~ 3° in longitude. The magenta box further east (the northeast US) contains an additional group of quasi-parallel wave fronts tilted toward NW-SE. These waves are likely associated with existing solar terminator waves under solar flare influence, because in this region disturbances already existed 30-min before the flare was launched (Figure 6a).

The TID wave fronts evolved in time and were persistently in the NE-SW azimuth for a few hours; they coexisted along with other TIDs, for instance, equatorward propagating TIDs with wave fronts more in the zonal direction (as indicated in Figure 6c for 13:02 UT by the two arrows on the right side of the yellow box); the US west coast TIDs (15:54

UT, Figure 6d) appear to be associated with terminator waves. These other TIDs were unlikely associated with the flare because of an incompatible propagation direction as further explained below.

Detailed propagation features of the post-flare disturbances can be found in the ΔTEC keograms (Figures 9 and 10). The keograms in Figure 9 show ΔTEC variation as a function of UT and longitude for ~40°N latitudes impacted by the 6 September flare. The diagonal cyan area indicates the daily TEC minimum before sunrise. Post-flare disturbances were significantly enhanced, with subsequent propagation in the eastward direction. These propagating TIDs existed for at least 5 hours between ~12:15 - 1700 UT, with amplitudes normally within 0.2 TECu. The speed of this propagation was approximately 10° longitudes in 1.5 hrs (i.e., ~ 150 m/s). Very similar ΔTEC keograms, including eastward propagation and ~150 m/s phase speed, also resulted from 60-min sliding window results (Figure 10). Consistent eastward propagation existed at all latitudes from 30-45°N, with approximately hourly oscillations.

In order to visualize the TID propagation phase delays between longitudes, a cross-correlation analysis of a keogram at ~45°N within -100 – -70 °E and 12:30 – 14:30 UT was conducted, and the results are shown in Figure 11a. The well-organized phase relationship among waves at different longitudes is very evident, and this information was used to estimate the zonal wavelength (3° longitudes, 240 km at ~45°N), zonal phase speed (150 m/s), and periodicity in zonal propagation (~ 30 min). The periodicity of the brightness (correlation) in vertical direction (see vertical small arrows in Figure 11a) indicating synchronized oscillations is estimated as ~40-50 min.

The meridional propagation of TIDs was analyzed similarly using keogram and cross-correlation methods. Figure 11b shows the cross-correlation results for -80°E within 30-45°N. The TIDs exhibited at predominantly equatorward progression within the latitude range. The phase speed of this propagation is estimated at approximately 15° latitudes in 2 hrs (~230 m/s). It is worth noting that this equatorward propagation was initially less evident, but approximately 1-hr after the flare peak, propagation became more significant. This means that post-flare TIDs propagation were initially eastward (with a 150 m/s zonal phase speed), then propagation rotated toward more southeastward. Figure 10b shows also the synchronized oscillations of differential TEC disturbances (small vertical arrowheads) described earlier.

We can estimate the vertical wavelength λ_z based on horizontal wave information derived above and the acoustic gravity wave dispersion relation [Hines, 1960; Yeh and Liu, 1974]:

$$k_h^2(1-\omega_b^2/\omega^2)+k_z^2=k_0^2(1-\omega_a^2/\omega^2) \quad (1)$$

where k_h and k_z are horizontal and vertical wave numbers, $k_0 = \omega/c_0$, ω is the angular frequency, $\omega_b = \sqrt{(\gamma-1)}g/c_0$ is the Brunt-Väisälä frequency, $\omega_a = c_0/2H$ is the acoustic cutoff frequency, $c_0 = \sqrt{\gamma Hg}$ is the speed of sound, γ is the ratio of specific heats, H is the scale height calculated using the MSIS model, and g is the gravitational acceleration. For our case, this expression yields λ_z values of 35-80 km varying with height between 200-400 km in the F-region at 07:00 LT using GW horizontal wavelength λ_h = 250 km, wave period = 30 min, azimuth = 110°. Thus the vertical phase velocity may be estimated as 20-45 m/s. This derived speed appears low and, if estimated correctly, may indicate that the source of these (F region) TIDs was *in situ* (probably in the F1 region) or this TID/AGW relationship is inconsistent with the simplified classical theory. In reality, thermospheric winds in the morning, which are ignored in various dispersion relation equations [Hines, 1960; Vadas , 2007], are typically eastward and poleward with large amplitudes, thus the arriving TIDs in the F region with upward and eastward propagation and corresponding estimations for the wave properties are subject to their strong influences [Yeh et al., 1972; Ding et al., 2003].

The dependence of ionospheric disturbances on both the solar flare and the sunrise terminator can be seen in Figures 9-10 as well. In general, ionospheric disturbances increased right after the flare onset. However, along non-flare impact longitudes at -105°E and westward, disturbances had smaller magnitudes with less clearly organized zonal propagation at 40° and 45°N latitudes (as compared to the flare impact longitudes). Toward lower latitudes (the sub-solar point), post-sunrise TIDs had larger amplitudes and were more difficult to classify as having eastward propagation.

4 Further discussion

We now discuss several important processes that should be considered in order to argue for a flare impact on TID excitation.

4.1 Flare-induced ionospheric heating and up-welling

If the flare impact excited AGWs/TIDs, substantial and immediate heating to the neutral atmosphere would result. Flare related neutral heating arises through multiple pathways: directly from UV absorption which is deposited the most near the thermo-base, and indirectly from elastic and inelastic energy exchange with excessive energetic photoelectrons and ambient electrons with elevated temperature in the F-region ionosphere [Schunk and Nagy, 1978]. These latter energy exchanges, leading to neutral temperature and density increases and up-welling, take place in the F peak region including the topside where neutral density is low.

During the 6 September 2017 flare, clear indication of ionospheric up-welling and expansion occurred in vertical drift enhancement as measured by the Millstone Hill ISR (Figure 11) compared with a non-flare day for similar season and solar cycle conditions. Ion drift increased by 20 m/s at 275 km and by up to 80 m/s at 500 km immediately after the X9.3 flare, vanishing in approximately 30 min. These large upward vertical drifts were accompanied by electron temperature enhancements increasing with altitude up to 300+ K in the topside [Mendillo et al., 2018]. This electron temperature increase provides evidence for ionospheric heating directly driven by the flare.

Post-flare large upward drifts are very typical in the topside. This phenomenon was first reported for the 7 August 1970 solar flare by Mendillo and Evans [1974]. Figure 12 shows another recent example measured with the Millstone Hill ISR during an intense X17.0 solar flare on 7 September 2005. Electron density variations during this flare were discussed in Xiong et al. [2014]. Above 200 km, vertical ion drifts at the flare peak were consistently higher than the pre-flare ones, up to 20 m/s. Meanwhile, while electron density enhancements were large at the F2 peak, electron temperature was clearly enhanced as well, up to 400 K in the topside. The decay of electron temperature and vertical velocity enhancements was relatively long, for about 2 hrs, arising partially from the slower flare flux decay, which is very different from that in the 6 September 2017 case discussed in this study. Electron density decay time was altitude dependent: in the topside, Ne was higher during the flare decay than at the flare peak, possibly due to the flare enhanced plasma scale height and enhanced temperatures which decayed slowly. Thus this comparison between the 2005 and 2017 X-class solar flare, all in September, shows the commonality of enhanced drift velocities in the F region immediately following the flare as well as the difference in the decay time of flare impact on electron density enhancements. These important facts help us understand some of the observed ionospheric disturbances.

Rapid post-flare responses in neutral density were also observed previously [Sutton et al. , 2006; H. Liu et al., 2007]. The intensity of the observed vertical drift enhancement is comparable to geospace storm induced large ionospheric up-welling at subauroral latitudes [Zhang et al., 2017a]. F-region heating effects caused by geomagnetic activity have also been noted previously [Heelis and Coley, 1988; Deng et al., 2011].

4.2 Flare-induced electron density enhancements and post-flare TIDs

Flare-induced heating in the neutrals can impact TID propagation due to changes in the speed of sound as well as in temperature height gradients. Flare-induced significant electron density enhancements can potentially impact the amplitude and perhaps propagation of TIDs as manifestation of GWs. In particular, for a given GW, the ionospheric fluctuation ΔNe is approximately proportional to Ne [Hines, 1960; Hooke, 1968], i.e., ΔNe/Ne is determined primarily by neutral disturbance properties. This implies that Ne enhancements could indicate a larger resulting disturbance amplitude ΔNe. Thus, if there are existing GWs at the flare onset, they are likely more susceptible after the flare. Additionally, flare-induced significant Ne enhancements may impact ion drag forcing on GW propagation and dispersion.

These Ne enhancements are altitude dependent due to the height dependent ionization production rates of electrons. The flare time solar UV/EUV spectrum also modifies this height dependency. As shown in the Millstone Hill ISR electron density profiles for 6 September 2017 [Mendillo et al., 2018], electron density enhancements were well above 50% below 150 km, and up to ~30% near the 250 km F2-peak height, and dramatically smaller above that. Figure 14 provides detailed F1 and F2 peak densities from the radar's highly accurate plasma-line measurements made with one-min time resolution. Typical uncertainty values for these measurements are ~0.1%. These show that NmF2 increased by 1.3×10^{11} el/m^3. NmF2 fluctuations differ between pre- and post- flare times, with post-flare perturbation oscillations being faster (the blue curve). Therefore the majority of the Ne enhancement influences on TIDs occurred at altitudes below 250 km, especially below 150 km. Corresponding changes in TEC were up to 1.8 TECu (see Figures 3, 4, 15) depending, as is well known, on solar zenith angle (longitude). Figure 15 shows this longitude dependence at 3 stages of the flare event: 11:40 UT (pre-flare), 12:02 UT (at the flare peak), and 12:09 UT (7 min after the flare peak). The TEC increases, ΔTEC, were roughly linear with longitude but faster near the terminator. ΔTEC/TEC was dramatically nonlinear across the terminator. Nevertheless, the TEC percentage change, ΔTEC/TEC, was much smaller than the NmF2 percentage change.

Another very significant post-flare process is the decay of enhanced electron density. A prolonged TEC decay was found previously during some flare events (e.g., in Qian et al. [2012a,b]), with TEC enhancements reported as surviving for a few hours. These conditions are conducive to enhanced TID susceptibility. The X9.1 flare in this study, however, showed a very different scenario with a limited electron density enhancement impact on TID parameters. Figure 14 in particular shows that the decay was faster eastward with later local times, a result expected due to shorter plasma life times toward local noon as well as a fairly quick decay in flare EUV irradiation (Figure 2). It took 10 min or less at -90°E and eastward for the enhanced TEC to decay by 50% (Figure 15). At Millstone Hill (-71.5°E), the NmF1 enhancement decayed almost completely in ~20 min (note that NmF1 enhancements after 12:30 UT / 07:44 LT were part of the regular morning density buildup), and the NmF2 enhancement decayed in ~ 15 min. The quick decay in electron density means that a potential impact on the enhanced susceptibility of TIDs due to Ne enhancements (via ΔNe/Ne dependency on GW amplitudes mentioned above) must have been limited to only a short time scope. This important fact argues against any mechanism by which the observed post-flare TIDs mirrored the pre-existing ones that were accentuated by the flare enhanced density. Post-flare TIDs lasted for at least 3 hours and became quite long compared to the lifetime of the flare induced density.

4.3 Geomagnetic activity influences on post-flare TIDs

LSTIDs are often launched by geospace disturbance energy with momentum and material depositions at auroral, cusp, and polar cap latitudes, leading to the excitation of traveling atmospheric disturbances (TADs) [Lu et al., 2015]. Relevant to this study, these facts raise the question of whether weak fluctuations occurring slightly before and after the

flare (Figure 1) could contaminate TID signatures which have been identified in previous sections as directly of solar flare origin.

Typical LSTIDs propagating equatorward from high latitudes have the wave front aligned in the zonal direction, quasi-parallel to magnetic latitudes, as shown in Figure 16 and also in Zakharenkova et al. [2016]; Jonah et al. [2018]; Lyons et al. [2019]. Figure 16 corresponds to AE ~2800 nT. However, for the AE $\gtrsim$500 nT brief disturbance at ~2 hours prior to the flare, the ionospheric disturbance was expected to propagate dominantly equatorward at a slow phase speed and a small amplitude. A faint disturbance wave front may be found in Figure 6c (white dashed line) near 13:00 UT, 3 hours after AE activity onset. It should be emphasized that post-flare zonal TID propagation as well as the meridional wave fronts identified earlier in Section 3.3 (quasi-parallel to the solar terminator) cannot be related to geomagnetic disturbances at ~10:00 UT.

Small magnetic disturbances occurring briefly at ~10:00 UT and ~15:20 UT cannot be considered as the likely driver of synchronized continental scale TEC oscillations mentioned in Section 3.2. The latter large magnetic disturbance at ~ 15:20 UT occurred later than ionospheric oscillation times (peaking at ~ 13:00 and 13:45 UT, Figure 2), and the earlier brief and small disturbances appear to not have led to clear continental-size synchronized oscillations as well as rapid damping of oscillation amplitude. Post-flare oscillations and associated amplitude damping on the other two days are also unlikely related to geomagnetic perturbations.

One possible causative mechanism for a continental-size synchronized oscillation (30-60 min periodicity) is related to as-yet unidentified upper atmospheric intrinsic resonance modes triggered by the solar flare sudden energy input over the entire sunlit atmosphere. The nature of this special mode, and its observational existence, was regarded as one of the seven major challenging ionosphere and thermosphere questions by Rishbeth [2007]. In particular, Rishbeth stated that "Apparent preferences for particular timescales (e.g., 40 minutes and 26 hours) [occur], some times perceived in ionospheric phenomena. Are they real? If so, what is the physics? " This deserves more in-depth investigation in future studies.

4.4 Sunrise terminator waves and post-flare TIDs

The three solar flares discussed here occurred at different UTs which correspond to different local times in the eastern US. While synchronized oscillations were found in all the events, the post-flare propagating TIDs observed on 6 September were primarily near the solar terminator and early in the morning. The moving solar terminator is widely believed to generate waves in different atmosphere layers; Hedlin et al. [2018] recently showed ground-based terminator wave observations over the eastern US. Theories and observational evidence of AGW/TIDs in the thermosphere and ionosphere altitudes exist, as in Somsikov [1991]; Afraimovich [2008]; Forbes et al. [2008]; H. Liu et al. [2009]. It remains unclear whether these ionospheric waves are excited *in situ* or remotely in the lower atmosphere. However, while the terminator sweeps through different longitudes and occurs each day, mid-latitude statistical studies [Song et al., 2013] indicate that AGW/TIDs are not always visible during their passage. This suggests that preconditioning of ionosphere and thermosphere states (e.g., plasma density, thermospheric winds and temperature) could be critically important in setting the characteristics of perturbation response to large changes in energy input, with solar flare effects providing the needed conditions. In addition, the state of the middle atmosphere and MLT could be important for the propagation of AGWs if launched in the stratosphere by the solar terminator.

A similar TEC analysis for 5 September, the day before the X9.3 solar flare, shows evident TIDs which originated in the eastern US (Figure 17). Clear wave fronts were observed, initially being oriented in the NE-SW direction or roughly the meridional direction, and quasi-parallel to the sunrise terminator. At 13:16 UT, there were additional wave

fronts in the zonal direction (e.g., the white dashed line) likely due to equatorward propagating TIDs from high latitudes. All these characteristics, including timing, wave front orientation and evolution, were very similar to the post-flare TIDs on the flare day. Therefore one may ask: were the post-flare TIDs merely terminator waves (TWs), or flare modified terminator waves (FMTWs), or flare-induced waves (FWs) which may interact with existing terminator waves (FWTWs)? Our observations do not support the first scenario of TWs **only**, but support a greater likelihood of FMTW and/or FWs and/or FWTW; key arguments are as follows:

(1) The original TEC data as shown in Figures 3 and 4 demonstrate clearly the timing of post-flare TIDs suggesting a close cause-effect relationship, as TWs alone cannot explain TID timing. Figures 3 and 4 also show pattern changes in fluctuations, more fully described in Section 3.1, that provide support for the occurrence of FMTWs, FW and/or FWTWs. Wave fronts of these FWs or FMTWs are best seen in Figures 6b, 7, and 8 (the black box area).

(2) There are some important differences between TWs in Figure 17 (prior to the flare day) and post-flare waves in Figures 6, 7 and 8. TWs found on 5 September were located essentially in the southeastern US; the post-flare waves were at higher latitudes, more westward, and slightly closer to the terminator. The post-flare TIDs lasted for $\sim$ 5 hours between ~12:15-17:00 UT (Figure 9), with amplitudes up to 0.2 TECu. The pre-flare day TWs have survived for < 1-2 hrs. Other than presumable day to day variability in TWs which is poorly known, FMTW and FW or FWTW signatures are the most reasonable interpretations of our observations. The observed post-flare TIDs propagated clearly eastward (Figure 9), and are opposite to the TW propagation direction in some of the observations reported previously, e.g., the statistical analysis by Song et al. [2013] , and also opposite to the simulations in Pawlowski and Ridley [2008]; Zhu and Ridley [2015].

While multiple types of disturbances, are expected to occur in the same observations over the CONUS, their coexistence in space and time are better evidenced over the eastern US (see the yellow box area in Figure 6), including Millstone Hill. They can be seen in precise ISR plasma-line electron density data (Figure 14) and TEC data. Similarly, the keogram in Figures 9 and 10 and the TID maps e.g. in Figure 6a, 7a and 7b indicate that TWs were present predominantly at -80°E and moved eastward. It is worth noting that TWs, if they do occur, would lag behind the sunrise terminator by one hour or less.

There are a number of unresolved problems regarding the excitation mechanism of GWs/TIDs by solar flares. Our observations provide a comprehensive view of TIDs and synchronized oscillations where high correlation exists between flare onset and TIDs at post-flare and post-sunrise, although the exact physical processes and their causality remain largely speculative. More fundamental questions lie in excitation of terminator waves and their subsequent propagation. Specifically: what determines the presence of fluctuations as TIDs in the ionosphere, and what are most favored excitation/propagation conditions? Furthermore, how does a flare occurring simultaneously with a regular solar terminator effect enhance the likelihood of TID presence and susceptibility? We assert here that quantitative simulation of these mechanisms is clearly needed to be able to reproduce terminator wave characteristics and associated variability, as well as flare and terminator interplay in shaping the important presence of ionospheric and atmospheric waves.

5 Summary

Based on GNSS differential TEC observations as well as Millstone Hill ISR observations during the September 2017 space weather events, this study provides the first observations of post-flare ionospheric oscillations as well as potential flare-induced and/or flare-modified TIDs. Two specific types of post-flare ionospheric perturbations are identified: **a)** synchronized

continental scale oscillation behavior with attenuating amplitudes over time (not necessarily propagating features); **b)** post-flare large scale TIDs with the following characteristics:

b1) Ionospheric disturbance wave fronts occurring at ~ 90°E and eastward, within 10 min after the flare peak, and oriented quasi-parallel to the solar terminator.

b2) Wave fronts had a ~240 km zonal wavelength, and propagated eastward initially into the dayside at a 150 m/s phase speed and a ~ 30 min period.

b3) Their orientation evolved over time from primarily meridional direction toward more NE-SW direction. The clear wave front survived for more than 3 hours, and the consistent zonal propagation existed for at least 5 hours.

These post-flare TIDs are different from the solar terminator wave TIDs launched on the previous day in terms of wave front location and life time. The eastward propagation of post-flare TIDs seems opposite to the TW propagation reported elsewhere. It appears that these post-flare disturbances are more likely TIDs that were excited by the solar flare near the solar terminator and perhaps coexist or even interact with regular solar terminator waves.

FFT spectrum analyses of periodical oscillations in the differential TEC and comparisons among oscillations during the post-flare time, during the same time frame but on the quiet-days, and during the pre-flare time (on the flare day) reveal the following flare effects: (1) significant enhancements of oscillation amplitudes; (2) the occurrence of a unique 60-min periodicity; (3) changes of the oscillation period (in the range of 20-45 min) for dominant amplitudes. Although some of these short-period temporal oscillations may be also interpreted partially as certain spatial periodicity (due to the ionospheric pierce point movement in the time series data for a pair of receiver and satellite), the enhancements of wave activities with temporal/spatial structures are a key flare-induced signature.

GNSS TID onset was accompanied by immediate local heating and up-welling of the ionosphere primarily in the topside, shown as substantial upward ion drift enhancements in Millstone Hill ISR observations. This ionospheric response is likely relevant to, although not the same as, the sudden upper atmospheric heating necessary for *in situ* TID excitation, caused by flare energy injection. However, the flare-enhanced plasma density decayed very quickly and returned to background levels in <30 min.

The overall picture of post-flare ionospheric changes as revealed in this study is characterized by very dynamic ionospheric disturbances near the solar terminator. In addition to better known enhancements in ionospheric ionization and neutral density, ionospheric heating and up-welling in the topside are immediate and significant. We hypothesize that sudden solar flare energy inputs trigger certain (but not yet completely quantified) ionospheric inherent resonances leading to observed 30-60 min synchronized TEC oscillations which are damped quickly in amplitude. Meanwhile, TIDs are presumably excited by the flare near the solar terminator and are therefore related to joint flare and sunrise effects. These TIDs could interact with pre-existing solar terminator induced TIDs. As a result, post-flare TIDs have a characteristically small zonal wavelength (~240 km) and travel eastward at a slow phase speed (~150 m/s).

Acknowledgments

GPS TEC data products and access through the Madrigal distributed data system are provided to the community (http://www.openmadrigal.org) by the Massachusetts Institute of Technology (MIT) under support from US National Science Foundation (NSF) grant AGS-1762141, which also supports ISR observations and analysis at MIT Haystack Observatory. SRZ and PJE acknowledge NASA LWS funding support (NNX15AB83G), SRZ and AJC the DoD Multidisciplinary Research Program of the University Research Initiative (MURI)

project FA9559-16-1-0364, AJC and SRZ the NASA LWS RAISE project (NNX14AH54G), and AJC, SRZ and LPG the ONR grant N00014-17-1-2186. Data for TEC processing is provided from the following organizations: UNAVCO, Scripps Orbit and Permanent Array Center, Institut Geographique National, France, International GNSS Service, The Crustal Dynamics Data Information System (CDDIS), National Geodetic Survey, Instituto Brasileiro de Geografia e Estatística, RAMSAC CORS of Instituto Geográfico Nacional de la República Argentina, Arecibo Observatory, Low-Latitude Ionospheric Sensor Network (LISN), Topcon Positioning Systems, Inc., Canadian High Arctic Ionospheric Network, Centro di Ricerche Sismologiche, Système d'Observation du Niveau des Eaux Littorales (SONEL), RENAG : REseau NAtional GPS permanent, GeoNet - the official source of geological hazard information for New Zealand, GNSS Reference Networks, Finnish Meteorological Institute, and SWEPOS - Sweden.

GPS data analyzed can be found here:
https://w3id.org/cedar?experiment_list=experiments2/2017/gps/06sep17&file_list=los_20170906.001.h5
https://w3id.org/cedar?experiment_list=experiments2/2017/gps/07sep17&file_list=los_20170906.001.h5
https://w3id.org/cedar?experiment_list=experiments2/2017/gps/08sep17&file_list=los_20170908.001.h5
https://w3id.org/cedar?experiment_list=experiments2/2017/gps/09sep17&file_list=los_20170909.001.h5
https://w3id.org/cedar?experiment_list=experiments2/2017/gps/10sep17&file_list=los_20170910.001.h5

The majority of ISR data analyzed in the paper can be found here:
https://w3id.org/cedar?experiment_list=experiments/2017/mlh/05sep17&file_list=mlh170905g.001.hdf5

Solar X-ray flux data from GOES-15 were obtained from NOAA NGDC at
http:// satdat.ngdc.noaa.gov/sem/goes/data/

Solar wind and magnetic AE and Kp index data at
https://omniweb.gsfc.nasa.gov/ow_min.html

References

Afraimovich, E. L., A. T. Altynsev, V. V. Grechnev, and L. A. Leonovich (2002), The response of the ionosphere to faint and bright solar flares as deduced from global GPS network data, Ann. Geophys., 45(1), 31-40.

Afraimovich, E. L. (2008). First GPS-TEC evidence for the wave structure excited by the solar terminator. Earth, Planets and Space, 60(8), 895-900. http://doi.org/10.1186/BF03352843

Azeem, I., J. Yue, L. Hoffmann, S. D. Miller, W. C. Straka III, and G. Crowley (2015), Multisensor profiling of a concentric gravity wave event propagating from the troposphere to the ionosphere, Geophys. Res. Lett., 42, 7874-7880, doi:10.1002/2015GL065903.

Chou, M. Y., Lin, C. C. H., Huba, J. D., Lien, C. P., Chen, C. H., Yue, J., et al. (2018). Numerical Modeling of the Concentric Gravity Wave Seeding of Low-Latitude Nighttime Medium-Scale Traveling Ionospheric Disturbances. Geophyical Research Letters, 45(13), 6390-6399. http://doi.org/10.1029/2018GL077959

Coster, A., D. Herne, P. Erickson, and D. Oberoi (2012), Using the Murchison Widefield Array to observe midlatitude space weather, Radio Sci., 47, RS0K07, doi:10.1029/2012RS004993.

Coster, A. J., L. Goncharenko, S.-R. Zhang, P. J. Erickson, W. Rideout, J. Vierinen (2017), GNSS Observations of Ionospheric Variations During the 21 August 2017 Solar Eclipse, Geophys. Res. Lett. 44, doi:10.1002/2017GL075774.

Deng, Y., T. J. Fuller-Rowell, R. A. Akmaev, and A. J. Ridley (2011), Impact of the altitudinal Joule heating distribution on the thermosphere, J. Geophys. Res., 116, A05313, doi:10.1029/2010JA016019.

Ding, F., Wan, W., & Yuan, H. (2003). The influence of background winds and attenuation on the propagation of atmospheric gravity waves. Journal of Atmospheric and Solar-Terrestrial Physics, 65(7), 857–869. http://doi.org/10.1016/S1364-6826(03)00090-7

Forbes, J. M., Bruinsma, S. L., Miyoshi, Y., & Fujiwara, H. (2008). A solar terminator wave in thermosphere neutral densities measured by the CHAMP satellite. Geophyical Research Letters, 35(14), 1513. http://doi.org/10.1029/2008GL034075

Hayes, L. A., Gallagher, P. T., McCauley, J., Dennis, B. R., Ireland, J., and Inglis, A. (2017). Pulsations in the Earth's lower ionosphere synchronized with solar flare emission. Journal of Geophysical Research: Space Physics, 122, 9841-9847. https://doi.org/10.1002/2017JA024647

Hedlin, M. A. H., de Groot-Hedlin, C. D., Forbes, J. M., & Drob, D. P. (2018). Solar Terminator Waves in Surface Pressure Observations. Geophyical Research Letters, 45(10), 5213-5219. http://doi.org/10.1029/2018GL078528

Heelis, R. A., and W. R. Coley (1988), Global and local Joule heating effects seen by DE 2, J. Geophys. Res., 93(A7), 7551-7557, doi:10.1029/JA093iA07p07551.

Helmboldt, J. F., Kassim, N. E., and Teare, S. W. (2015). Observations of the ionospheric impact of M-class solar flares on local and hemispheric scales. Earth and Space Science, 2(10), 387-402. http://doi.org/10.1002/2015EA000116

Hernández-Pajares, M., A. García-Rigo, J. M. Juan, J. Sanz, E. Monte, and A. Aragón-Àngel (2012), GNSS measurement of EUV photons flux rate during strong and mid solar flares, Space Weather, 10, S12001, doi:10.1029/2012SW000826.

Hines, C. O. (1960). Internal atmospheric gravity waves at ionospheric heights. Canadian Journal of Physics, 38(11), 1441-1481. http://doi.org/10.1139/p60-150

Hooke, W. H. (1968). Ionospheric irregularities produced by internal atmospheric gravity waves. Journal of Atmospheric and Terrestrial Physics, 30(5), 795-823. http://doi.org/10.1016/S0021-9169(68)80033-9

Hunsucker, R. D. (1982). Atmospheric gravity waves generated in the high-latitude ionosphere: A review. Reviews of Geophysics, 20(2), 293–315. http://doi.org/10.1029/RG020i002p00293

Jonah, O. F., Coster, A., Zhang, S.-R., Goncharenko, L. M., Erickson, P. J., de Paula, E. R., & Kherani, E. A. (2018). TID Observations and Source Analysis During the 2017 Memorial Day Weekend Geomagnetic Storm Over North America. Journal of Geophysical Research: Space Physics, 42(4), 7874. http://doi.org/10.1029/2018JA025367

Le, H., L. Liu, Y. Chen, and W. Wan (2013), Statistical analysis of ionospheric responses to solar flares in the solar cycle 23, J. Geophys. Res. Space Physics, 118, 576-582, doi:10.1029/2012JA017934.

Lin, C. C. H., M.-H. Shen, M.-Y. Chou, C.-H. Chen, J. Yue, P.-C. Chen, and M. Matsumura (2017), Concentric traveling ionospheric disturbances triggered by the launch of a SpaceX Falcon 9 rocket, Geophys. Res. Lett., 44, 7578-7586, doi:10.1002/2017GL074192.

Liu, H., H. Lühr, S. Watanabe, W. Köhler, and C. Manoj (2007), Contrasting behavior of the thermosphere and ionosphere in response to the 28 October 2003 solar flare, J. Geophys. Res., 112, A07305, doi:10.1029/2007JA012313.

Liu, H., Lühr, H.,& Watanabe, S. (2009). A solar terminator wave in thermospheric wind and density simultaneously observed by CHAMP. Geophyical Research Letters, 36(10), 377. http://doi.org/10.1029/2009GL038165

Liu, J.-Y., C.-H. Chen, C.-H. Lin, H.-F. Tsai, C.-H. Chen, and M. Kamogawa (2011), Ionospheric disturbances triggered by the 11 March 2011 M9.0 Tohoku earthquake, J. Geophys. Res., 116, A06319, doi:10.1029/2011JA016761.

Lu, G., M. E. Hagan, K. Häusler, E. Doornbos, S. Bruinsma, B. J. Anderson, and H. Korth (2015), Global ionospheric and thermospheric response to the 5 April 2010 geomagnetic storm: An integrated data-model investigation, J. Geophys. Res. Space Physics, 119, 10,358-10,375, doi: 10.1002/2014JA020555.

Lyons, L. R., Y. Nishimura, S.-R. Zhang, A. J. Coster, A.Bhatt, E. Kendall4, Y. Deng (2019) Identification of auroral zone activity driving large-scale traveling ionospheric disturbances, J. Geophys. Res. Space Physics, 10.1029/2018JA025980

Mendillo, M. and J. V. Evans (1974), Incoherent scatter observations of the ionosphere with respect to a large solar flare, Radio Sci., 9, 197-210.

Mendillo, M., Erickson, P. J., Zhang, S.-R., Mayyasi, M., Narvaez, C., Thiemann, E., et al. (2018). Flares at Earth and Mars: An Ionospheric Escape Mechanism? Space Weather, 315(5811), 501. http://doi.org/10.1029/2018SW001872

Mitra, A. P. (1974), Ionospheric Effect of Solar Flares, 294 pp., Springer, New York.

Nishioka, M., Tsugawa, T., Kubota, M., & Ishii, M. (2013). Concentric waves and short-period oscillations observed in the ionosphere after the 2013 Moore EF5 tornado. Geophyical Research Letters, 40(21), 5581-5586. http://doi.org/10.1002/2013GL057963

Pawlowski, D. J., and A. J. Ridley (2008), Modeling the thermospheric response to solar flares, J. Geophys. Res., 113, A10309, doi:10.1029/2008JA013182.

Qian, L., Burns, A. G., Chamberlin, P. C., and Solomon, S. C. (2011). Variability of thermosphere and ionosphere responses to solar flares. Journal of Geophysical Research: Space Physics (1978-2012), 116(A10), A10309. http://doi.org/10.1029/2011JA016777

Qian, L., A. G. Burns, H. Liu, and P. C. Chamberlin (2012a), Effect of a solar flare on a traveling atmospheric disturbance, J. Geophys. Res., 117, A10319, doi:10.1029/2012JA017806.

Qian, L., A. G. Burns, S. C. Solomon, and P. C. Chamberlin (2012), Solar flare impacts on ionospheric electrodyamics, Geophys. Res. Lett., 39, L06101, doi:10.1029/2012GL051102.

Qian, L., Wang, W., Burns, A. G., Chamberlin, P. C., Coster, A., Zhang, S.-R., & Solomon, S. C. (2019). Solar Flare and Geomagnetic Storm Effects on the Thermosphere and Ionosphere During 6 – 11 September 2017. Journal of Geophysical Research: Space Physics, 124. https://doi.org/10.1029/2018JA026175

Ridley, A. J., Y. Deng, and G. Toth (2006), The global ionosphere-thermosphere model, J. Atmos. Sol.-Terr. Phys., 68, 839.

Richmond, A. D. (1978), Gravity wave generation, propagation, and dissipation in the thermosphere, J. Geophys. Res., 83, 4131-4145, doi:10.1029/JA083iA09p04131.

Rishbeth, H. (2007), Thermospheric targets, Eos Trans. AGU, 88(17), 189-193, doi:10.1029/2007EO170002.

Rideout, W., and A. Coster (2006), Automated GPS processing for global total electron content data, GPS Solutions, 10, 219-228, doi:10.1007/s10291-006-0029-5.

Savitzky, A., and Golay, M. J. E. (1964). Smoothing and differentiation of data by simplified least squares procedures. Analytical Chemistry, 36, 1627-1639.

Saito, A., Fukao, S., and Miyazaki, S. (1998). High resolution mapping of TEC perturbations with the GSI GPS Network over Japan. Geophysical Research Letters, 25(16), 3079-3082.

Schunk, R. W., and A. F. Nagy (1978), Electron temperatures in the F region of the ionosphere: Theory and observations, Rev. Geophys., 16(3), 355-399, doi:10.1029/RG016i003p00355.

Somsikov, V. M. (1991), Atmospheric waves caused by the solar terminator: a review, Geomagn. Aeron., 31, 1-12.

Song, Q., F. Ding, W. Wan, B. Ning, L. Liu, B. Zhao, Q. Li, and R. Zhang (2013), Statistical study of large-scale traveling ionospheric disturbances generated by the

solar terminator over China, J. Geophys. Res. Space Physics, 118, 4583-4593, doi:10.1002/jgra.50423.

Sumod, S. G., T. K. Pant, C. Vineeth, and M. M. Hossain (2014), On the ionospheric and thermospheric response of solar flare events of 19 January 2005: An investigation using radio and optical techniques, J. Geophys. Res. Space Physics, 119, 5049-5059, doi:10.1002/2013JA019714.

Sutton, E. K., J. M. Forbes, R. S. Nerem, and T. N. Woods (2006), Neutral density response to the solar flares of October and November, 2003, Geophys. Res. Lett., 33, L22101, doi:10.1029/2006GL027737.

Tsugawa, T., S.-R. Zhang, A. J. Coster, Y. Otsuka, J. Sato, A. Saito, Y. Zhang, and L. J. Paxton (2007), Summer-winter hemispheric asymmetry of the sudden increase in ionospheric total electron content and of the O/N2 ratio: Solar activity dependence, J. Geophys. Res., 112, A08301, doi:10.1029/2007JA012415.

Tsurutani, B. T., O. P. Verkhoglyadova, A. J. Mannucci, G. S. Lakhina, G. Li, and G. P. Zank (2009), A brief review of "solar flare effect" on the ionosphere, Radio Sci., 44, RS0A17, doi:10.1029/2008RS004029.

Vadas, S. L. (2007). Horizontal and vertical propagation and dissipation of gravity waves in the thermosphere from lower atmospheric and thermospheric sources. Journal of Geophysical Research: Space Physics (1978–2012), 112(A6), n/a–n/a. http://doi.org/10.1029/2006JA011845

Vierinen, J., A. J. Coster, W. C. Rideout, P. J. Erickson, and J. Norberg (2016), Statistical framework for estimating GNSS bias, Atmos. Meas. Tech., 9, 1303-1312, doi:10.5194/amt-9-1303-2016.

Wan, W., L. Liu, H. Yuan, B. Ning, and S. Zhang (2005), The GPS measured SITEC caused by the very intense solar flare on July 14, 2000, Adv. Space Res., 36, 2465-2469.

Xiong, B., W. Wan, B. Ning, F. Ding, L. Hu, and Y. Yu (2014), A statistic study of ionospheric solar flare activity indicator, Space Weather, 12, 29-40, doi:10.1002/2013SW001000.

Yeh, K. C., Webb, H. D., & Cowling, D. H. (1972). Evidence of Directional Filtering of Travelling Ionospheric Disturbances. Nature Physical Science, 235(59), 131–132. http://doi.org/10.1038/physci235131a0

Yeh, K. C., & Liu, C. H. (1974). Acoustic-gravity waves in the upper atmosphere. Reviews of Geophysics, 12(2), 193-216. http://doi.org/10.1029/RG012i002p00193

Zakharenkova, I., E. Astafyeva, and I. Cherniak (2016), GPS and GLONASS observations of large-scale traveling ionospheric disturbances during the 2015 St. Patrick's Day storm, J. Geophys. Res. Space Physics, 121, 12,138-12,156, doi:10.1002/2016JA023332.

Zhang, S.-R., Erickson, P. J., Zhang, Y., Wang, W., Huang, C., Coster, A. J., Holt, J. M., Foster, J. C., Sulzer, M., and Kerr, R. (2017). Observations of ion-neutral coupling associated with strong electrodynamic disturbances during the 2015 St. Patrick's Day storm. Journal of Geophysical Research: Space Physics. http://doi.org/10.1002/2016JA023307

Zhang S.- R., P. J. Erickson, L. Goncharenko, A.J. Coster, W. Rideout, and J. Vierinen (2017), Ionospheric bow waves and perturbations induced by the 21 August 2017 solar eclipse, Geophys. Res. Lett., 44, doi:10.1002/2017GL076054.

Zhang, D. H., Z. Xiao, and Q. Zhang (2002), The correlation of flare's location on solar disc and the sudden increase of total electron content, Chin. Sci. Bull., 47, 82-85, doi:10.1360/02tb9017.

Zhang, D. H., and Z. Xiao (2003), Study of the ionospheric total electron content response to the great flare on 15 April 2001 using the International GPS Service network for the whole sunlit hemisphere, J. Geophys. Res., 108, 1330, doi:10.1029/2002JA009822, A8.

Zhang, R., L. Liu, H. Le, and Y. Chen (2017), Equatorial ionospheric electrodynamics during solar flares, Geophys. Res. Lett., 44, 4558-4565, doi:10.1002/2017GL073238.

947 Zhu, J., and A. J. Ridley (2015), Modeling subsolar thermospheric waves during a
948 solar flare and penetration electric fields, J. Geophys. Res. Space Physics, 119, pages
949 10,507-10,527. doi:10.1002/2014JA020473.

Figure 1. Solar geophysical parameters during 6-10 September 2017, including hourly IMF Bz and By, solar wind speed, AE index, and Kp index. Green lines represent the peak times of solar flares that are the subject of this study.

Figure 2. Solar flux at 0.1-0.8 nm measured by GOES-15 for three major X-class flare events on 6, 7 and 10 September 2017 (panels (a), (c) and (e)), and corresponding ionospheric fluctuations measured as CONUS median differential TEC (CMDT) for the three flare events (panels (b), (d) and (f)). A quiet day reference for 9 September 2017 is also given in (d, gray line) All CMDT data are based on 30-min sliding window filtering except for the dotted red curve in (b) using a 1-hr sliding window filtering. These curves show clear continental-size fluctuations following the flares. The fluctuations marked as vertical green solid lines are rapid ionospheric responses to flare bursts, and the dashed lines are post-flare oscillations/TIDs induced by the three major X-class events.

Figure 3. Ionospheric TEC perturbations on 6 September 2017, sort into four categories (a-d; see text) derived using a 30-min sliding window for the Savitzky-Golay filter. Shown in each panel are original vertical TEC data from an individual ground receiver looking at an individual GNSS satellite (an individual receiver-satellite pair) (blue), background TEC values determined with the filter (red) and differential TEC (black). See text for category descriptions.

Figure 4. Temporal evolution of differential TEC (ΔTEC) within 42.5±2 °N latitudes on 6 September 2017 for three longitudes, 85±0.25 °W (pink dots), 92±0.25 °W (blue dots), and 100±0.25 °W (black dots). Pink dots and black dots are shifted upward and downward, respectively, by 0.6 TECu for clarity. Vertical green link marks the flare peak time, and other short vertical lines mark the sunrise times, color-coded by longitudes. Disturbance data are derived using a 60-min sliding window for the Savitzky-Golay filter.

Figure 5. FFT Analysis of differential TEC periodicities during 12:30-15:30 UT for 6, 9, and 15 September. Average spectrum amplitudes and corresponding standard error for given periods are calculated and shown in the left panel; also provided for comparisons are the spectrum results for 12:30-14:30 UT (post-flare) and 07:00-0900 UT (pre-flare at night) on 6 September. The locations of significant oscillations at several periods whose amplitude are prominent during a particular day are shown in the right panel; only oscillations with amplitudes above the mean level by 3 standard divisions for a corresponding period are provided.

Figure 6. 2-dimensional ΔTEC (10^{16} el/m^2 unit) maps over CONUS on 6 September 2017 at pre-flare time 11:40 UT (a), a few minutes after the flare peak at 12:09 UT (b), one hour after the flare peak at 13:02 UT (c), and further later at 15:54 UT (d). The shaded area is the nightside. The 30-min sliding window filtering is used. Note the change in the color scale across different panels. The black box area is near solar terminator with wave fronts immediately following the flare peak; the yellow box area contains various post-flare wave fronts under influences of potentially flare-induced waves and other waves. The magenta box contains solar-terminator related disturbances or waves. A faint wave front in (c) (white dashed line) appears related to a pre-flare weak magnetic disturbance at ~10:00 UT.

Figure 7. Same as Figure 5 of 2-dimensional TID maps over CONUS on 6 September 2017 but with a high cadence within 16 min of the flare peak at 12:10 UT (a), 12:11 UT (b), 12:13 UT (c), and 12:18 UT (d). Along with Figure 5b for 12:09 UT, these maps show the post-flare TID occurrence and initial evolution. Note the change in the color scale across different panels. The black box area is near solar terminator with wave fronts immediately following the flare peak; the magenta box contains solar-terminator related disturbances or waves.

Figure 8. Post-flare 2-D ΔTEC (10^{16} el/m^2 unit) maps at 12:11 UT derived using a 30-min sliding window (a) and a 60-min sliding window (b) for the Savitzky-Golay filter. Panel (a) is the same as Figure 4d. Note the change in the color scale between the two panels. In the black box near the solar terminator, a group of wave fronts can be identified and some of them are marked with black arrowheads. The magenta box area is in the northeast US where wave fronts are also visible; this was the region fluctuations existed before the flare as indicated in Figure 5a.

Figure 9. Keograms of pre- and post- flare TID propagation in ΔTEC (10^{16} el/m^2 unit) in the zonal direction at fixed latitudes of ~ 40°N, derived using 30-min sliding window filtering. Eastward propagation perpendicular to the direction of sunrise terminator (shown as blue areas) can be identified during post-flare hours. The prominent blue and red signature aligned vertically across longitude near 12:00 UT is associated with the flare impact on the sudden ionization enhancement and the filter response to the enhancement (see text), while the diagonal blue stripe is associated with the sunrise terminator.

Figure 10. Same as Figure 9 but for 60-min sliding window filtering. This shows post-flare variations of the larger amplitude and longer period fluctuations.

Figure 11. Cross-correlation analysis of keogram similar to Figure 9 but at ~45°N to visualize delays between longitudes in order to estimate the TID zonal propagation within -100 – -70 °E and 12:30 – 14:30 UT (a). The higher correlation at 120 min simply implies the data length analyzed is 2 hours. The periodicity of the brightness in vertical direction (see vertical small arrowheads) indicating synchronized oscillations is ~ 40-50 min. The white arrowhead lines are parallel to the bright bands of high cross correlation across longitude and time. Panel (b) shows a similar analysis of keogram at -80±0.5°E within 30 – 45°N and 12:30-14:30 UT, indicating equatorward TID propagation. Long white arrowheads represent an equatorward propagation; short vertical arrowheads mark the 40-50 min synchronized oscillations.

Figure 12. Ionospheric F2 region expansion/up-welling following the solar flare on 6 September 2017 as measured in vertical ion drift by the Millstone Hill incoherent scatter radar. The vertical green line indicates the flare maximum time. For comparison with similar conditions but on a non-flare day, observations during 8 September 2010 are also shown (dotted lines).

Figure 13. Millstone Hill ISR observations during the X17.0 solar flare on 7 September 2005 with electron density (a), electron temperature (b), and vertical drift (c). GOES-12 solar X-ray flux at 1-8Åis shown in (d).

Figure 14. Millstone Hill ISR plasma-line measurements of NmF2 (top) and NmF1 (bottom) with a 1-min cadence during the 6 September 2017 solar flare. Blue lines are measured data, gray dotted lines are derived using a 30-min sliding window for the Savitzky-Golay filter. Red dotted lines are the relative electron density changes. Measurement uncertainty associated with the plasma-line data is at 0.1% level. Post-sunrise NmF1 was not measurable until the flare onset.

Figure 15. Longitudinal variations of TEC disturbances Δ TEC at 42.5±1.5 °N (a) and their relative variations ΔTEC/TEC (b), before (black), at the peak of (blue), and after (pink) the solar flare on 6 September 2017. Disturbance data are derived using a 30-min sliding window for the Savitzky-Golay filter (see text).

Figure 16. Large scale traveling ionospheric disturbances as in ΔTEC (10^{16} el/m^2 unit) launched by strong magnetic disturbances on 8 September 2017 (see Figure 1). The characteristic wave fronts along geomagnetic latitudes (in the zonal direction) are very evident. Disturbance data are derived using a 30-min sliding window for the Savitzky-Golay filter (see text).

Figure 17. 2-D ΔTEC (10^{16} el/m^2 unit) maps on 5 September 2017, the day before the flare, at 12:07 UT (a), 12:11 UT (b) and 13:!6 UT (c) derived using a 30-min sliding window. Black arrowheads represent the terminator related wave front alignments and the white curve is the wave front in zonal direction caused likely by high latitude disturbances.

Figure 1.

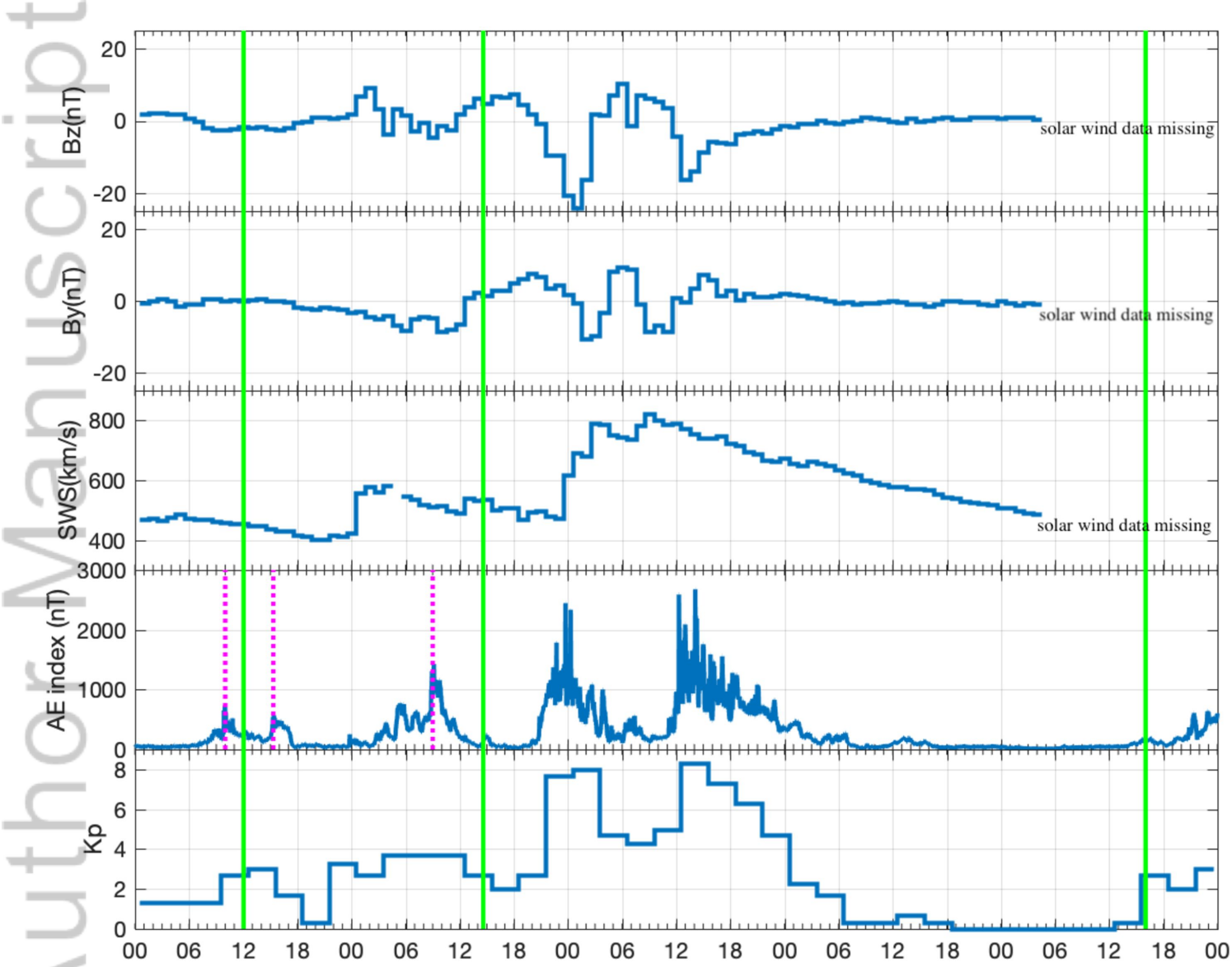

Figure 2.

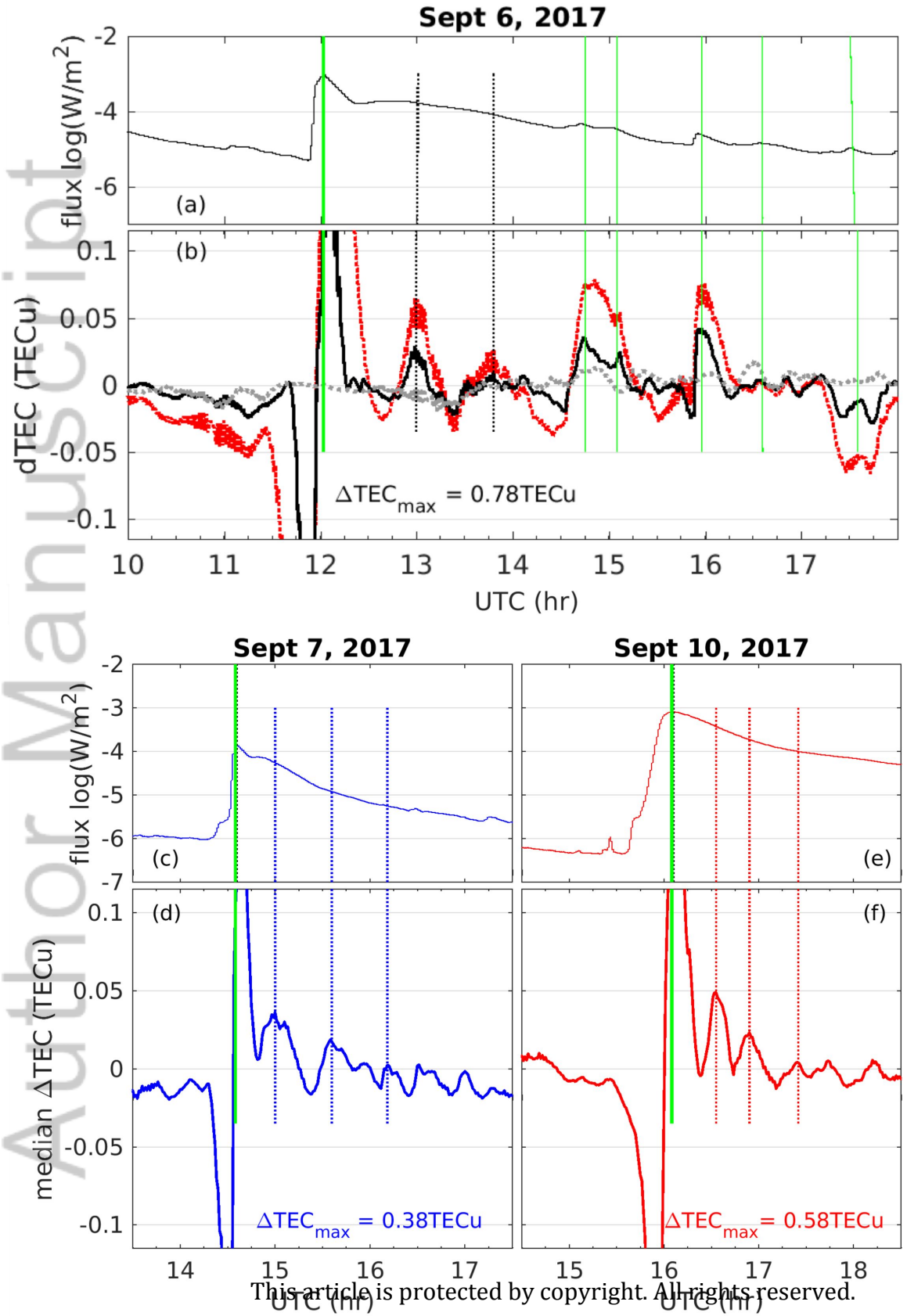

Figure 3.

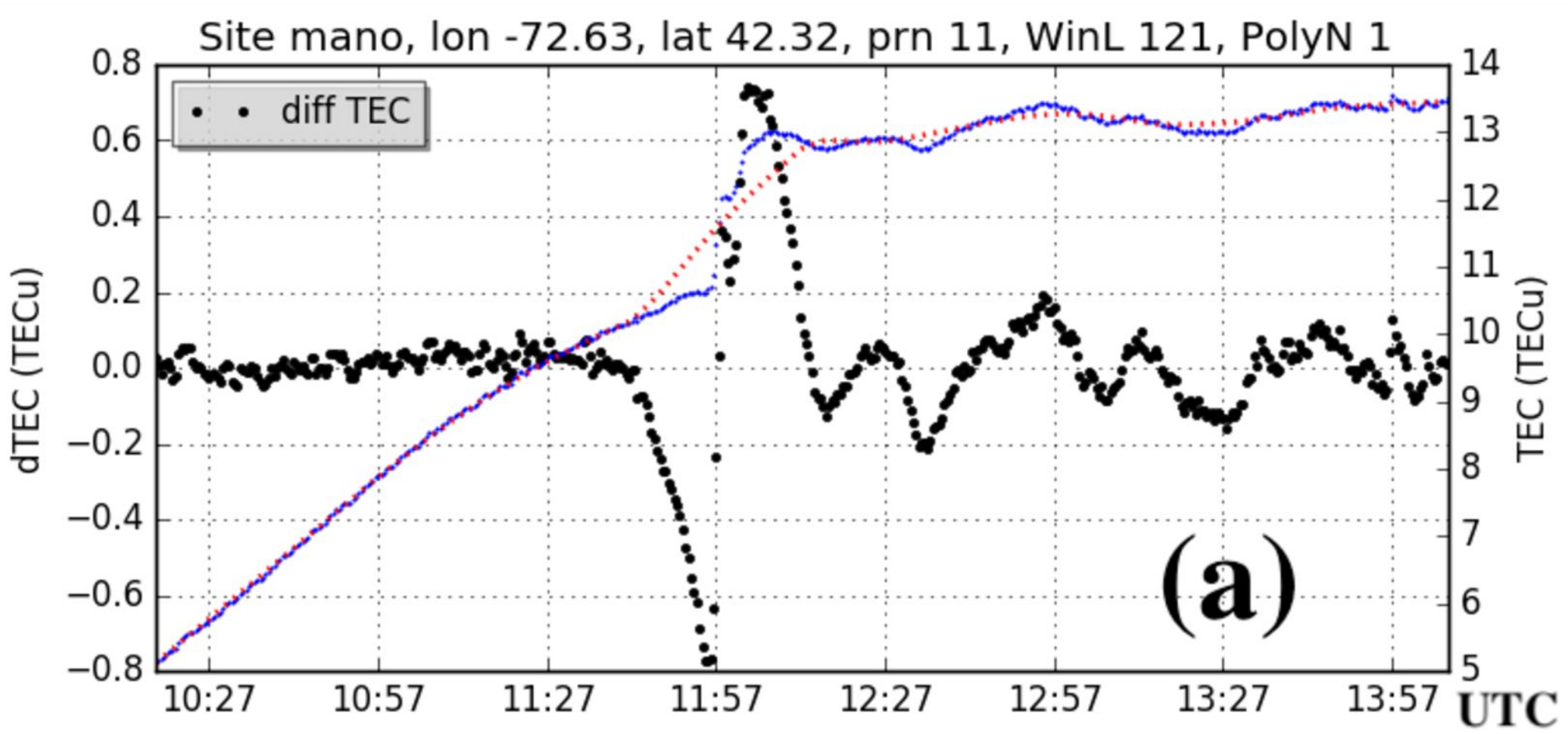

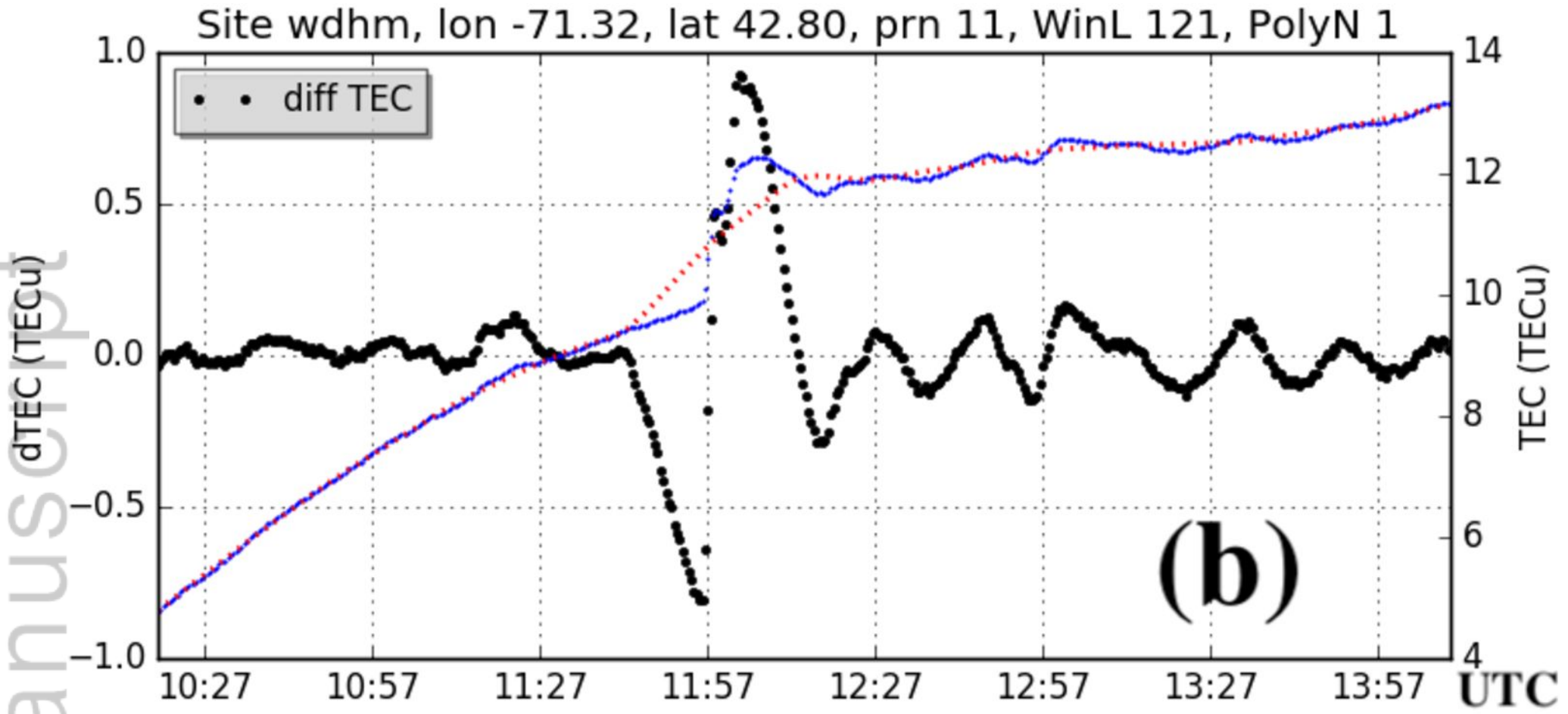

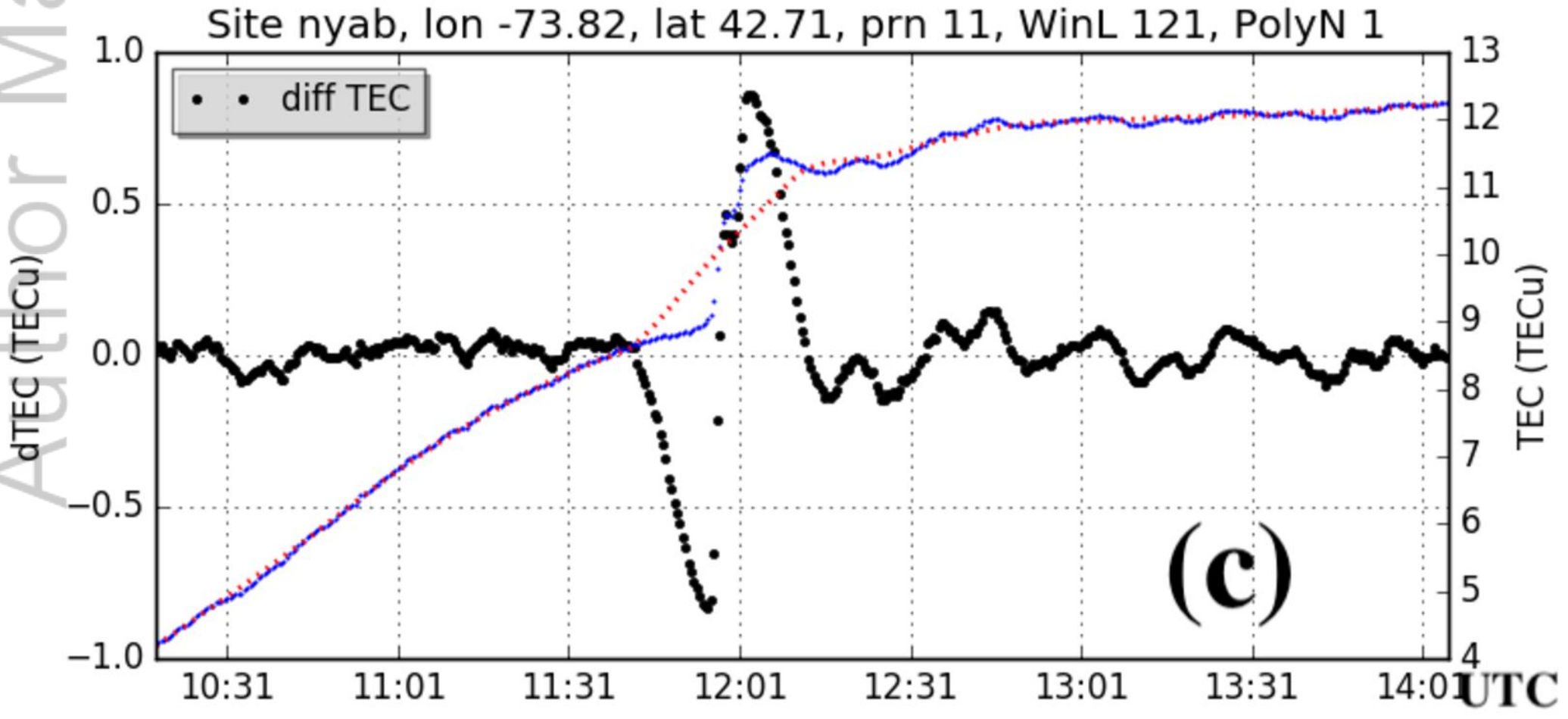

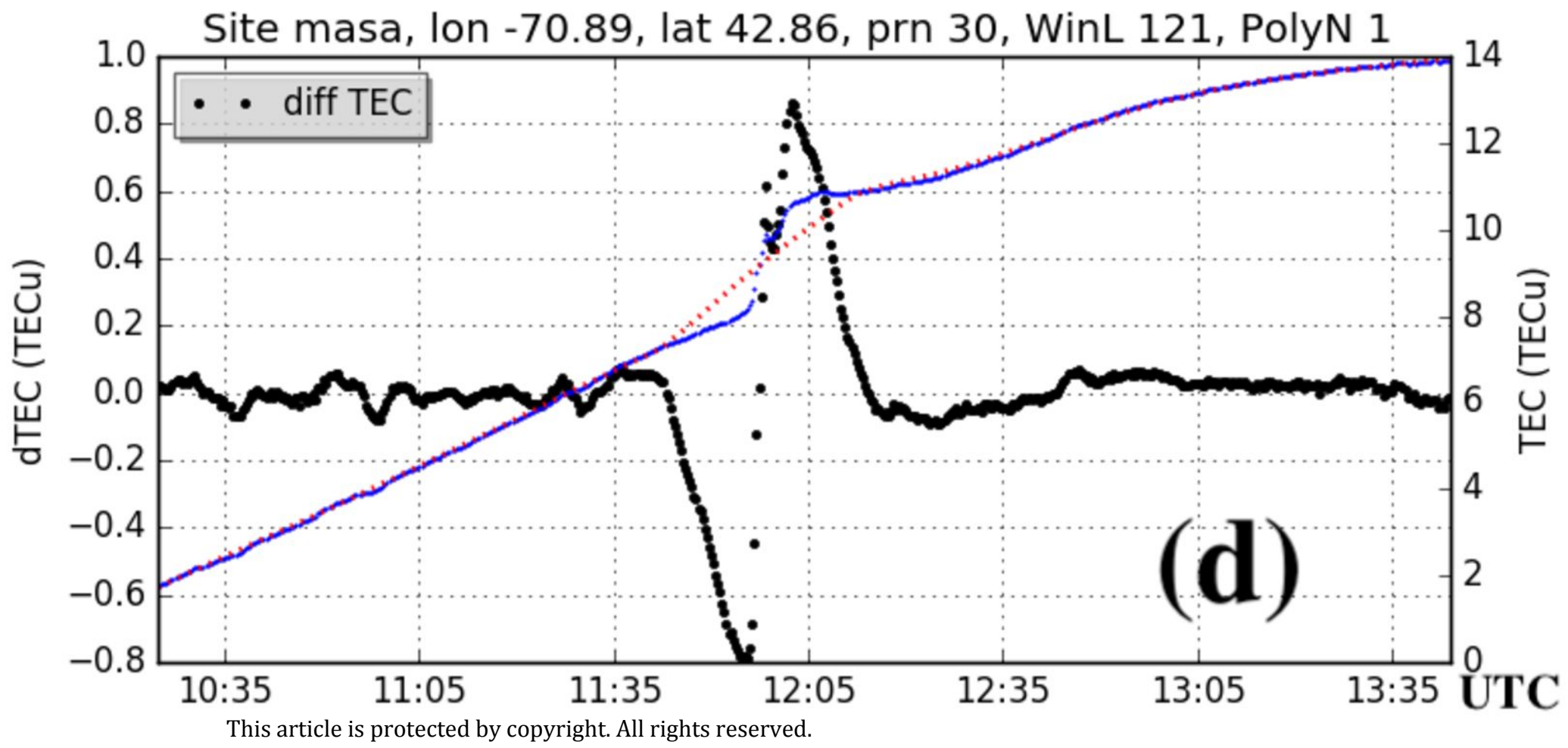

Figure 4.

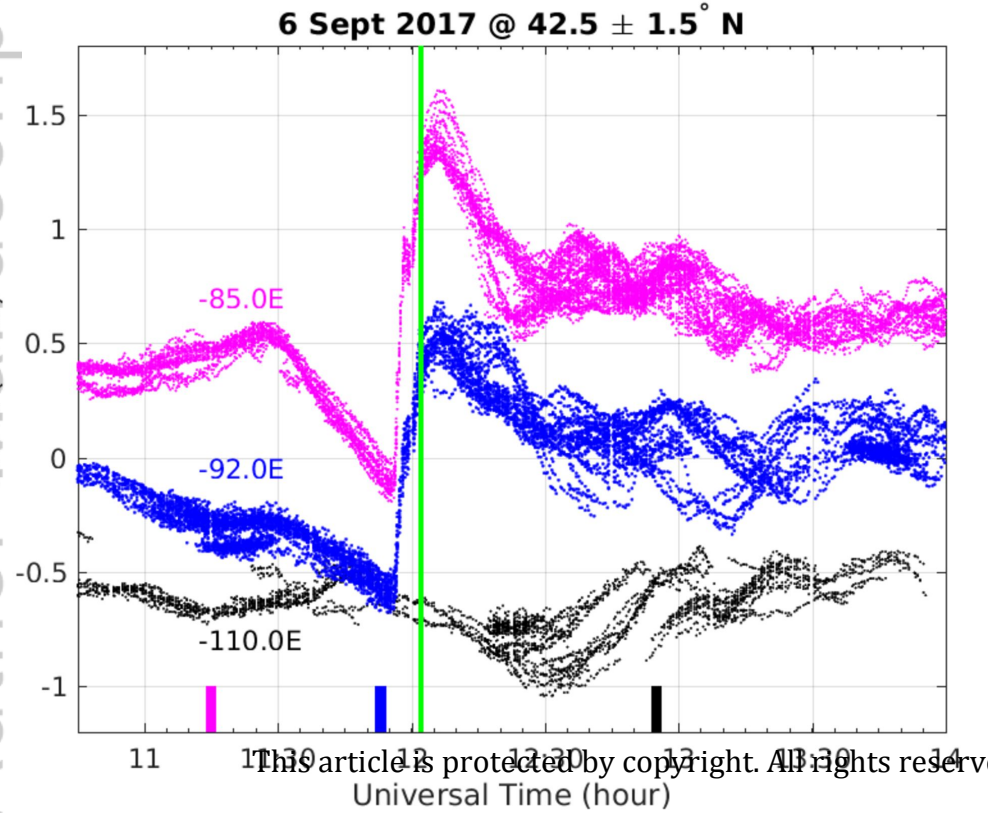

Figure 5.

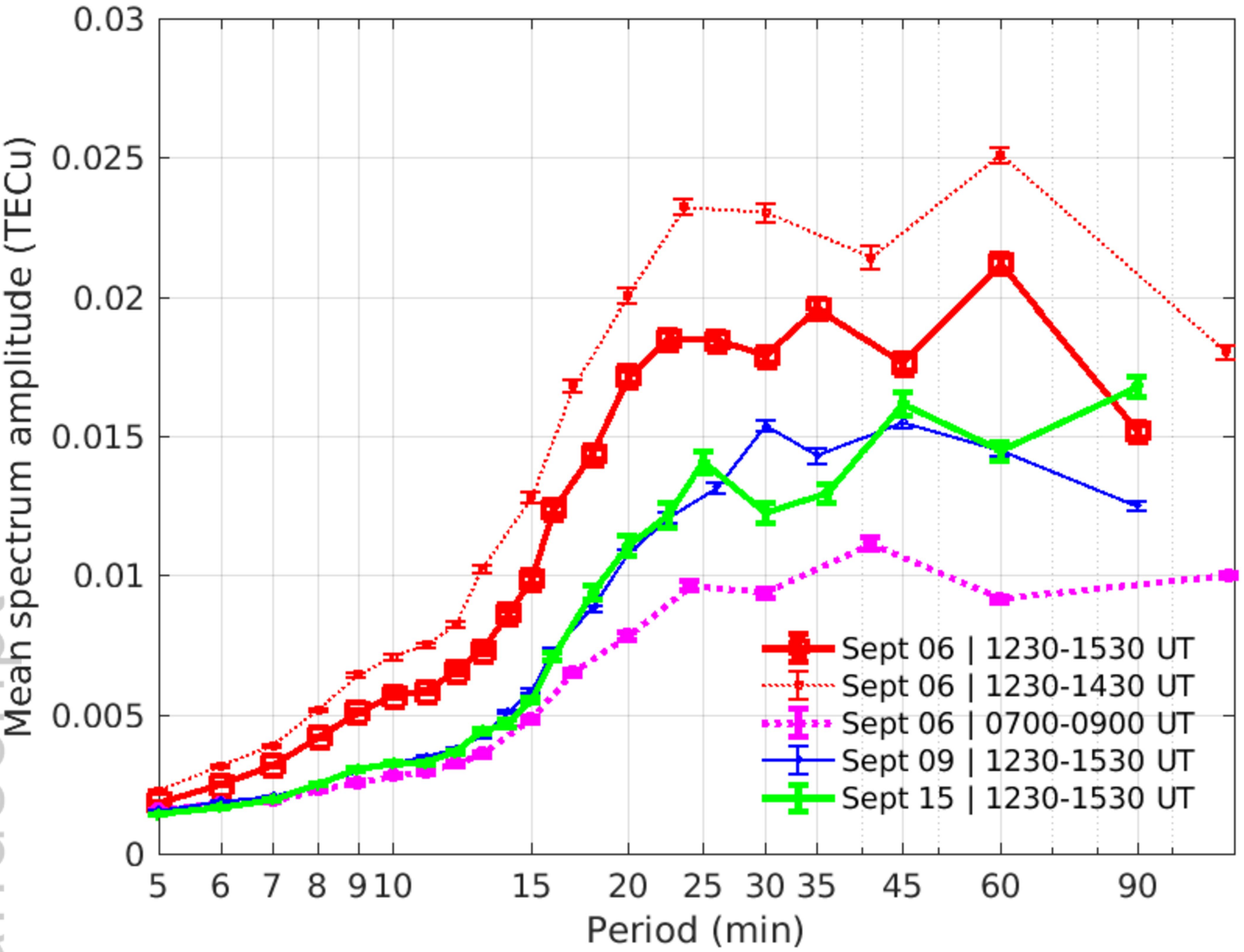

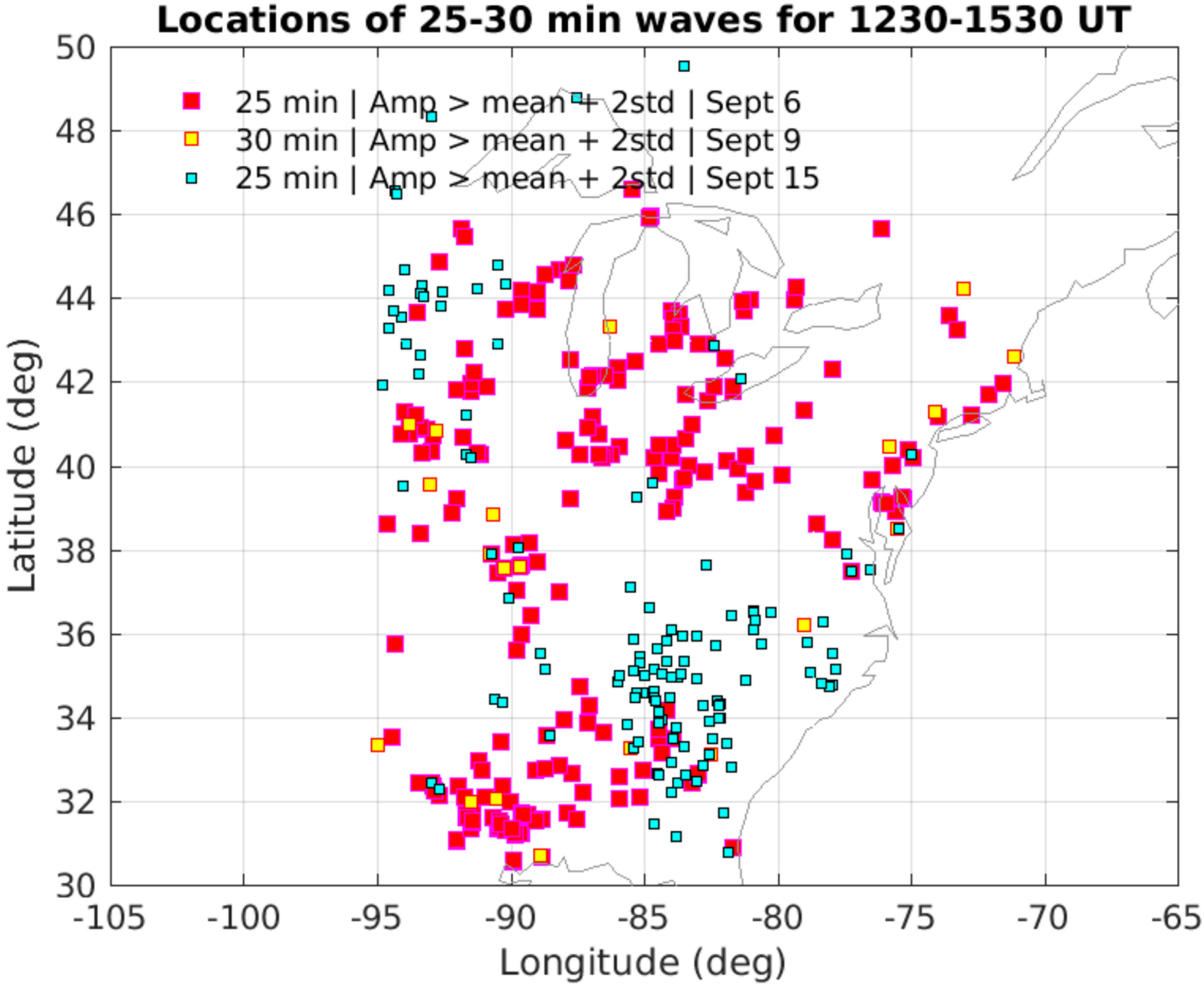

Figure 6.

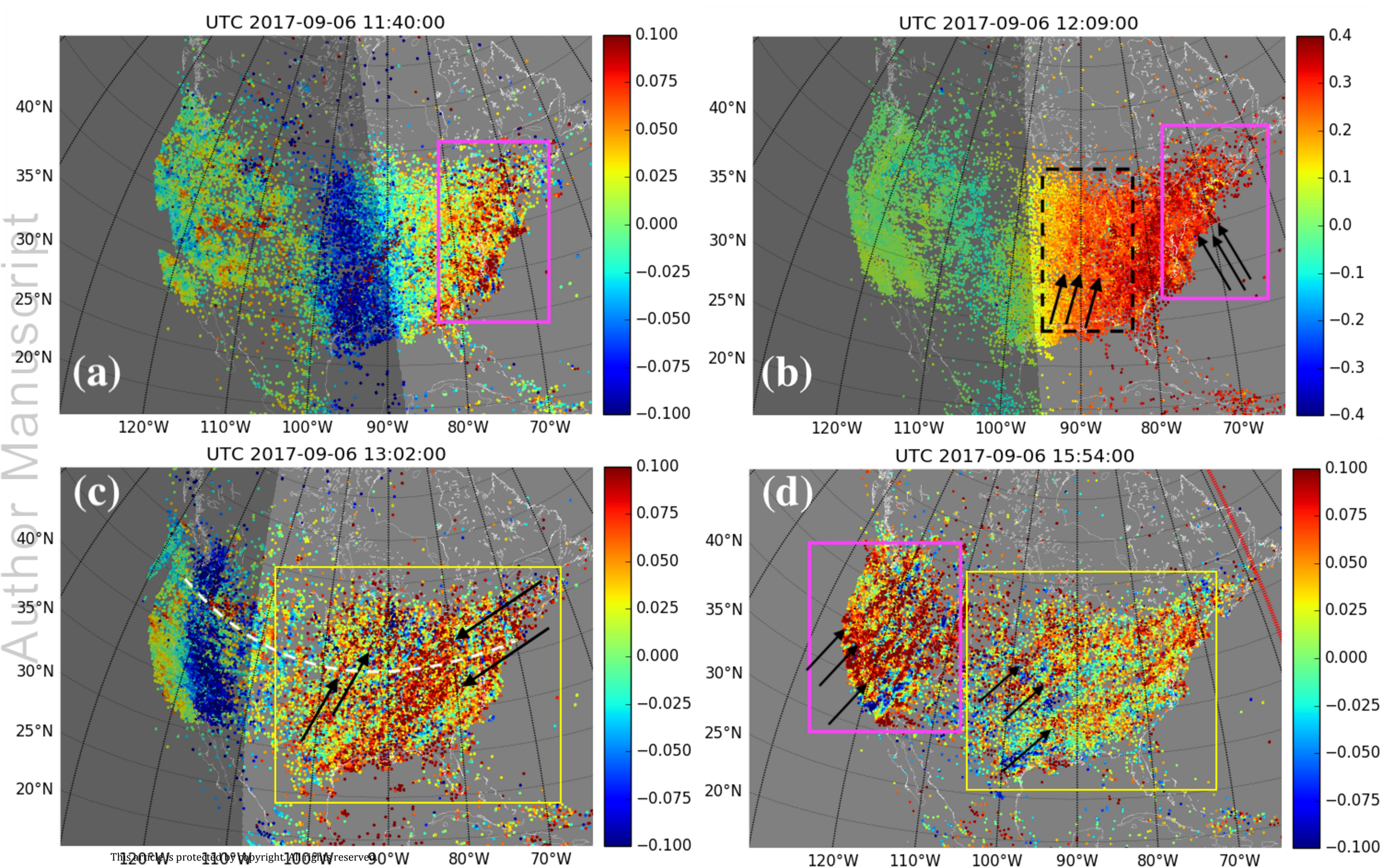

Figure 7.

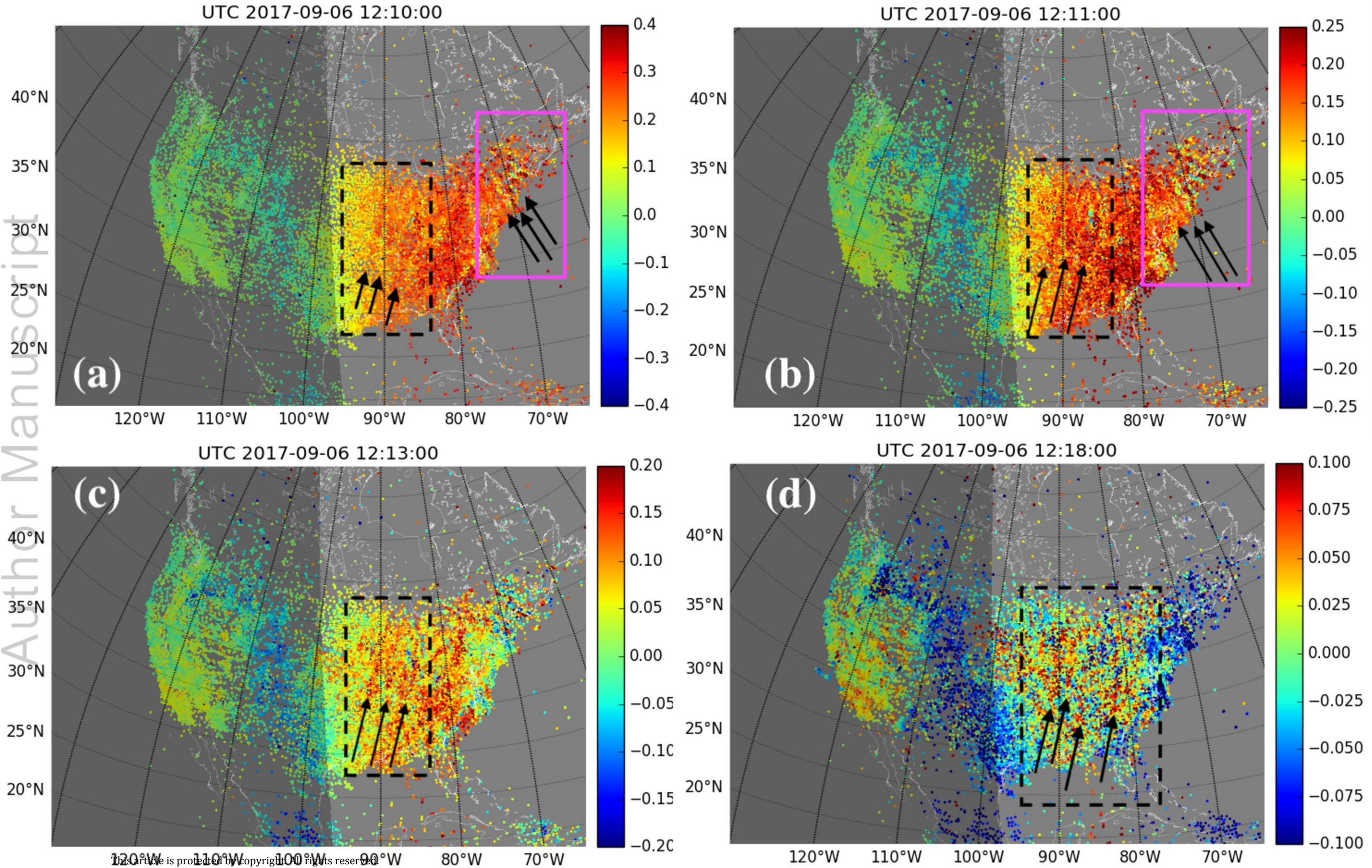

Figure 8.

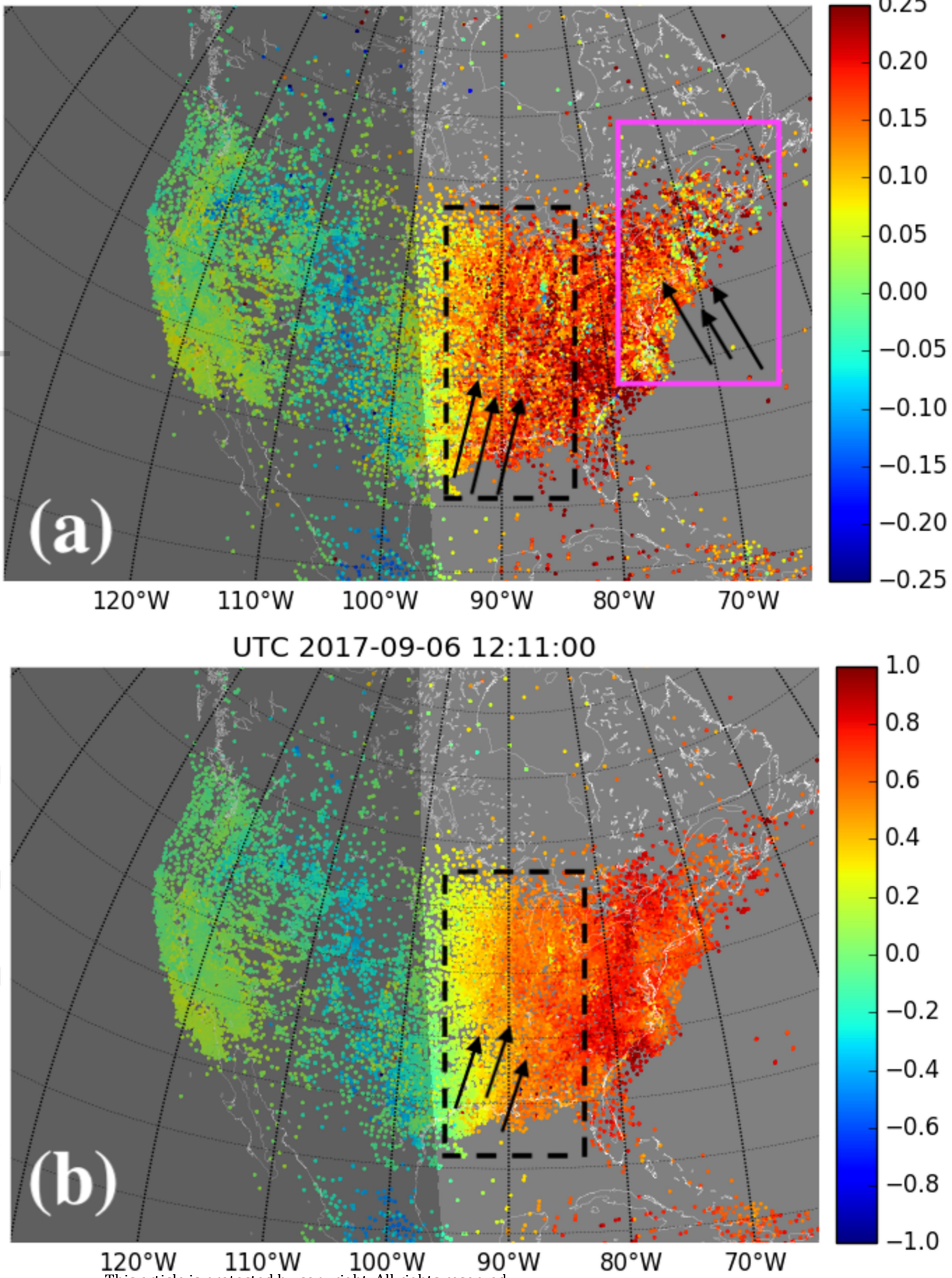

Figure 9.

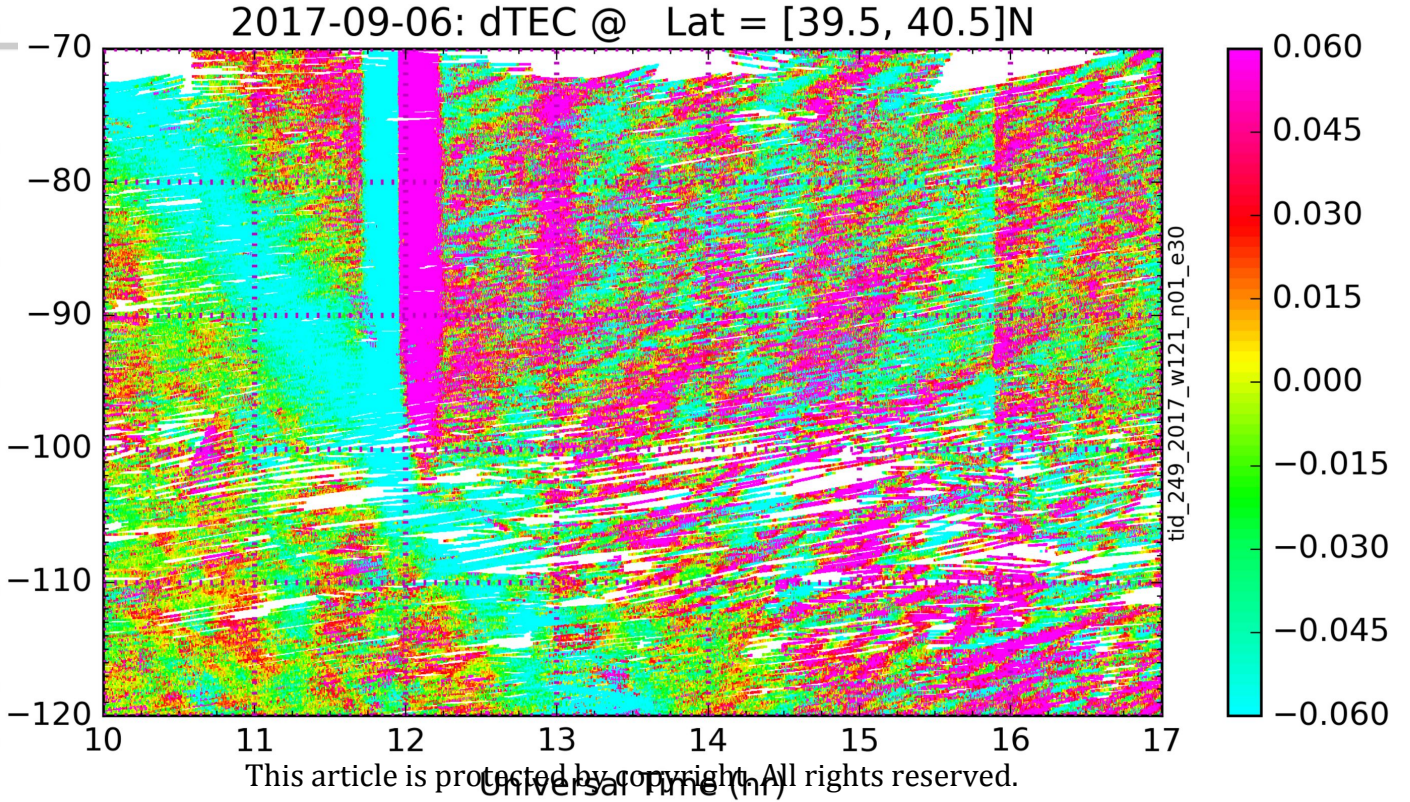

Figure 10.

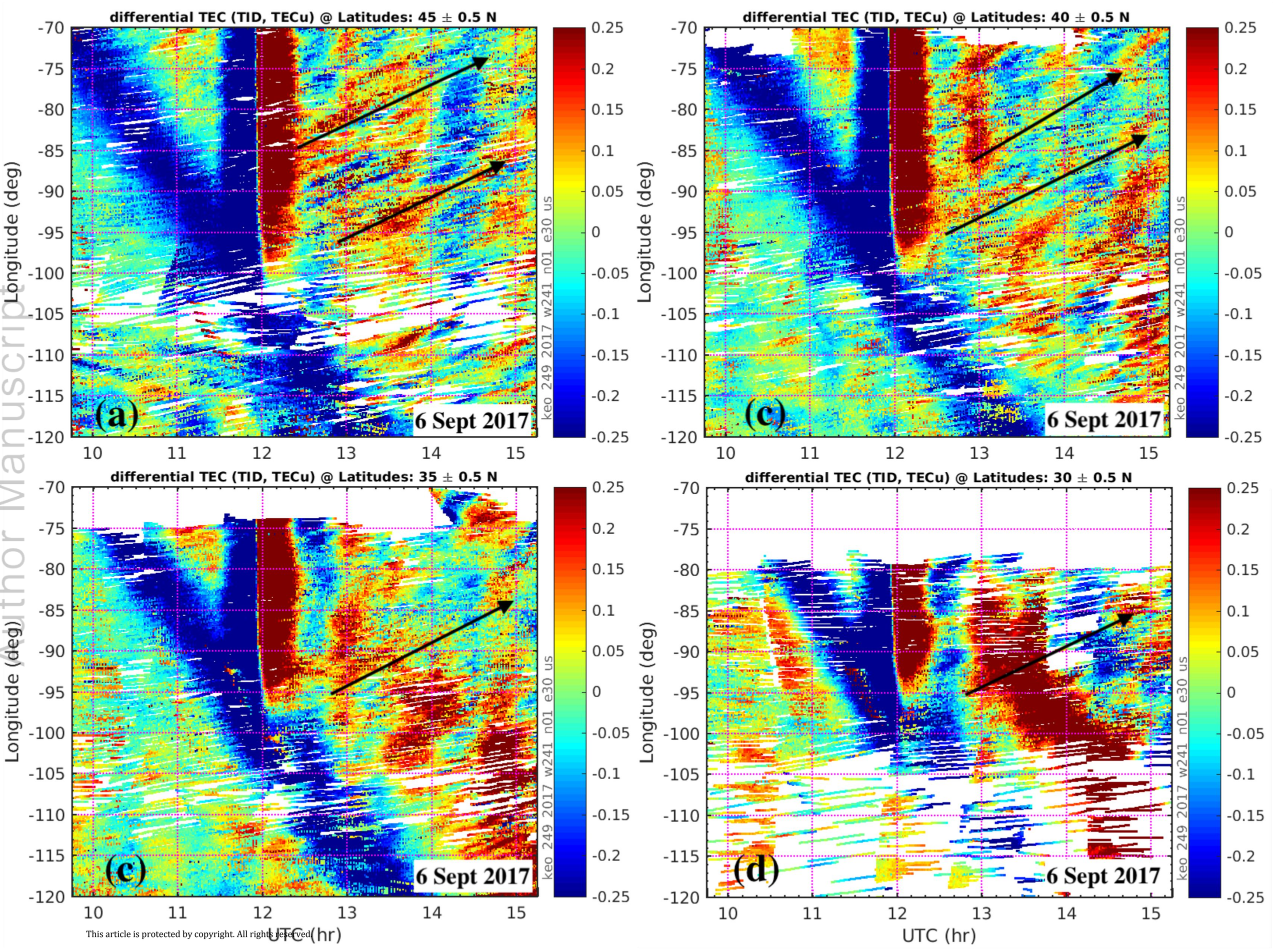

Figure 11.

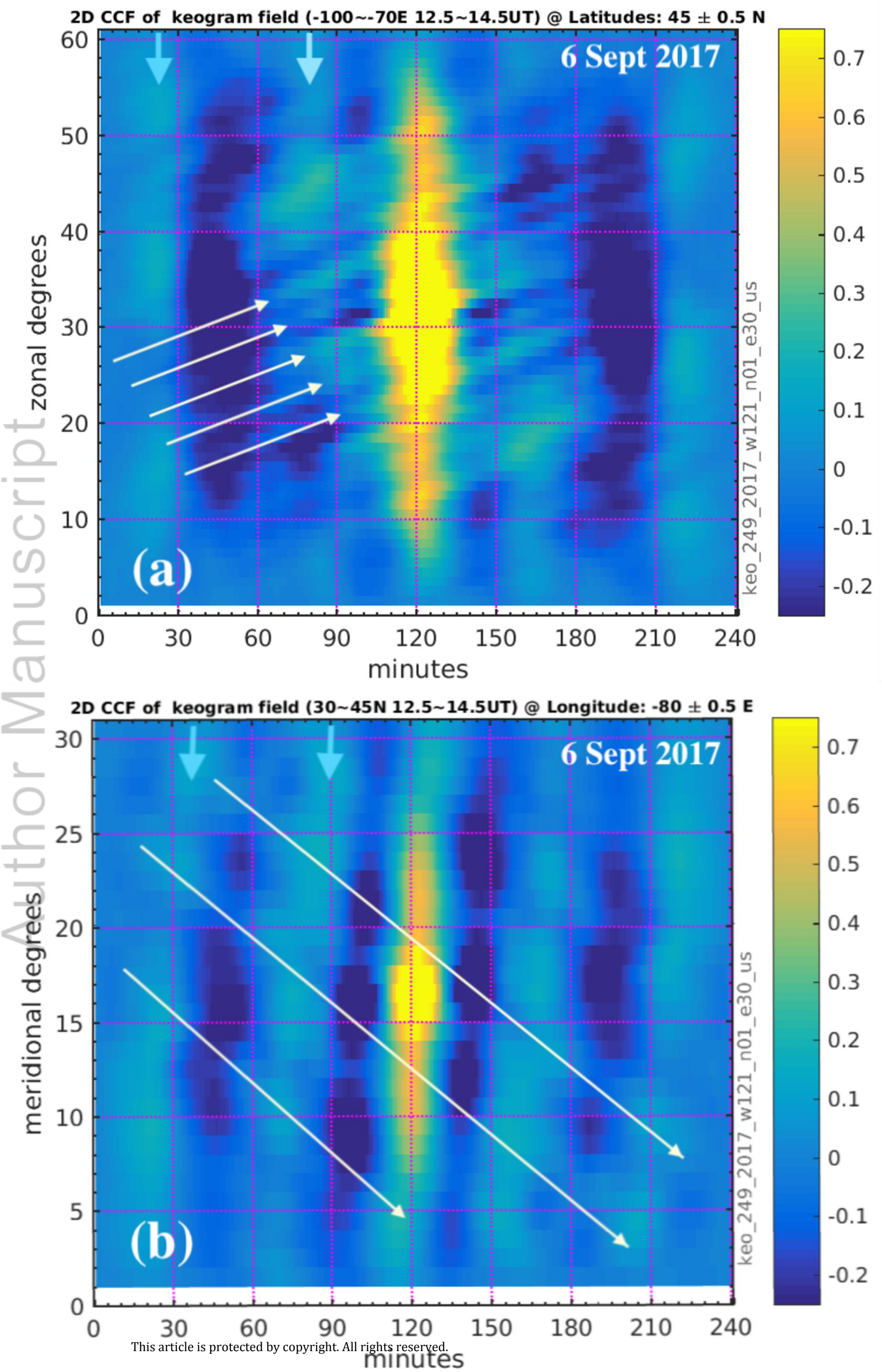

Figure 12.

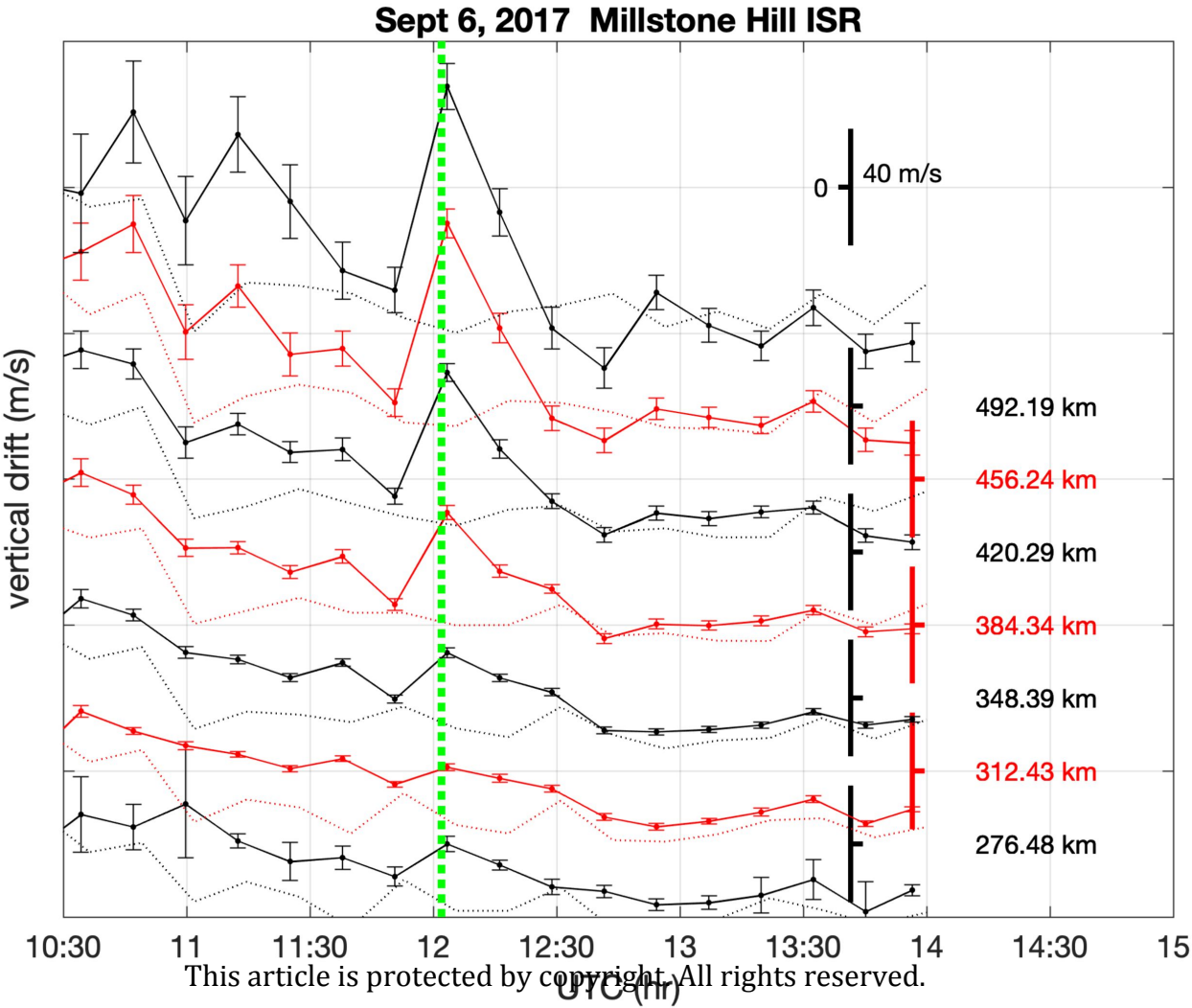

Figure 13.

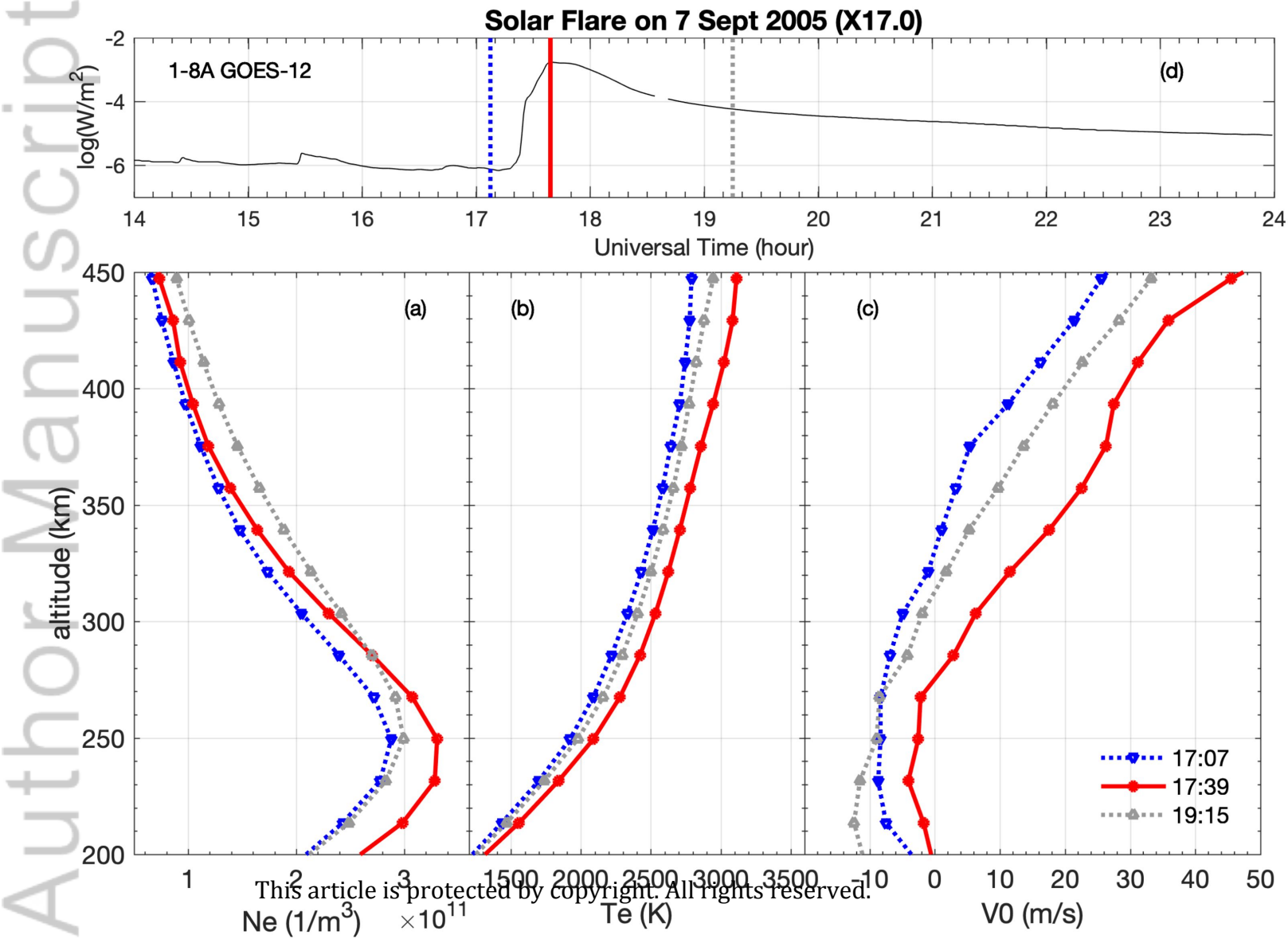

Figure 14.

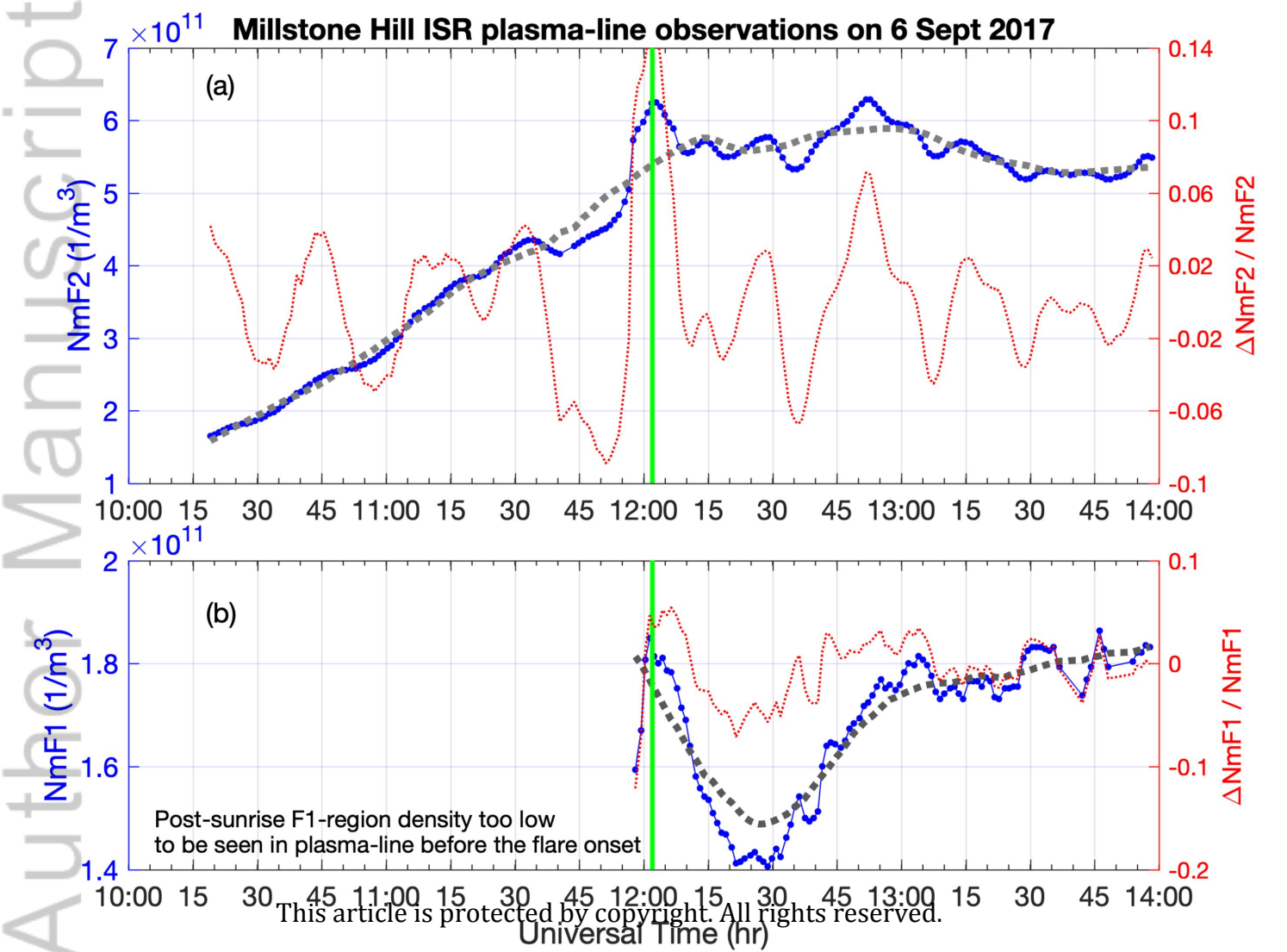

Figure 15.

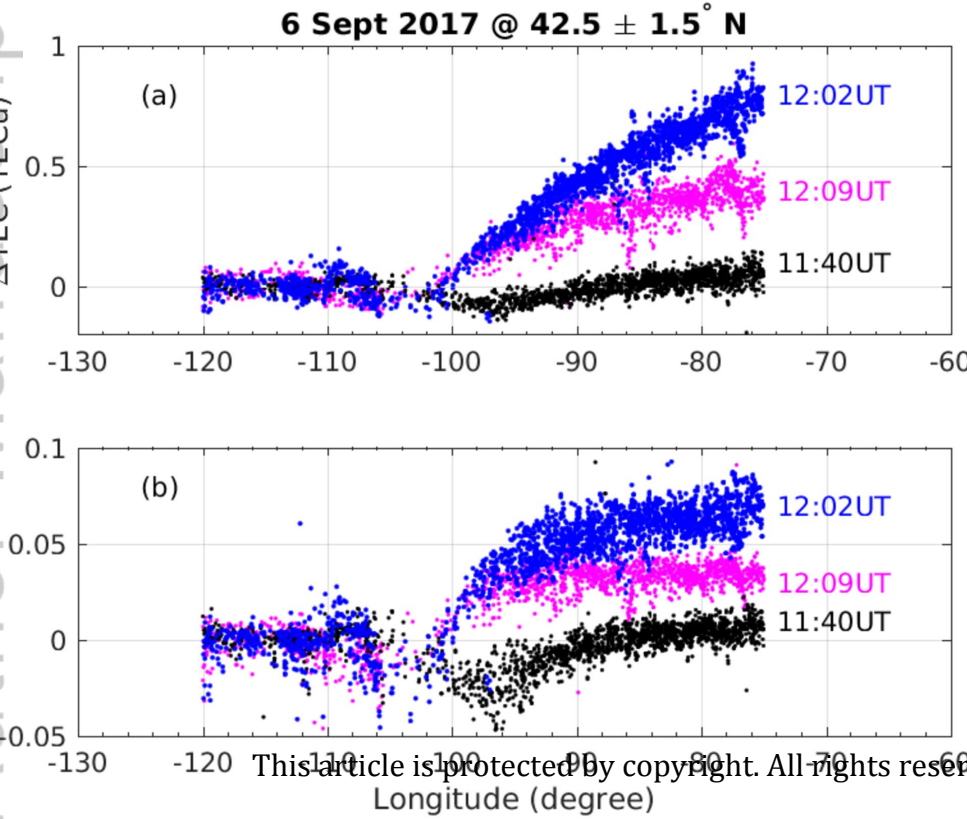

Figure 16.

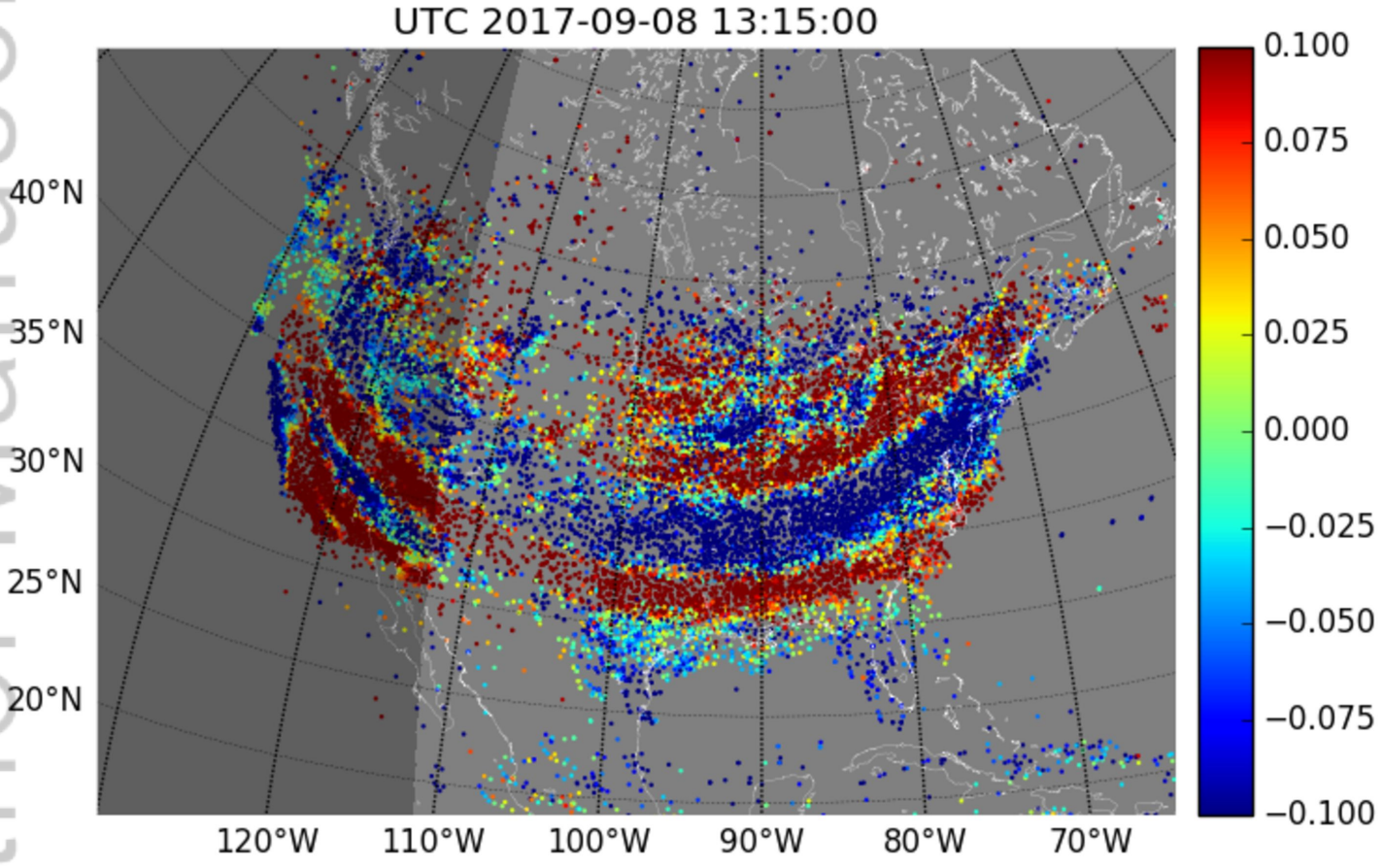

Figure 17.

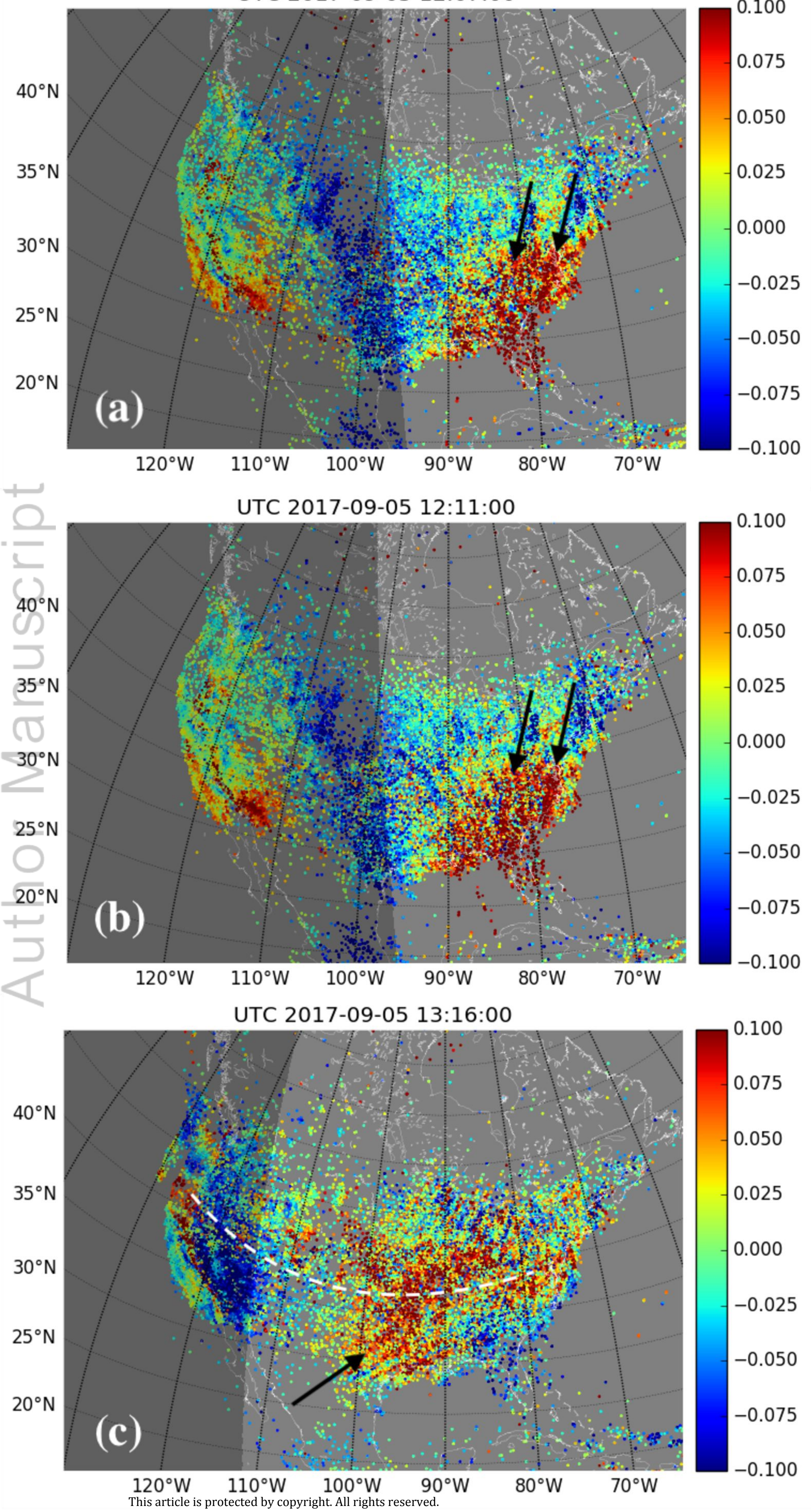

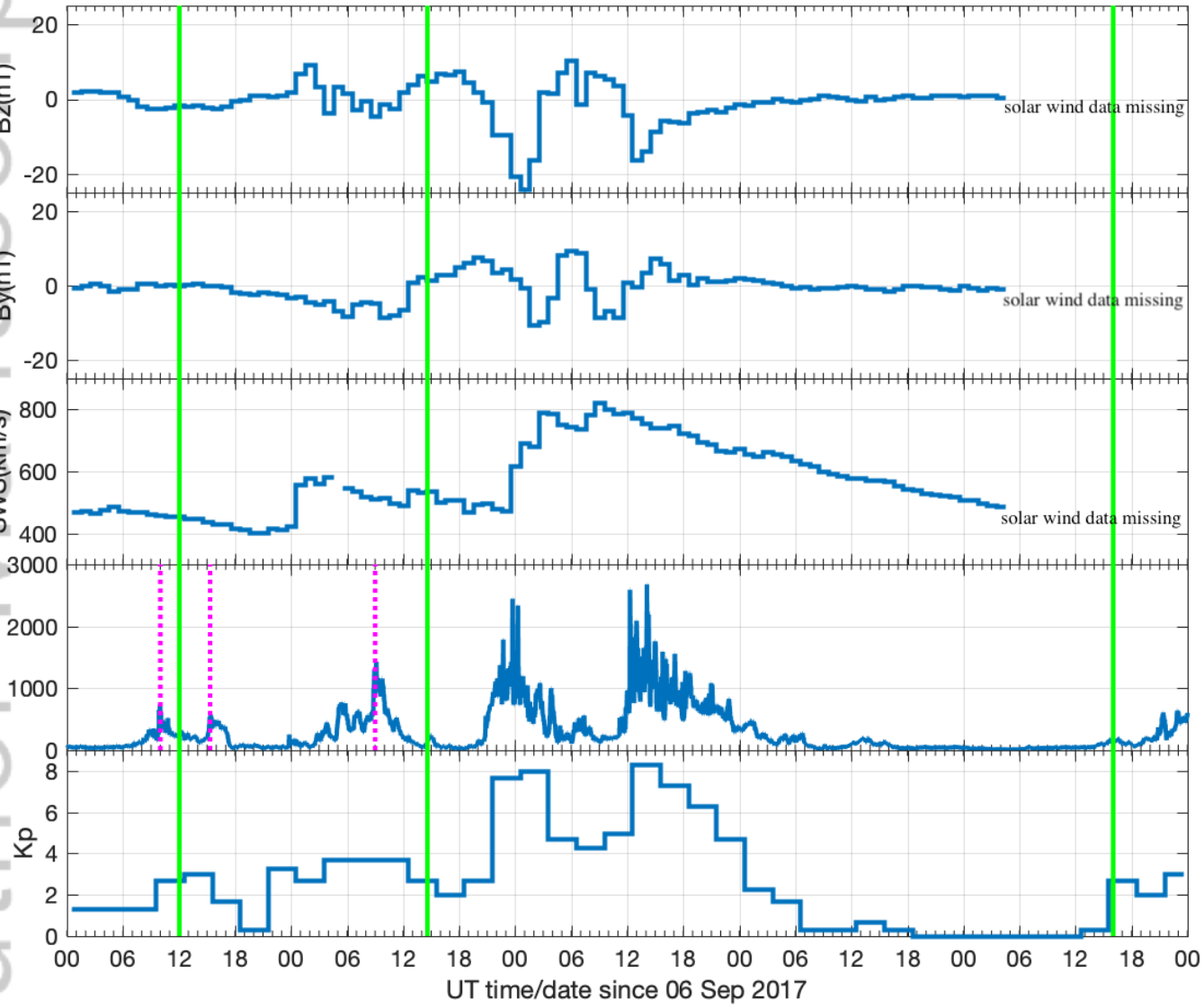

2019JA026585-f01-z-.png

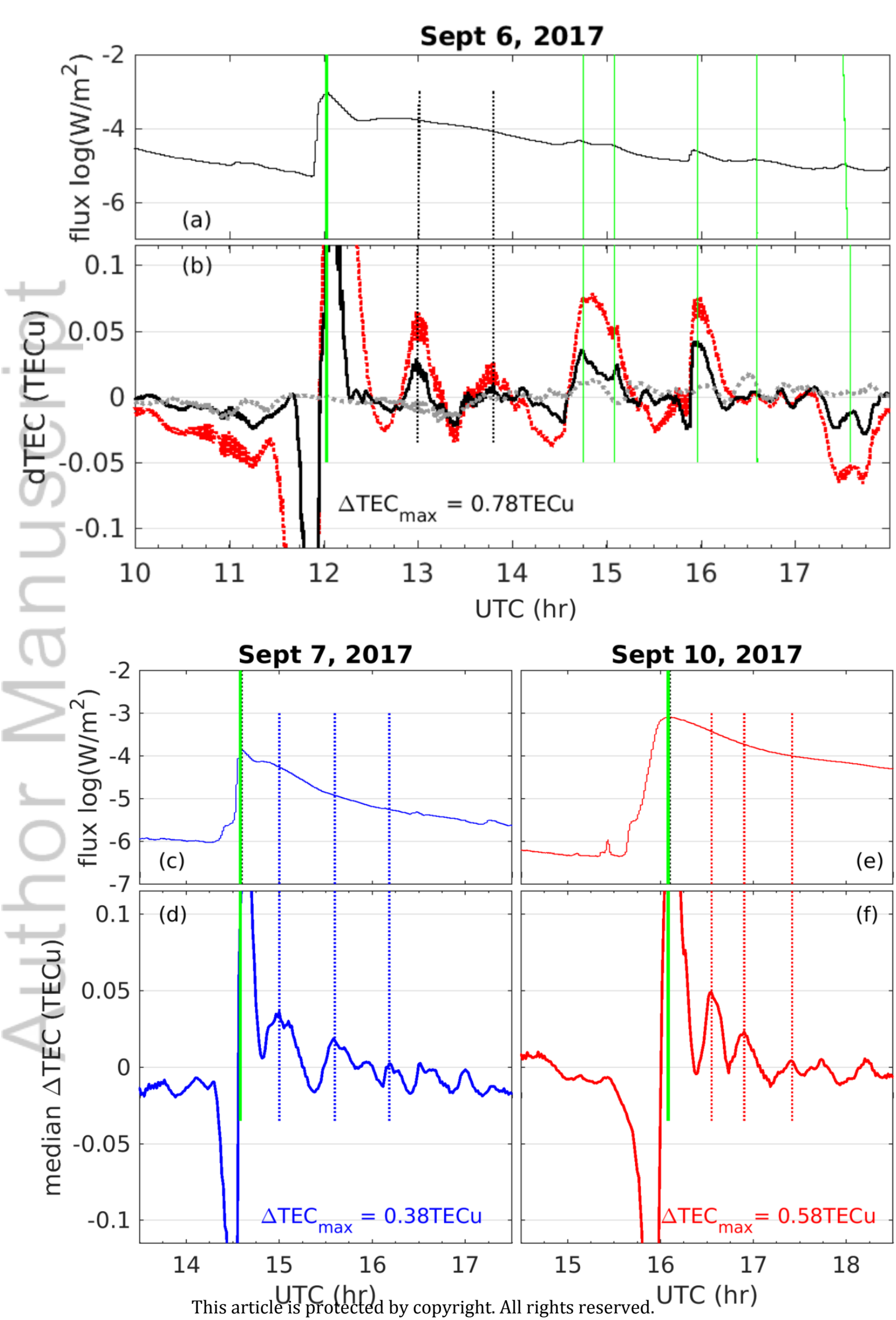

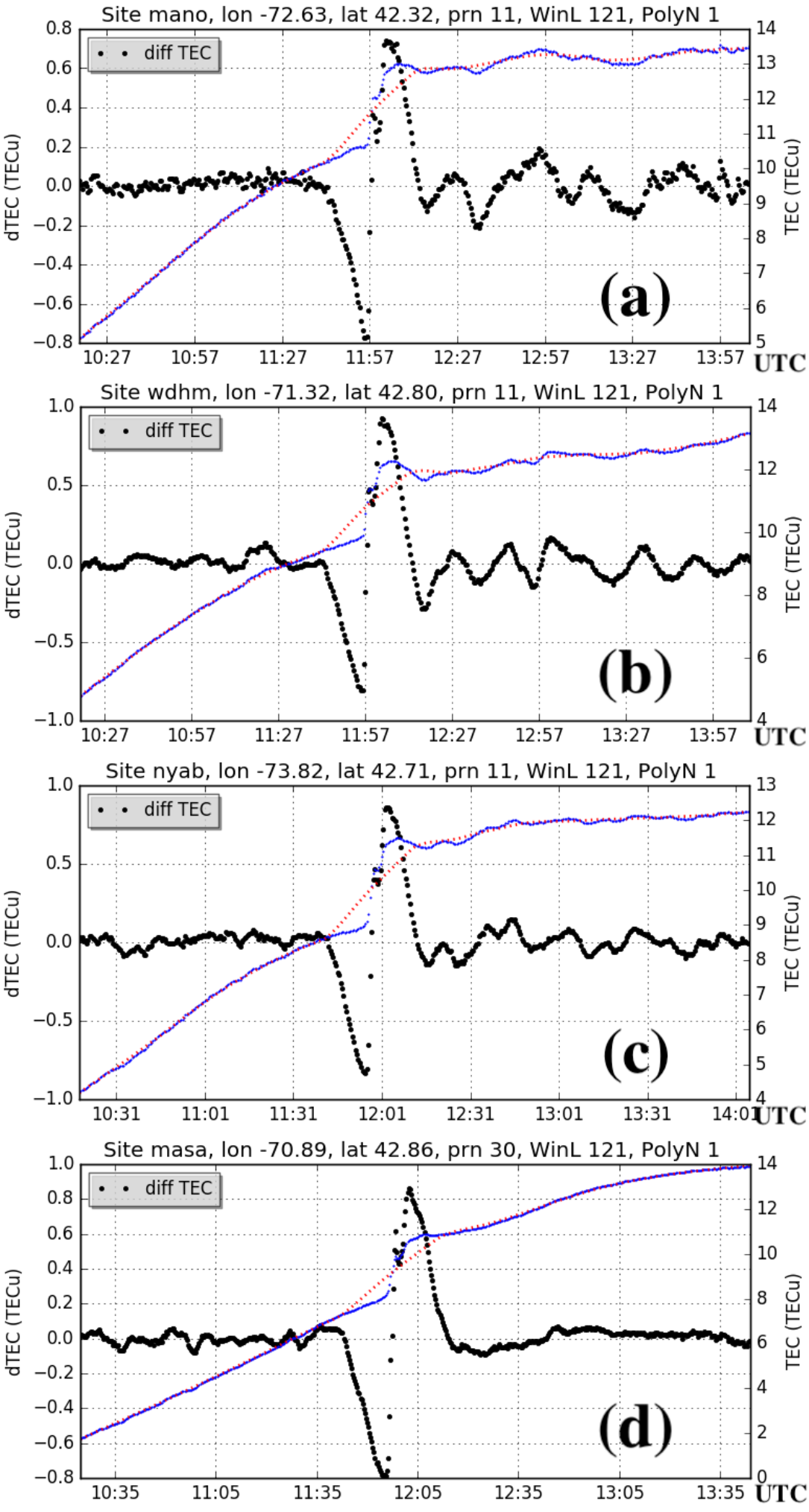

2019JA026585-f03-z-.png

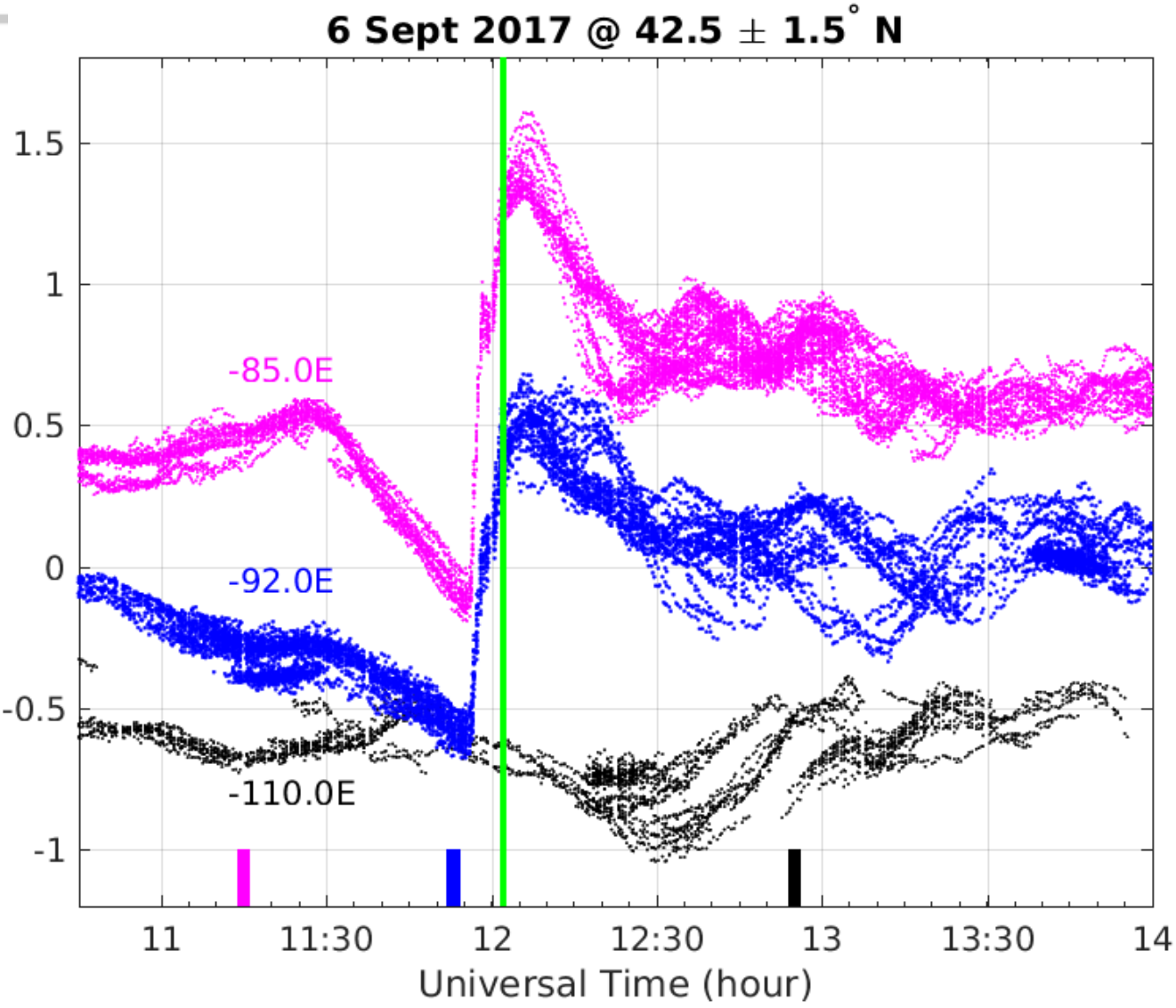

2019JA026585-f04-z-.png

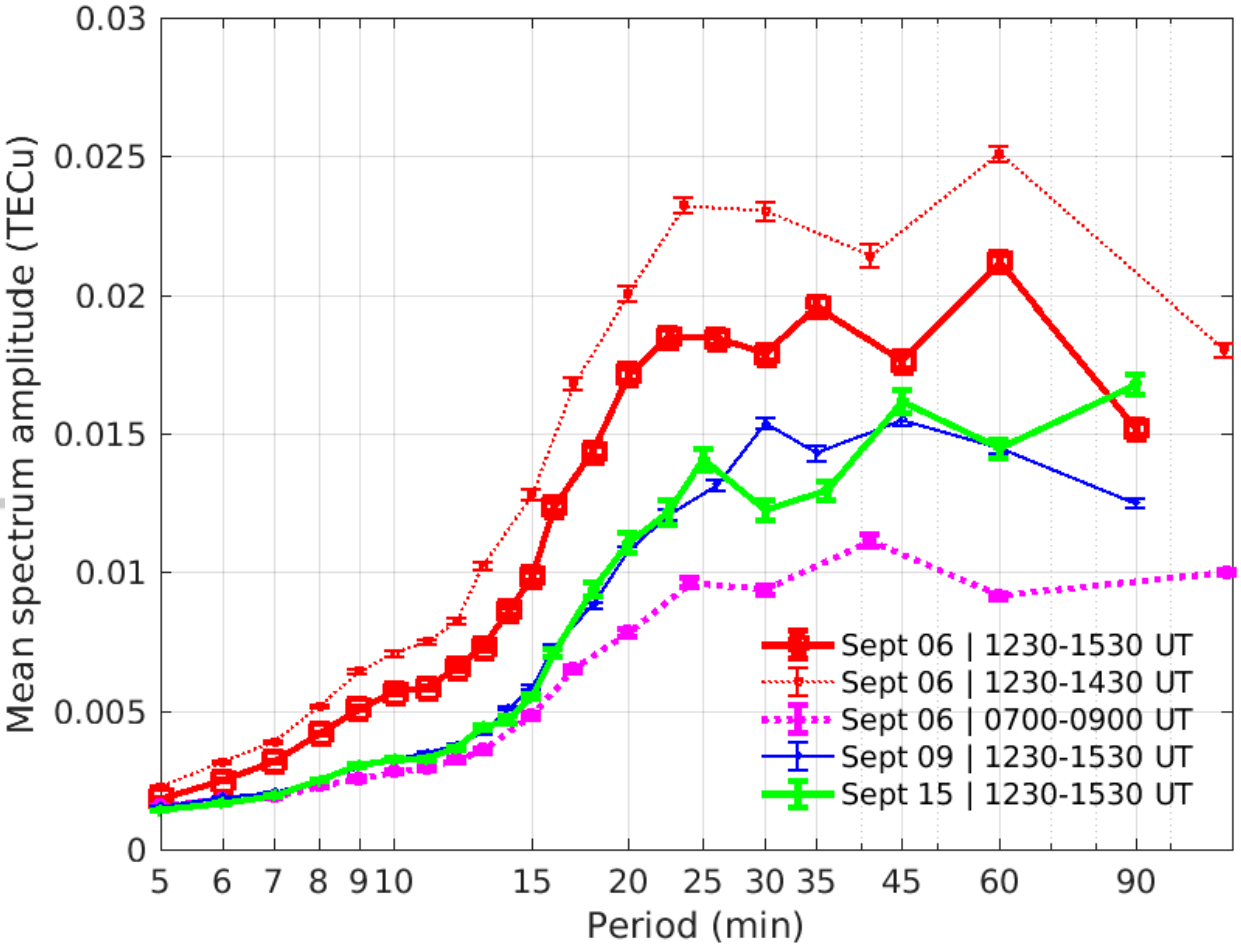

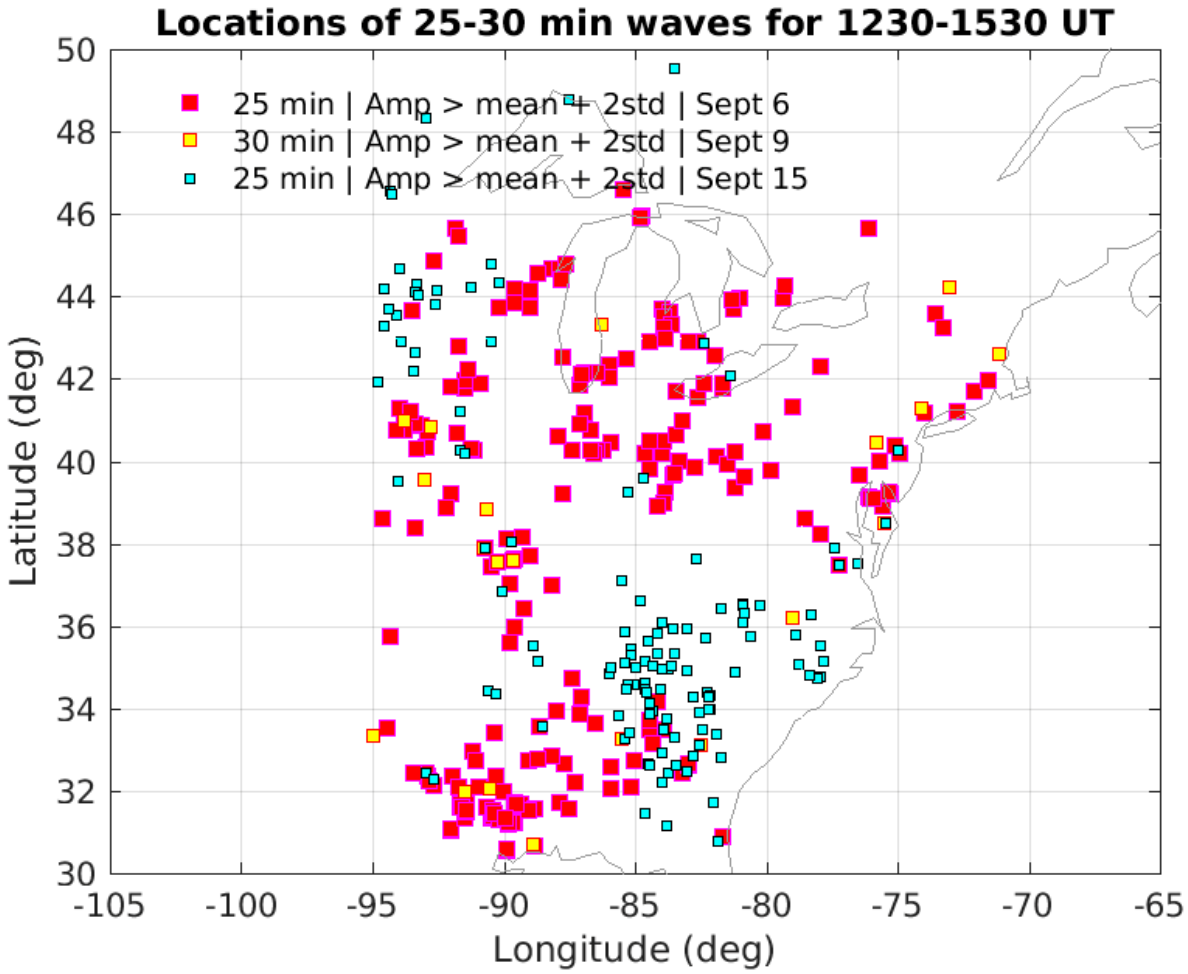

2019JA026585-f05-z-.png

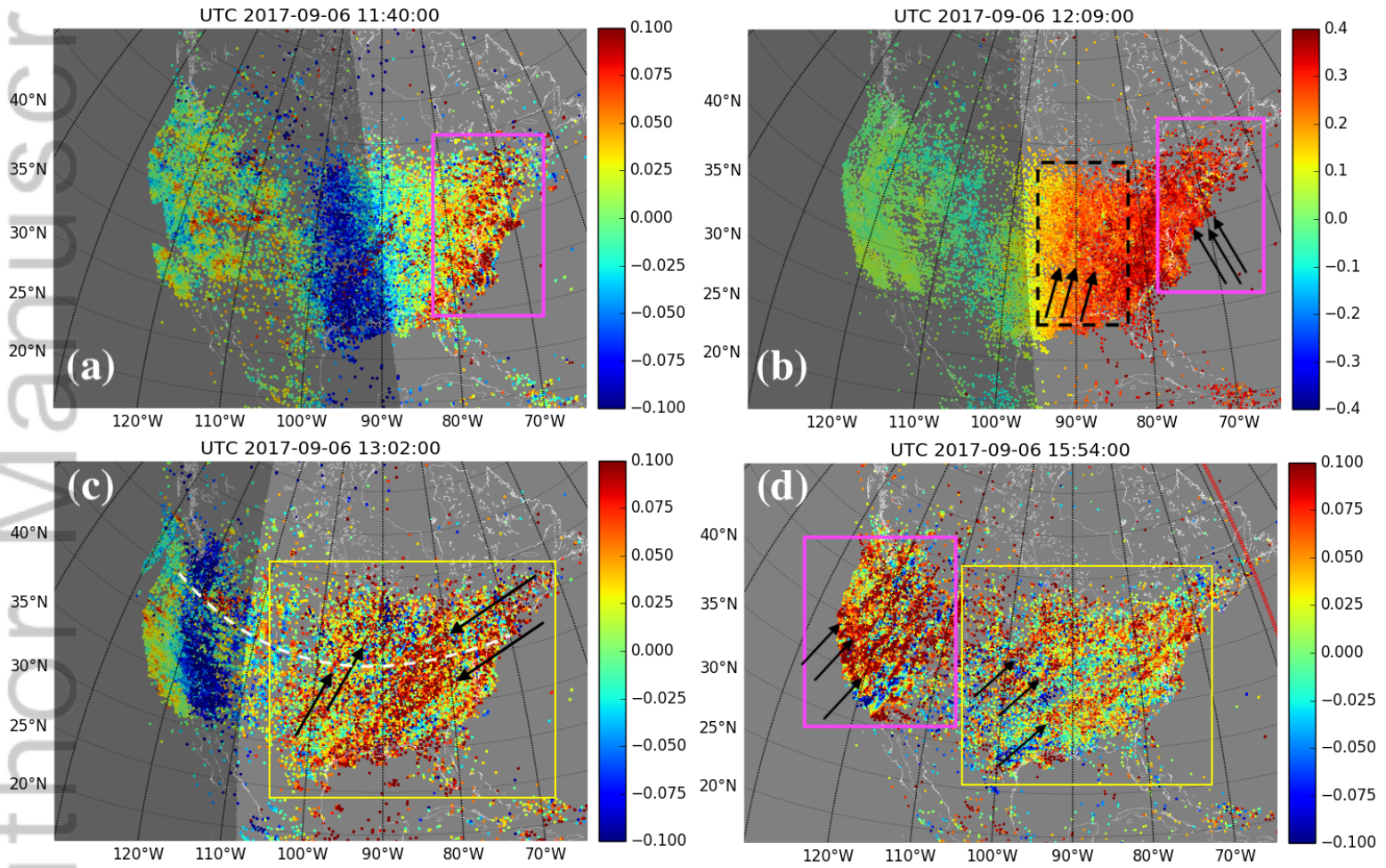

2019JA026585-f06-z-.png

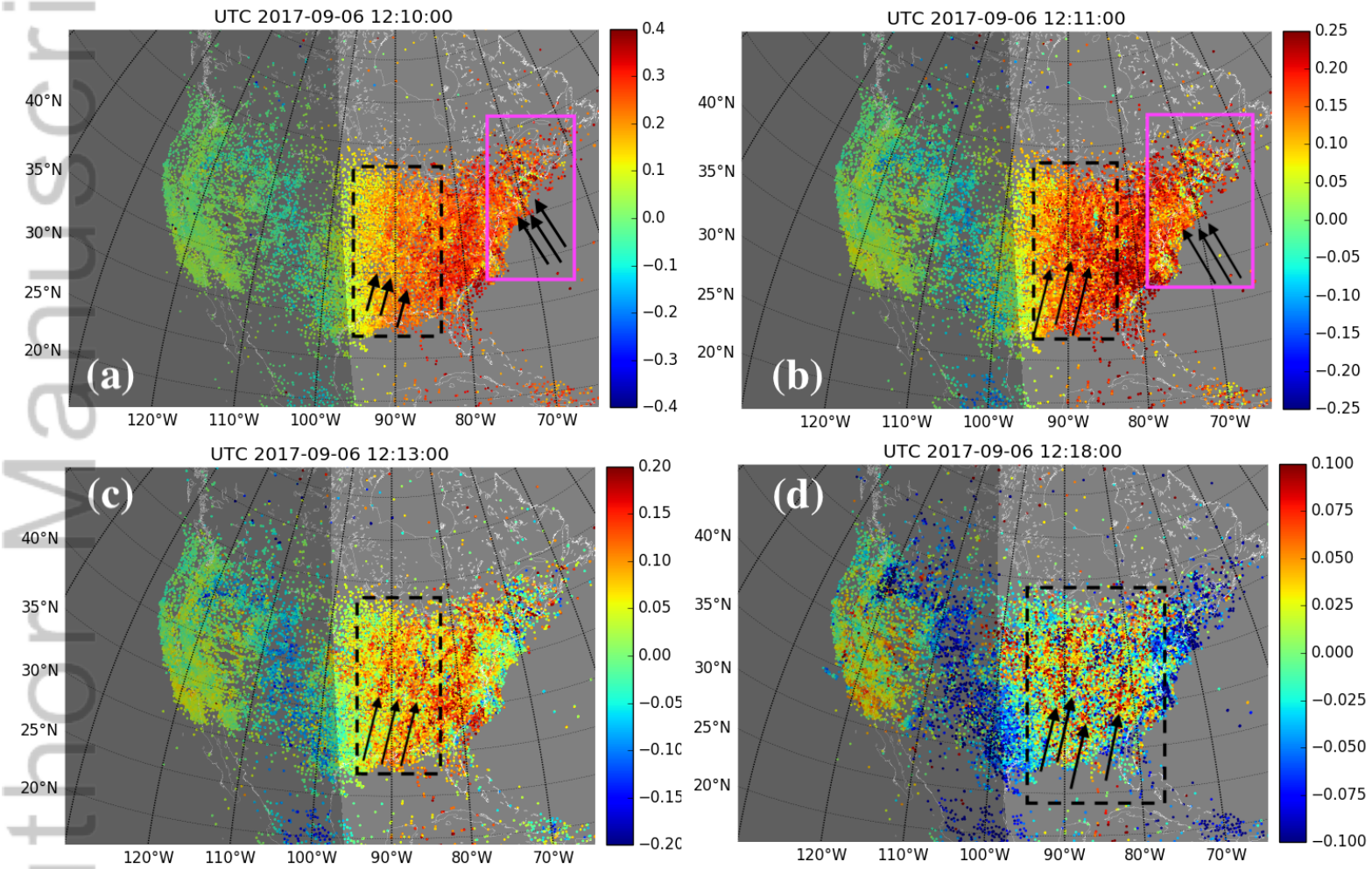

2019JA026585-f07-z-.png

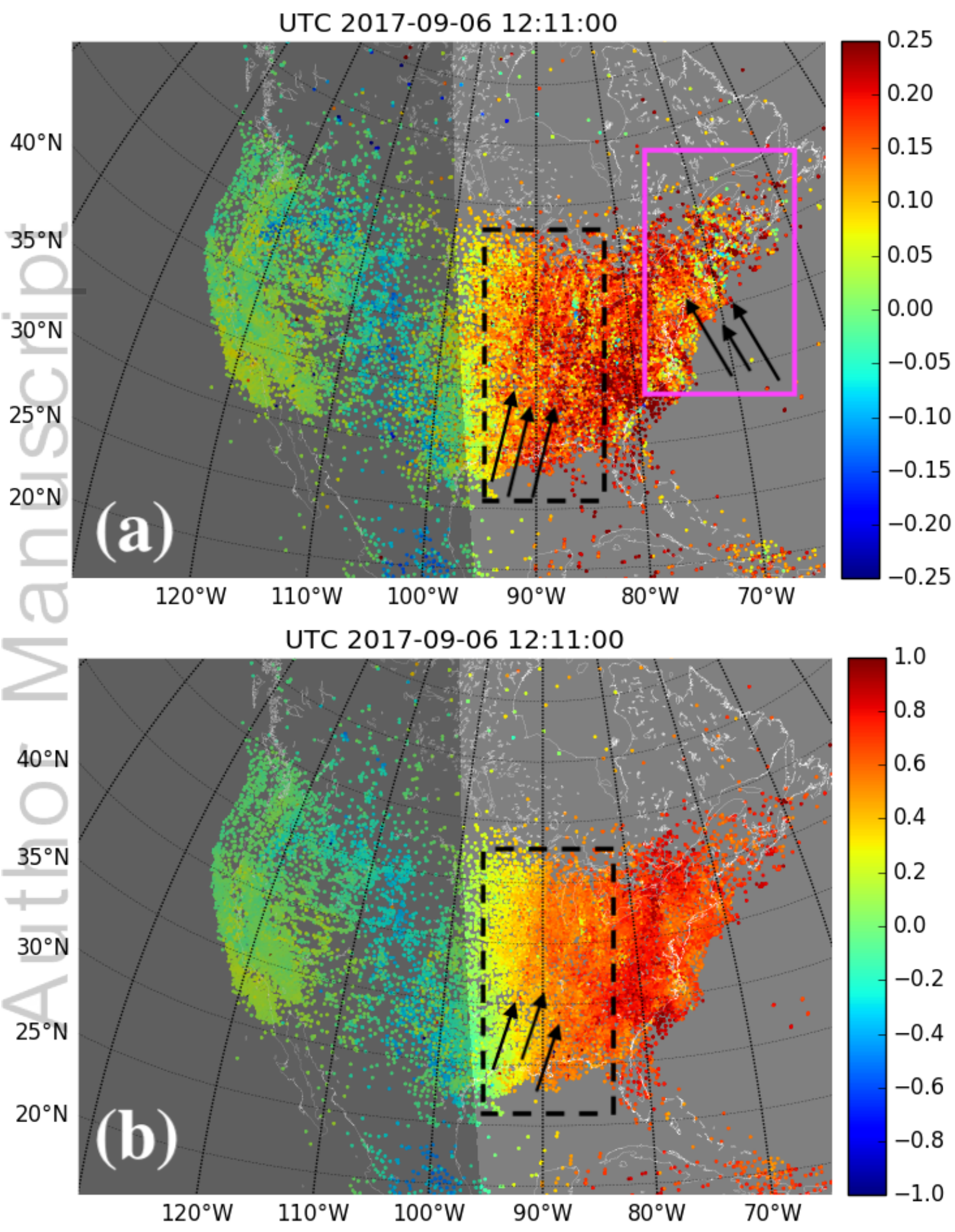

2019JA026585-f08-z-png

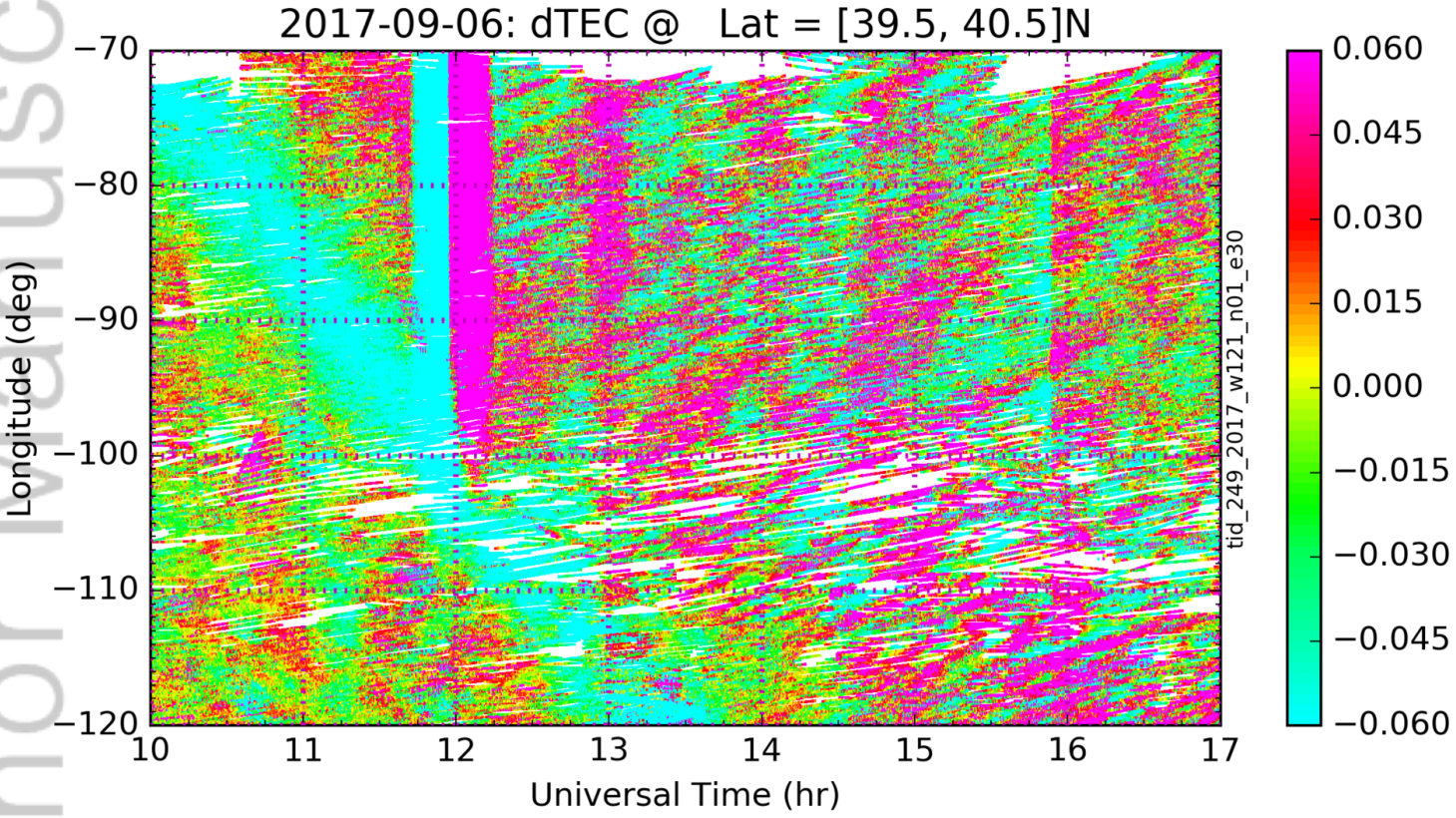

2019JA026585-f09-z-.png

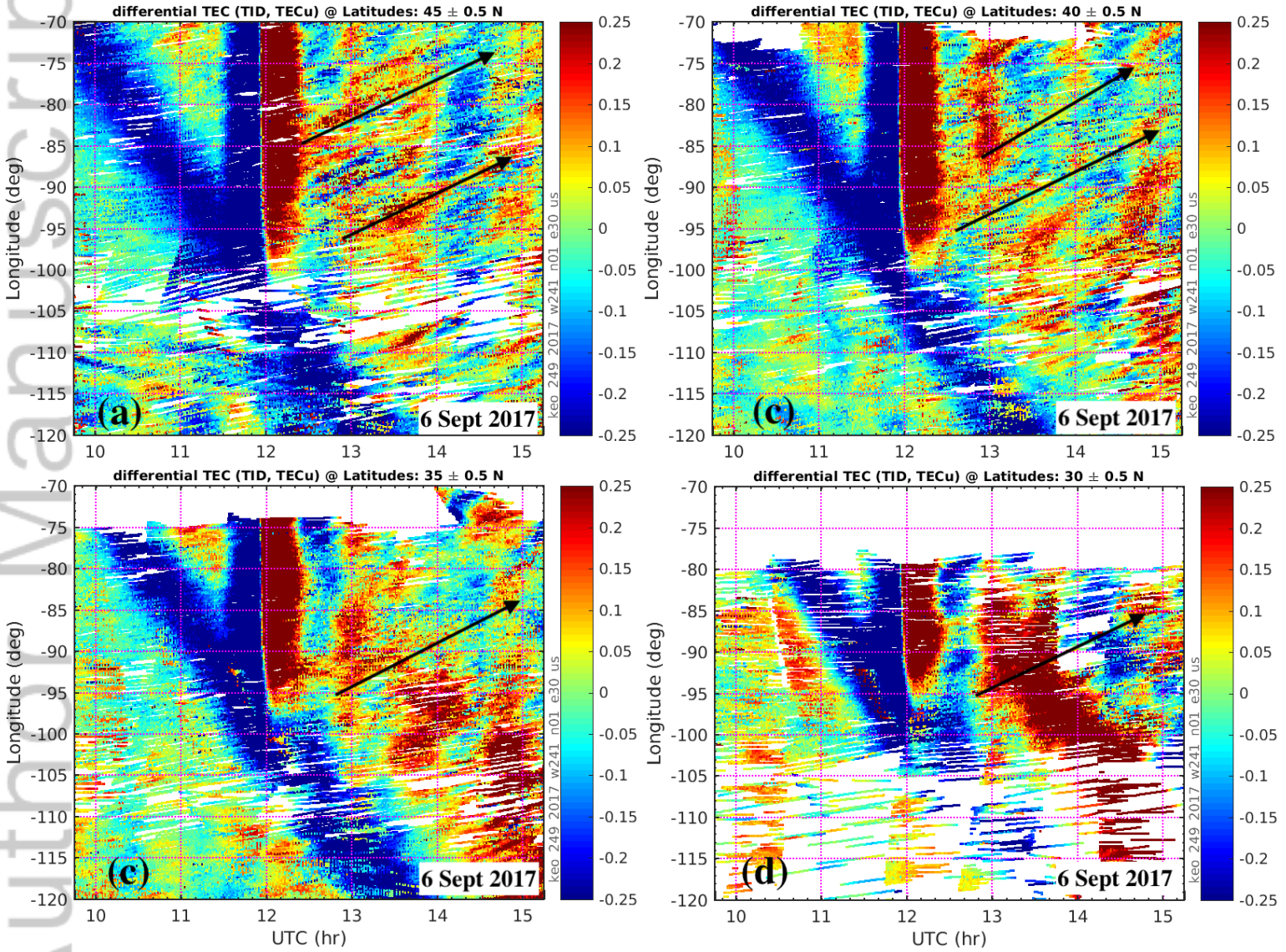

2019JA026585-f10-z-.png

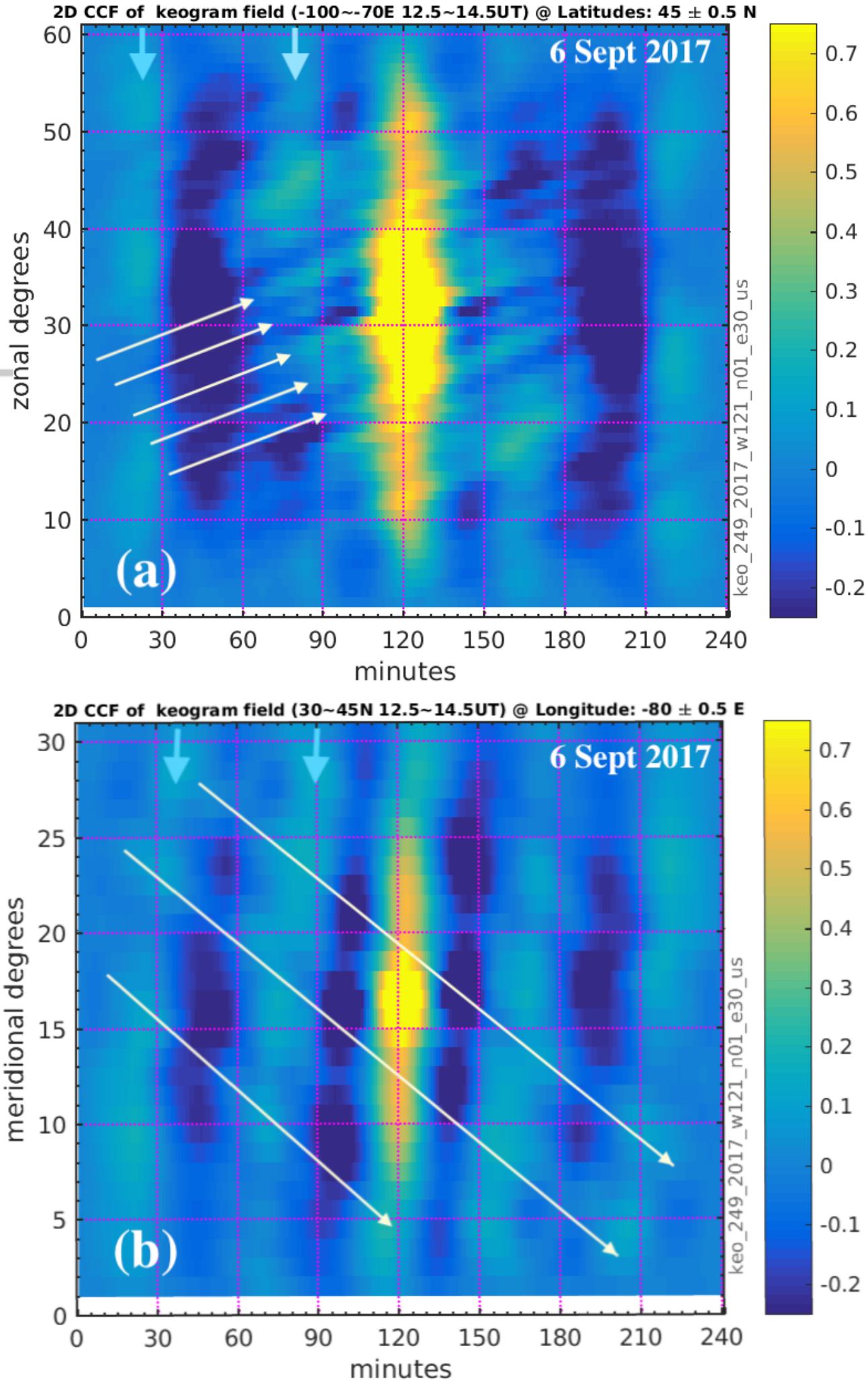

2019JA026585-f11-z-.png

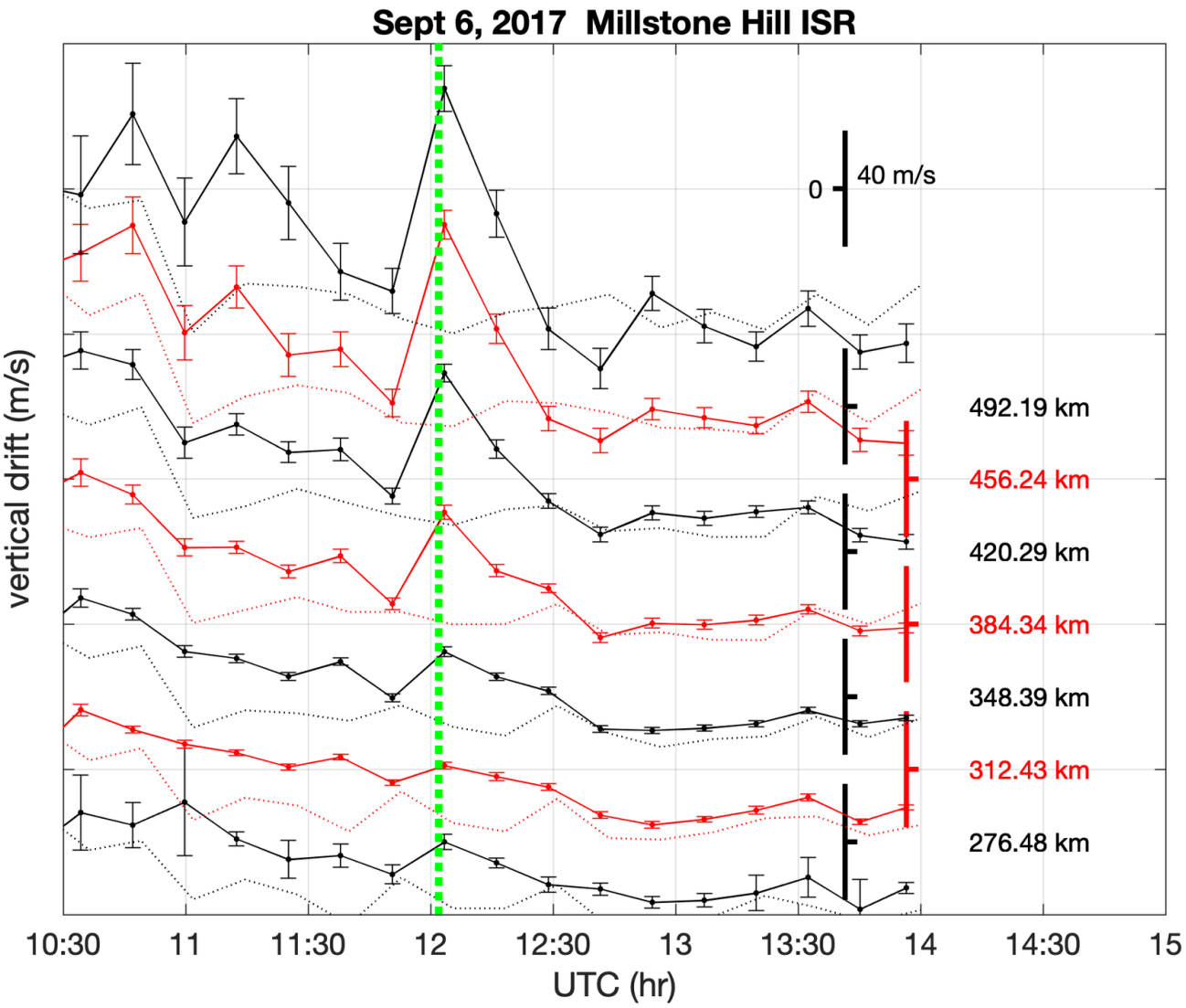

2019JA026585-f12-z-.png

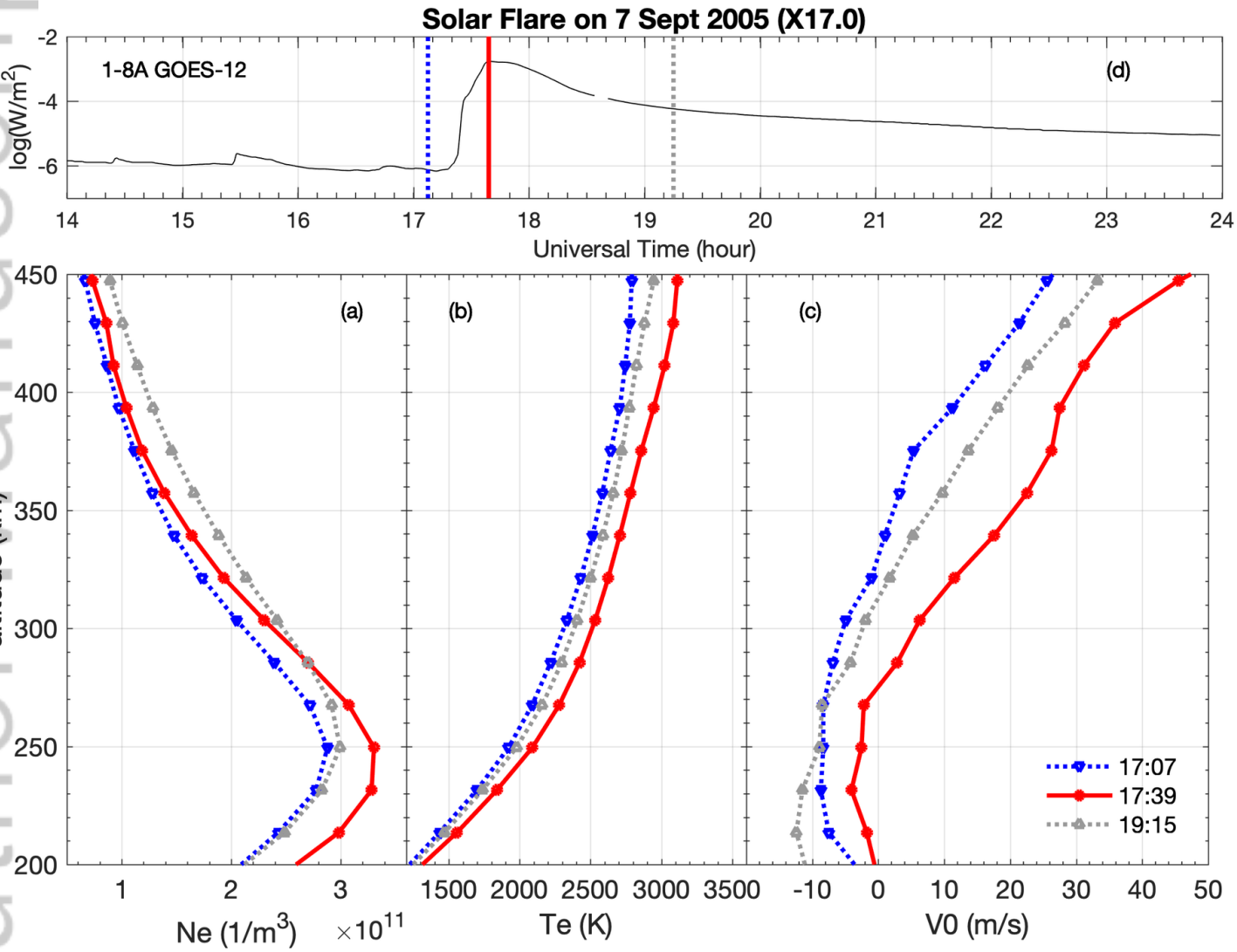

2019JA026585-f13-z-.png

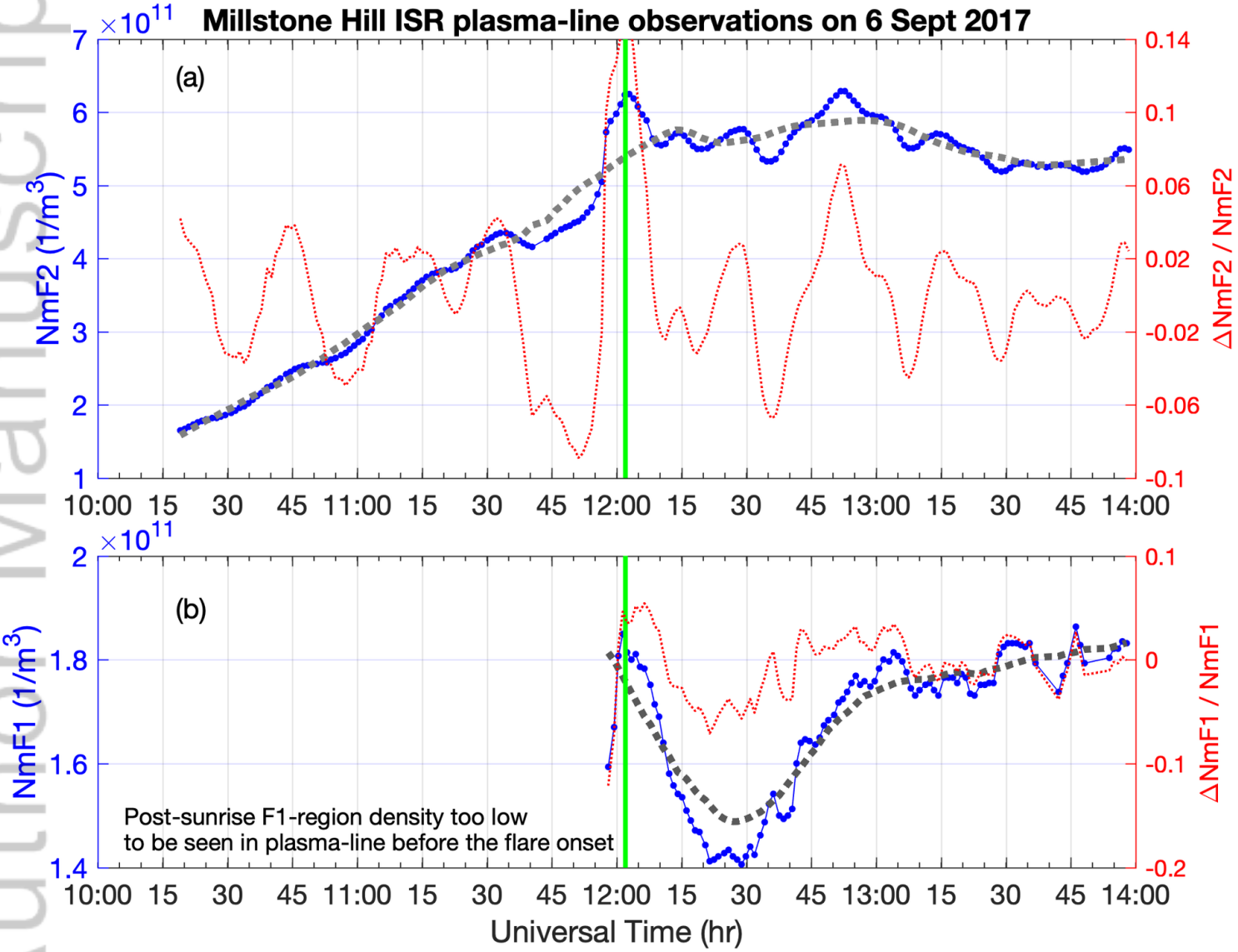

2019JA026585-f14-z-.png

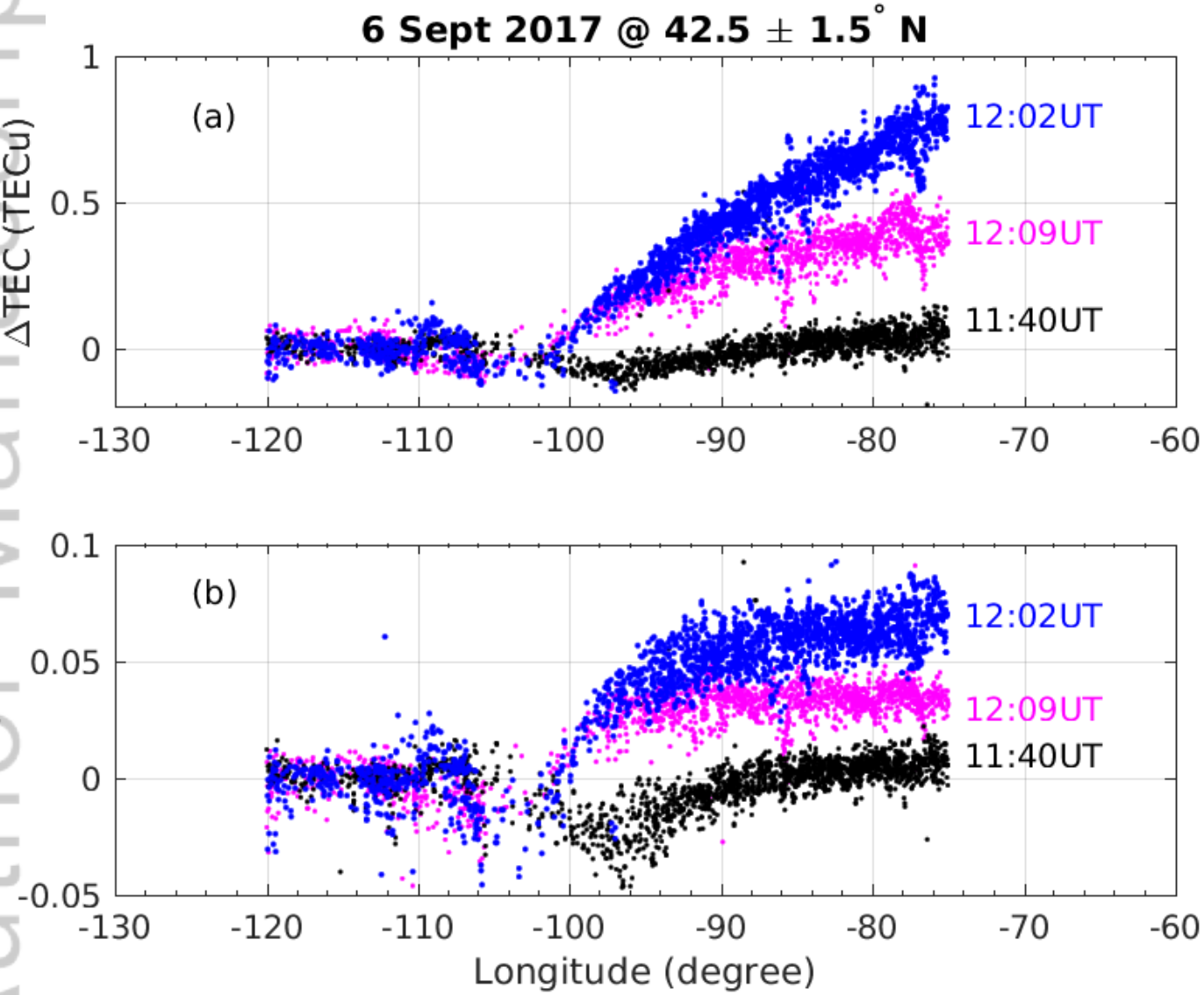

2019JA026585-f15-z-.png

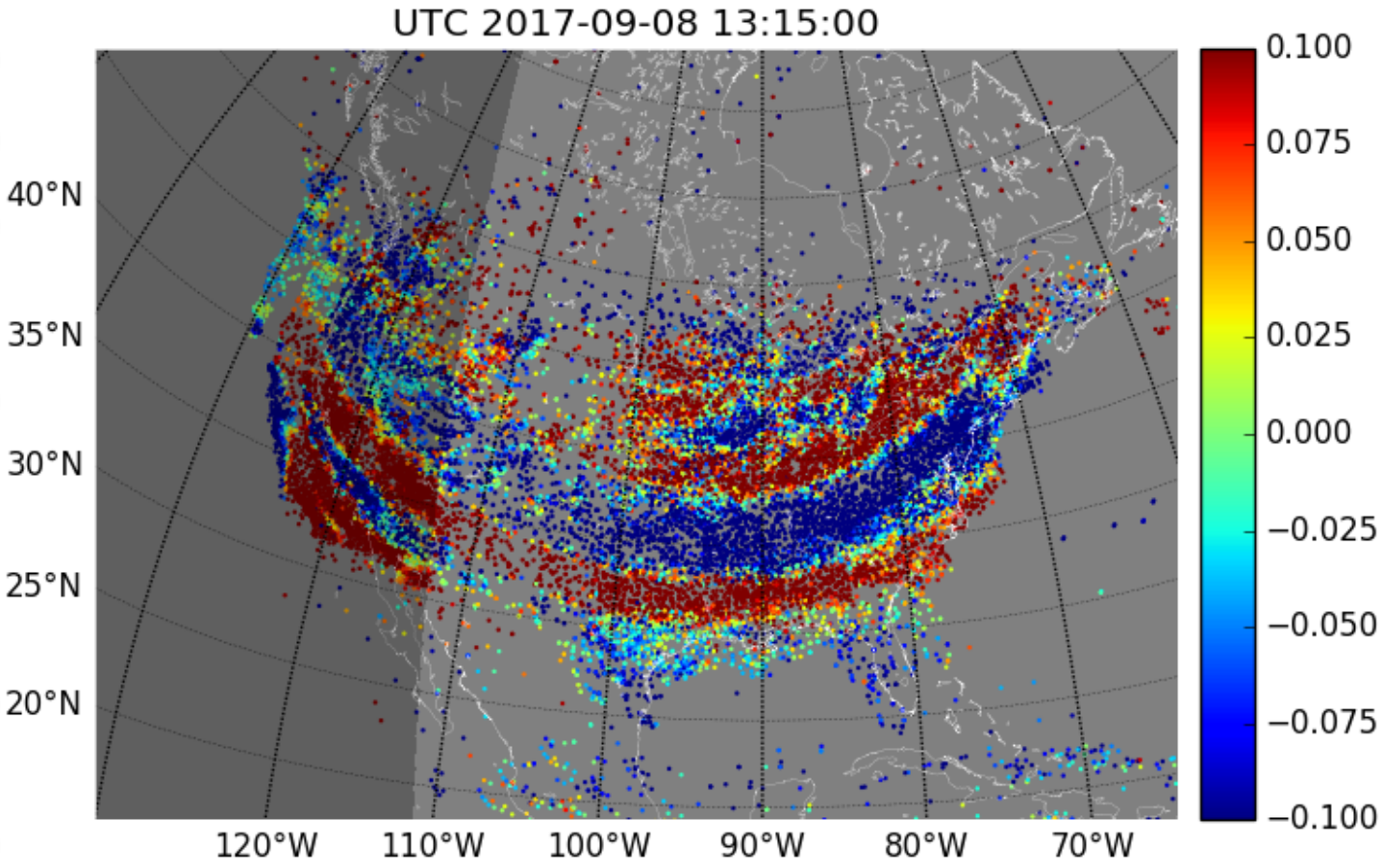

2019JA026585-f16-z-.png

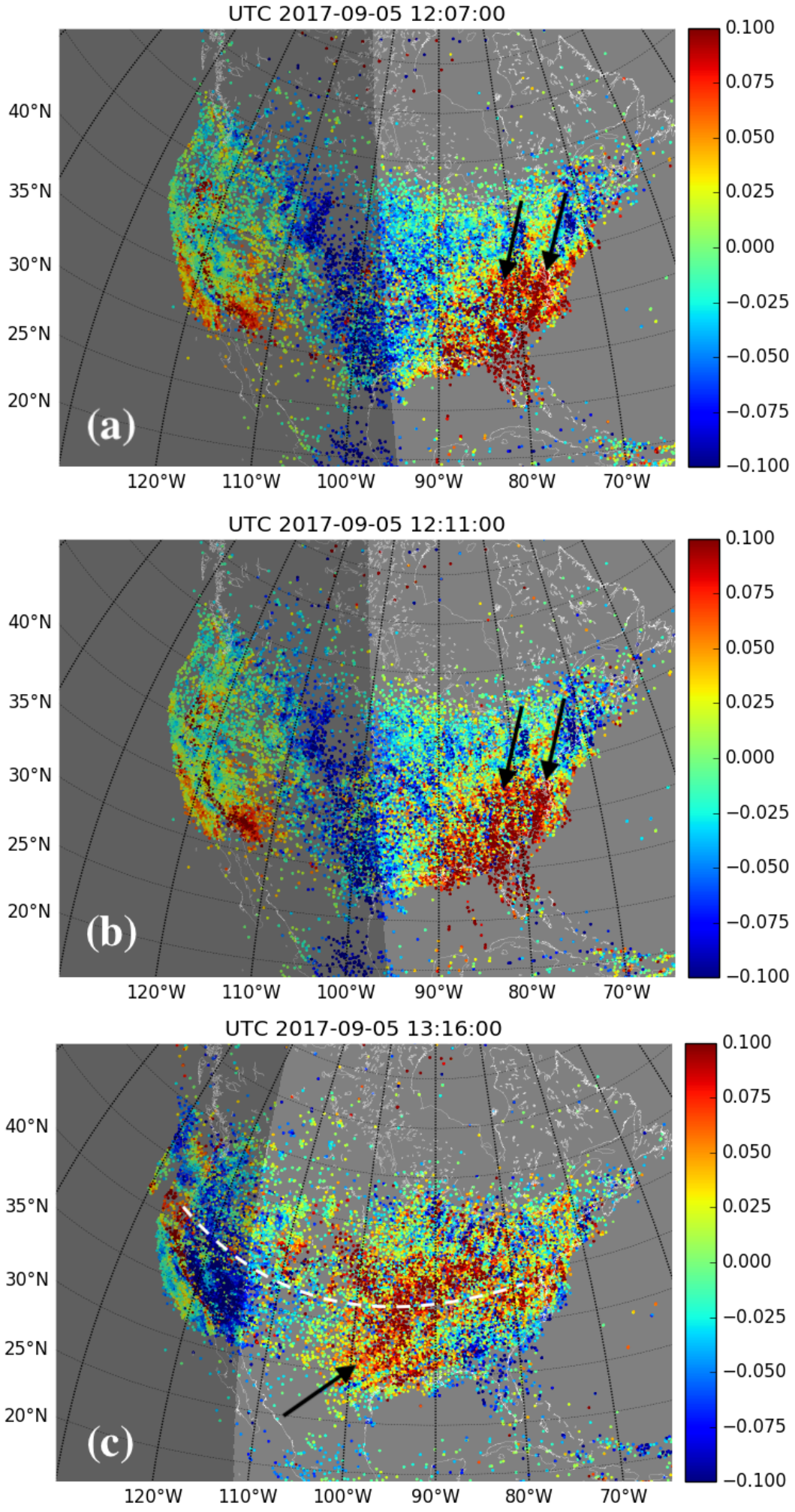

2019JA026585-f17-z-.png